UNIVERSITY OF SOUTHAMPTON

INTEGRATED OPTICAL MULTISENSORS FOR WATER QUALITY

by

Geoffrey Richard Quigley BSc, ARCS

Submitted for the degree of

Doctor of Philosophy

Department of Electronics and Computer Science

and Optoelectronics Research Centre

Faculty of Engineering and Applied Science

July 2000

UNIVERSITY OF SOUTHAMPTON

ABSTRACT

FACULTY OF ENGINEERING AND APPLIED SCIENCE

DEPARTMENT OF ELECTRONICS AND COMPUTER SCIENCE

AND OPTOELECTRONICS RESEARCH CENTRE

Doctor of Philosophy

INTEGRATED OPTICAL MULTISENSORS FOR WATER QUALITY

by Geoffrey Richard Quigley

This thesis is concerned with research into the development of integrated optical sensors for simultaneous measurement of the levels of a panel of analytes in water at concentrations of order 0.1 parts per billion.

A numerical model was established to investigate the optimum waveguide geometry for the application. This modelling yielded predictions that low numerical aperture waveguide devices could have their sensitivity increased by more than an order of magnitude by the addition of a thin overlay of high refractive index material.

Mach-Zehnder interferometers were used to measure the refractive index of aqueous solutions of sucrose. The devices were fabricated with different thickness high index overlays and were used to validate the predictions of the numerical modelling and to provide information about potential shortcomings of the sensor designs and materials. The test devices achieved a limit of detection of 4×10^{-7} refractive index units, the best reported results for integrated optical refractometers. These devices are also believed to be the first practical demonstration of the use of non-guiding high index films to improve the performance of channel waveguide sensors.

Fluoropolymer films used in the early sensor designs were found to be detrimental to the performance of the sensors. Silica was chosen as a substitute material and a series of experiments was performed to determine the optimum deposition parameters.

The final experiments bring together the various parts of the previous work in a practical demonstration of an integrated optical multi-sensor. Sensors based on fluorescent-labelled antibodies are presented with simultaneous measurement on four channels. Two of the four channels were coated with thin high index films to increase the intensity of the evanescent field. The detection limit for sensing isoproturon was found to be 0.03 parts per billion, lower than the target of 0.1parts per billion, on the two channels which did not incorporate the high index films. This is shown to be because the dyes used suffer rapid photodegradation in the high intensity fields.

Acknowledgements

The greatest vote of thanks must go to my PhD. supervisor, James Wilkinson, without whose support and extreme patience this thesis may never have been finished.

Thanks also to Richard Harris and Louise Hickey for invaluable help and advice over the course of my PhD and indeed to the rest of the Integrated Optics and Microstructures group. It has been a privilege and a pleasure to work with you all. I also enjoyed the slightly more pub-based side of our time together.

I would like to thank my co-workers in RIANA, particularly the group in Tuebingen who hosted me for a short time. Prior to RIANA I was rather nervous at the prospect of working with chemists and biochemists. I feel I learned a great deal and with surprisingly little pain.

Finally, I wish to thank all the other great people in the ORC with whom I shared my time there...

Contents

Contents ii

List of Figures v

List of Tables viii

1 Introduction 1

2 Optical sensors for water quality 7

2.1 Introduction 7

2.2 Review of opto-chemical sensing techniques 8

2.2.1 Absorption measurements and spectroscopy 8

2.2.2 Refractometry 10

2.2.3 Fluorescence, luminescence and phosphorescence 12

2.2.4 Summary 15

2.3 The European Union River Analyser project 15

2.3.1 Project goals 15

2.3.2 Immunosensing in RIANA 17

2.3.3 Overview of RIANA system 19

2.3.4 Requirements of RIANA 23

3 Theoretical description of high-index film enhancement of waveguide sensitivity 25

3.1 Introduction 25

3.2 The numerical model 26

3.3 Validation of the model 29

3.4 Multilayer approximation to graded index waveguides 33

3.5 Enhancement of the evanescent field 38

3.6 Coupling of guided modes across an interface 46

3.6.1 Overview of theory 46

3.6.2 Verification of the mode coupling model 47

3.6.3 Predictions of the mode coupling model 49

3.7 Operation of integrated optical Mach-Zehnder interferometer 50
3.8 Summary 52

4 Experimental verification of the numerical model **54**
4.1 Introduction 54
4.2 Fabrication and characterisation of waveguide devices 55
4.2.1 Fabrication of ion-exchanged channel waveguides 55
4.2.2 Spectral attenuation measurements 56
4.2.3 Thin film deposition and patterning 58
4.2.4 Spectral Response of Mach-Zehnder interferometers 60
4.2.5 Isolation layers 61
4.3 Refractometry of aqueous sucrose solutions 62
4.4 Results and Analysis 63
4.4.1 Response to a pulse of sucrose solution 63
4.4.2 Estimation of the detection limit 70
4.4.3 Losses induced by high-index films 72
4.5 Mach-Zehnder interferometer with no isolation layer 73
4.6 Summary 74

5 Silica film deposition and annealing **76**
5.1 Introduction 76
5.2 Format of the experiments 78
5.3 Results 81
5.4 Summary 82

6 Multi-channel fluorescence sensing experiments **85**
6.1 Introduction 85
6.2 Two channel fluorescence sensing experiments 88
6.2.1 Design of integrated optical chips 88
6.2.2 Apparatus 89
6.2.3 Bulk dye experiments 91
6.2.4 Antibody experiments 93
6.2.5 Conclusions from preliminary measurements 99
6.3 Four channel fluorescence sensing experiments 101

6.3.1 Introduction 101
6.3.2 Apparatus 102
6.3.3 Optical power budget 105
6.3.4 Bulk dye experiments 107
6.3.5 Antibody experiments 111
6.3.6 Calibration of sensor responses to isoproturon 118
6.3.7 Conclusions 120
6.4 Summary 120

7 Conclusions and Future Work **121**
7.1 Conclusions 121
7.2 Future Directions 122

References **124**

A Publications List **132**

List of Figures

1.1 Common optical waveguide geometries 3

2.1 Format of competitive binding immunoassay 18
2.2 RIANA System 20

3.1 A slab waveguide 26
3.2 Irradiance distributions for the TE modes of a three layer guide . . . 30
3.3 Mode profiles of the example six-layer guide 32
3.4 Dispersion curves for a 3 layer guide 34
3.5 Dispersion curves for a three layer guide 34
3.6 Multilayer staircase approximation to a Gaussian index profile 35
3.7 Variation of irradiance at the superstrate-guide interface with thickness of high-index layer 39
3.8 Irradiance distributions of TE_0 modes of a 4-layer guide for various thicknesses of high-index layer 40
3.9 Irradiance distributions of TE_0 modes of a 4-layer guide —zoomed on the superstrate-guide interface 41
3.10 Enhancement of irradiance at the superstrate-guide interface with thickness of high-index layer 42
3.11 Effect of a high-index film on sensitivity to superstrate index 43
3.12 Variation of loss in an absorbing structure with thickness of high-index layer 43
3.13 Enhancement of surface irradiance by high index films 44
3.14 Enhancement of power carried by superstrate evanescent fields by high index films 45
3.15 Variation of the coupling efficiency between identical single moded waveguides with displacement parallel to the interface 48
3.16 Variation with overlay thickness of the transition loss going from non-overlaid waveguide to waveguide with high index overlay of refractive index 2.1 49
3.17 An integrated optical Mach-Zehnder interferometer 50

4.1 Mach-Zehnder interferometer 55
4.2 Spectral attenuation apparatus 57
4.3 A spectral attenuation plot for an ion-exchanged y-junction 58
4.4 Alpha-step scan across a Mach-Zehnder interferometer device with a thin film of tantalum pentoxide 60
4.5 Spectral attenuation of a device incorporating a Mach-Zehnder interferometer with a reference arm 61
4.6 Apparatus for flow injection analysis 63
4.7 Response of a Mach-Zehnder interferometer to a pulse of sucrose solution 64
4.8 Phase response of interferometers to different refractive index perturbations — TE operation 66
4.9 Comparison of theory and experiment — TE operation 68
4.10 Phase response of interferometers to different refractive index perturbations — TM operation 69
4.11 Residuals of baseline noise 71

5.1 Schematic representation of integrated optical devices for evaluating the performance of silica isolation layers 78
5.2 Transmission of waveguides coated with 5mm and 10mm long silica films as a function of annealing time 83

6.1 Devices designed for fluorescence sensing experiments 88
6.2 Normalized fluorescence and absorption spectra of Cy5.5 dye compared with the transmission spectrum of the Schott filter 91
6.3 Responses to bulk dye solution along chip with 30nm Ta_2O_5 patches . 93
6.4 Example antibody test cycle 94
6.5 Variation of collected fluorescence with antibody concentration 96
6.6 Responses to bulk solutions of Cy5.5 dye between patches on chip with 30nm Ta_2O_5 overlay 97
6.7 Response to Cy5.5 dye labelled antibody between patches on chip with 30nm Ta_2O_5 overlay 98

6.8 Response to many antibody samples of identical concentrations on two consecutive days 99
6.9 Calibration of chip with 30nm Ta_2O_5 overlay 100
6.10 Detector calibration 104
6.11 Response of four measurement channels to samples of Cy5.5 dye solution 108
6.12 The effect of using a reference signal on the ratio of standard error to the mean response 109
6.13 Responses at 6 patches 110
6.14 Response to antibody solution 112
6.15 Mean response to antibody samples over 24 test cycles 113
6.16 Fit to antibody response 114
6.17 Effect of integration time and referencing on the scatter of data . . . 116
6.18 Calibration curve, chip with 20nm Ta_2O_5 118

List of Tables

3.1 Comparison of results with those from Pascal Mauron's model for a guide with index 1.6, superstrate index 1.33, substrate index 1.55 . . 31
3.2 Comparison with published results for 6 layer guide 31
3.3 Comparison with published results for 6 layer absorbing guide 33
3.4 Comparison between staircase approximation and published results for the refractive index profile in equation (3.13) 36
3.5 Comparison between staircase approximation and published results for the refractive index profile in equation (3.14) 37
3.6 Comparison between staircase approximation and published results for the refractive index profile in equation (3.15) 37

4.1 Experimentally determined enhancement factors for TE modes 65
4.2 Detection limits of Mach-Zehnder interferometers (method 1 uses gradia of best-fit straight lines that are forced to pass through the origin) 72
4.3 Losses in Mach-Zehnder interferometers due to interaction regions . . 73
4.4 Sensitivities and detection limits for MZI's without isolation layers . . 74

5.1 Waveguide loss induced by silica films deposited with different parameters and effect of annealing at 250°C :TE polarization 81
5.2 Waveguide loss induced by silica films deposited with different parameters and effect of annealing at 250°C :TM polarization 82

6.1 Enhancements and loss calculated from responses to dye solutions . . 110
6.2 Enhancements calculated from responses to antibody solutions 115
6.3 Detection limits calculated from calibration curves 119

Chapter 1

Introduction

The modern world is highly dependent on mass produced goods and intensive farming to supply enough goods to satisfy the market demand. The cost of this is that farms and factories release potentially damaging chemicals into the environment: for example, the use of pesticides is necessary to increase the quality and yield of agricultural produce, but these pesticides are highly toxic. Pesticides are leached off the fields into streams and rivers where they not only can harm wildlife, but can also reach human drinking water supplies. Other chemicals that also find their way into water supplies include herbicides, also heavily used in farming, and surfactants, commonplace among industrial effluent. The population of the world continues to rise, as do the expectations of the population. As the demand for food and for goods continues to rise there is a risk of the quantities of chemicals released into the environment rising at the same or greater pace.

European and national legislation limits the permitted concentrations of many chemicals in industrial effluents, river water and in drinking water. The permissible concentrations of these chemicals are very low, of order 0.1 parts per billion (ppb), and the legislation is continuously changing to include new analytes and lower limits. Legislation is of little use if there is no way to check that it is being complied with. Current techniques mostly involve taking water samples to central laboratories where the techniques used to analyze the samples tend to be slow, laborious and expensive requiring highly trained staff to perform the analyses. There is great interest in finding low cost solutions to the problem of measuring water pollutants at low concentration as quickly and reliably as possible. The ideal device would be portable enough to take to the sample and easy enough to use that it could be operated by an unskilled person. The device would also need to be able to measure a range of analytes simultaneously if it is to be useful in light of the range of pollutants that are finding their way into water. It is also important that a new sensor should be adaptable, enabling new analytes to be measured without major changes to the

sensing system.

Integrated optics provides an ideal platform on which to build sensors for water pollution monitoring. Optical effects are deeply rooted in much of chemical analysis, the common example being the use of litmus and other indicators for pH measurements. Indicators make use of changes in absorption at particular wavelengths in response to changing concentrations of chemical species. Other optical changes that are commonly used include changes in refractive index in surface films and in fluorescence emitted when a fluorophore is excited by a light source. The sensors presented in this thesis are based on these later examples.

Sophisticated measurement techniques have been developed which make use of changes in optical properties to provide highly sensitive readings of the concentrations of chemicals in various environments. When dealing with low analyte concentrations it becomes desirable to somehow increase the interaction of the light with the analyte. This is mainly achieved by increasing the intensity of the illumination or by preconcentrating the sample.

Guided-wave optics, the field which encompasses fibre optics and integrated optics, offers convenient ways of providing locally intense illumination since optical waveguides are generally of order microns thick or less. The majority of the power in guided modes is normally confined to the "core" of the waveguide but part of the power is carried in the evanescent fields in the cladding region(s). Figure 1.1 shows some examples of optical waveguide geometries. Other examples of common structures can be found in the literature [1] and more complex structures are continuously being devised.

Due to the ease of access to the evanescent fields, integrated optics (IO) have increasingly found application in the field of chemical sensing [2]. A broad range of optical techniques for chemical analysis based, for example, on absorption, refractive index variation, fluorescence or chemiluminescence may be exploited and have the potential for great sensitivity. Fibre optics are also used for evanescent wave sensors. To access the evanescent fields, techniques such as tapering the fibres and polishing away the cladding to give D-fibres are used [3]. Fibre optic sensors offer the potential for remote sensing, distributed sensing and the easy use of long optical path-lengths. Integrated optics has other particular advantages for sensing in small

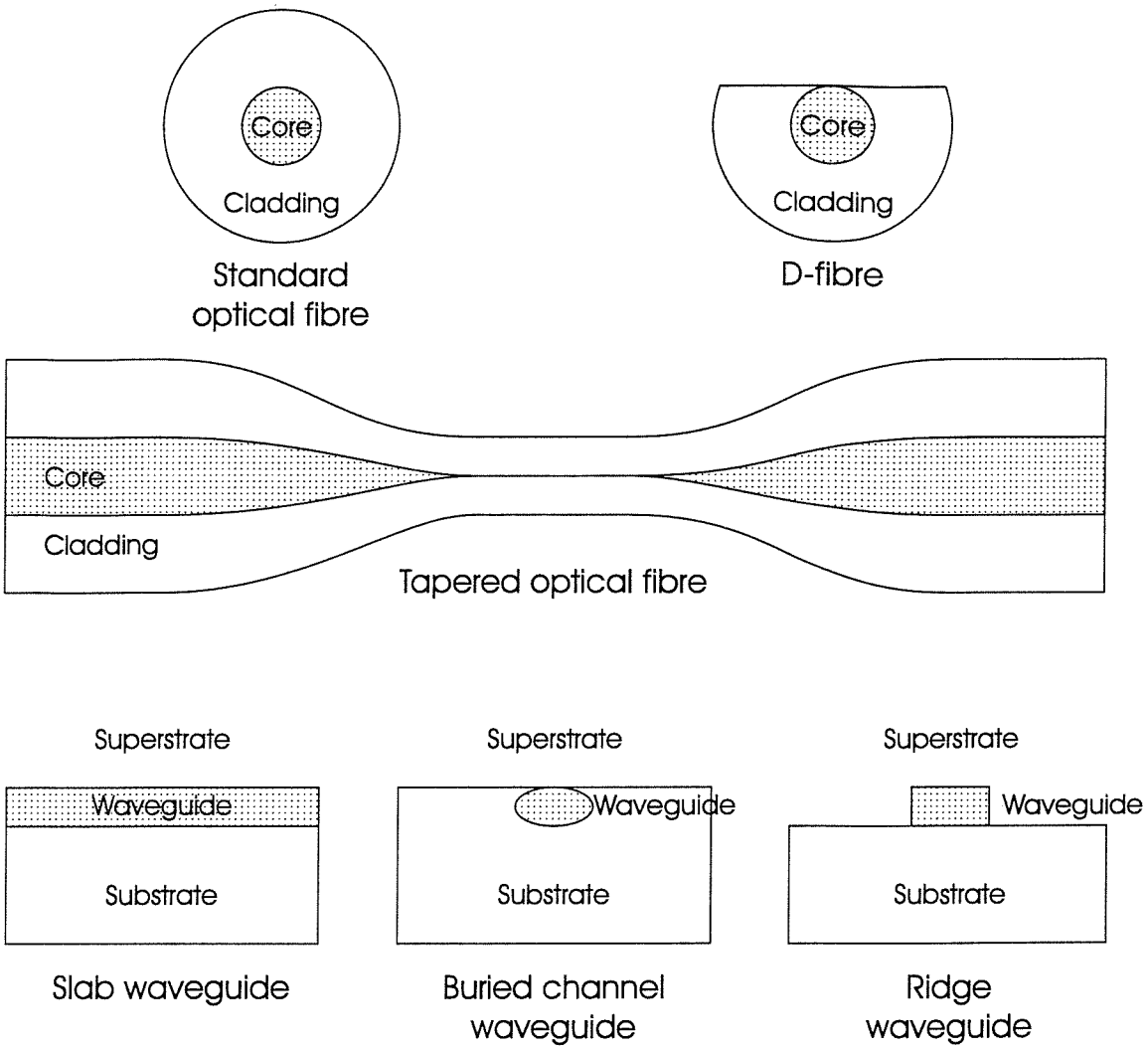

Figure 1.1: Common optical waveguide geometries

volumes. It allows the fabrication of several different devices of one chip offering the simultaneous measurement of several analytes, or of different optical parameters. The planar format of integrated optics is also convenient for the attachment of flow-cells, facilitating controlled measurements on fluid analytes. Integrated optical chips also tend to be more rugged than their fibre optic equivalents.

This thesis is primarily concerned with the design and fabrication of integrated optical transducers capable of measuring the concentrations of a panel of analytes at concentrations of order 0.1ppb. The emphasis here is on the optical aspects of the sensor. This work was performed as part of a European Union funded project titled River Analyser (RIANA) [4] where, in parallel with the transducer development, other workers developed surface chemistry, antibodies and an integrated instrument. The project will be described in the next chapter in order to put the work on optical

transducers into context.

The choice to use integrated optical transducers having been made, it was necessary to choose suitable materials and waveguide geometry. For a given substrate, the fields at the surface of a thin high index waveguide are more intense for a given input power than those of a lower refractive index waveguide. However, coupling light into thin high index waveguides is harder and they tend to have higher losses. These losses are largely due to scattering but are also due to absorption in the waveguides. Lower refractive index waveguides, such as those made by potassium-sodium ion-exchange, are much easier to couple light into but are less sensitive to changes in the superstrate. With a photolithographically patterned metal mask, ion exchange can easily be used to form low-loss channel waveguides, allowing easy construction of devices such as couplers, splitters and interferometers. Fibre coupling into ion-exchanged channel waveguides can be very simple and fibre pig-tailing of devices is routinely carried out. Both high index waveguides [5, 6] and lower refractive index waveguides [7–9] have been demonstrated in sensing applications. Ion-exchange was selected for this work due to the greater ease of input-coupling, the low-loss of ion-exchanged channel waveguides and the ease of making more complicated devices as would become necessary for realising multi-sensor arrays. In the long term, ion-exchanged devices can be fibre pig-tailed, giving improved input coupling stability and greater ease of use for an unskilled operator.

Stewart et al. [10–13] predicted that it would be possible to increase the sensitivity of methane gas sensors by overlaying D-fibres with high refractive index films — sensitivity enhancements of one or two orders of magnitude were predicted. It is desirable to achieve the same kind of enhancements with evanescent wave integrated optical devices. To investigate the feasibility of this approach, a similar computer model was established, allowing design of IO sensors, and devices were fabricated to measure the enhancement factor. The modelling is presented in chapter 3. In chapter 4, Mach-Zehnder Interferometers (MZI's), used as refractometers, were selected as being suitable devices for testing the theoretical predictions. The responses of four devices to refractive index changes were measured. From analysis of these results it can be seen that increases in sensitivity of greater than an order of magnitude are easily attainable.

This technique for enhancement of evanescent fields allows a trade-off between the high sensitivity of high index planar waveguides and the high fibre coupling efficiency and low loss of lower index channel waveguide devices. Devices were fabricated and tested to discover the size of the enhancement in sensitivity over standard integrated optical sensors. The detection limits of the devices were estimated and found to compare favorably with the detection limits of devices reported in the literature.

An approach similar to this in some respects is that of Itoh et al. [14] where a potassium-sodium ion exchanged waveguide is used to couple into a higher refractive index waveguide. Coupling into thin film waveguides high losses were observed in the films. Later work [15, 16] investigated use of a dual ion-exchange process to give a silver ion exchanged waveguide overlaid on a potassium ion exchanged waveguide. They demonstrated an increase in sensitivity of an order of magnitude over their potassium ion-exchanged waveguides for the composite system, but found that the waveguides were adversely affected by UV light. The field enhancements predicted for non-guiding films of high index material are greater than or equal to those measured in [16].

A concern has always been that the greater the enhancements in the evanescent fields are, the greater the loss is expected to be. The highest sensitivity will therefore be achieved for the design which balances loss and enhancement.

In this research, integrated optical Mach-Zehnder interferometers incorporating high-index overlays have been designed and fabricated for the first time and sensitivity enhancement of a factor of 50 or so demonstrated. A detection limit of 4×10^{-7} in refractive index was determined for devices which combined high sensitivity with low loss, equaling the best results in the literature for other integrated optical devices. Instrumental improvements are expected to allow further reductions in this limit.

In the course of making and using the devices necessary for this research, it became clear that the isolation layers being used were not performing well enough. The isolation layer is a layer of dielectric material of lower refractive index than the waveguide which is used to limit interaction of the evanescent fields with the superstrate medium. The purpose of an isolation layer in these devices is two fold,

the isolation layer protects the waveguides from the outside world, e.g. the black rubber o-ring on the flow cell, and helps to prevent the waveguide from interacting with the analyte except at the designed interaction regions. The material used initially was Teflon FEP, a transparent fluoropolymer. This material is very soft and easily damaged and evaporated films were often found to adhere badly to the surface of the chip. Silica was chosen as a possible alternative material and work was performed to find the optimum parameters for the deposition of silica films. This work is presented in chapter 5.

Chapter 6 brings together the work on sensitivity enhancements and on isolation layers and applies this to making multichannel fluorescence sensors. This work concentrates on examining these transducers as part of the RIANA system. The sensitivity enhancements from high index films are demonstrated to work similarly for bulk dye solutions to the way they did with the refractometers, but when used with dye-labelled antibodies it was found that the dye was rapidly photobleached and that the advantage from the addition of high index films was lost. The system is examined in detail, including calculations of how much light was reaching each part of the system, to illustrate where the most important areas for improvement are. The experiments demonstrate the use of integrated optical transducers for making multi-channel fluoroimmunosensors for water quality. The final sensors were capable of measuring the concentration of isoproturon in water simultaneously on four channels with limits of detection below 0.1 ppb being available on two of those channels and a test cycle of less than 15 minutes. When combined with the technology from the rest of the project these sensors will comprise the fast, compact, sensitive multi-analyte sensing system envisaged earlier.

In the concluding chapter, the results are summarized and the salient points are highlighted. Future directions are suggested based on the findings.

Chapter 2

Optical sensors for water quality

2.1 Introduction

There are myriad optical techniques which have been applied to chemical sensing. These techniques can be summarized in terms of three optical effects — the absorption, emission or change in speed of light (quantified as index of refraction). These things are not entirely separate, for example absorption can be expressed as the imaginary component of a complex refractive index and fluorescence is commonly preceded by the absorption of light at a shorter wavelength. Guided wave optics and, more specifically, integrated optics provides new ways of measuring changes in these properties. In this chapter, the use of guided wave optics in chemical sensing is reviewed and reasons for the choice of sensing techniques in RIANA are given. Due to the great variations in the way these techniques have been used in the past, meaningful quantitative comparison of published results was not possible in all cases.

Often the absorption, emission or refractive index change due to an analyte is too weak measure or cannot be distinguished from similar effects caused by different sources. For this reason it is common to use indicators and labels to cause a large effect that can be measured and which is specific to the analyte. For this reason, immunosensors were developed which use antibodies specific to the analytes of interest. Antibody molecules are large, with molecular weights of 250,000 being commonplace. These large molecules attach themselves to targets which have particular arrangements of chemical groups, in the same way that jigsaw pieces fit together. One advantage of antibody molecules is that they can be attached to a surface. Using this idea, the antibodies can interact within a large volume of liquid, but the final measurement takes place in a small volume next to a surface. This is analogous to concentrating the sample, although as will be seen with RIANA, the schemes for doing this include binding inhibition immunoassays in which none of the analyte is contained in the layer of bound antibodies. When antibodies bind

to a surface, the presence of a such large molecules causes a local increase in refractive index. The refractometers reviewed later in this chapter lend themselves well to monitoring the formation of these layers. However, refractive index based immunosensing is prone to non-specific interferences such as temperature changes, binding of unwanted chemical species and fluctuations in the composition of bulk water samples. Because of this, the approach taken for immunosensing in this work was based upon antibodies with fluorescent labels which may be detected with greater specificity.

This chapter compares the different optical changes that have been used in chemical sensors, particularly integrated optical sensors, to illustrate the advantages of the different schemes. Due to the great differences in the sensors discussed it is hard to meaningfully compare quantitative performance and so this has been restricted to where it is relevant.

From examination of the various methods that have been applied to chemical sensing, the choice of immunosensing with fluorescent-labelled antibodies was made. This choice takes into account the ideals that were lain out in the previous chapter and the practicalities of constructing useable devices.

The application of this work was in the European Union RIANA project, in which fluoroimmunosensors were used to measure the concentration of a panel of analytes in river water. This chapter concludes with a discussion of how the constraints of RIANA helped define sensor development.

2.2 Review of opto-chemical sensing techniques

2.2.1 Absorption measurements and spectroscopy

Possibly the simplest and best known optical effect applied to chemistry is the changing absorption of light in response to a chemical change. The common example is the colour change of litmus in response to pH, but there are many other indicators in common use, e.g. phenolphthalein, methyl red, thymol blue. The use of indicators is a very important concept in sensing. A direct measurement of the concentration of chemical species is possible using spectroscopic methods; absorption lines and bands exist due to the energy spacing of allowed quantum states of electrons. Characteristic

absorption bands exist which indicate the presence of particular chemical bonds and species. Some chemicals have very easily seen absorption, for example the different colours of copper ions due to the different oxidation states of the copper. Absorption bands can sometimes be useful for sensing, but often the absorption bands that would be interesting are too weak or exist at wavelengths that are not easily achieved by the desired light source. It is also not always possible to differentiate chemicals by their absorption bands. Often it is better to use an indicator for an analyte, allowing detection specific to a particular analyte at a convenient wavelength.

Integrated optics and fibre optics have both been applied to sensing using these techniques. Fibre sensing has been achieved using both the fibre tip [17–21] and the evanescent fields [10, 13, 22, 23] to couple light into and out of the sample.

In [10, 13, 22] D-fibre sensors are proposed to measure absorption due to methane gas. Here the efforts were also aimed at increasing the sensitivity of the sensors using high-index films on the flat surface of the fibre. Whilst the sensors in these papers propose to use a monochromatic source at the peak wavelength of the absorption of methane, other sensors have been made which look at a broad spectral range. In [23] sol-gel coated fibres are used which gain their specificity from chemicals immobilized in the sol-gel. They made a pH sensor by cladding a fibre with bromophenol-blue doped sol-gel and measured both its spectral response and the transmitted signal at 590nm wavelength. This work transfers well into integrated optics, where surface waveguides can be used to gain access to evanescent fields.

Work has also been performed using integrated optics. Yang et al. [24] used a doped sol-gel film on a planar waveguide surface to measure gaseous iodine, measuring the absorption at one wavelength due to a charge-transfer complex formed between iodine and phenyl groups immobilized in the sol-gel. In [25, 26] waveguides have been overlaid with indium-tin oxide (ITO) electrodes. ITO is a transparent conductive material which can be deposited by various techniques, including reactive evaporation [25] or sputtering [26]. In both cases a silica buffer layer was deposited between the ITO and the waveguide to reduce the absorption to a convenient level. The resultant waveguide structures were used to spectroscopically monitor electrochemically controlled reactions. In these cases the wavelength control was external to the waveguide chip; [25] used a scanning monochromator, restricting measure-

ments to before and after the reaction, and [26] selected one wavelength for each experiment but was able to monitor at that wavelength throughout the reaction. Bürck et al. [27] used an ion-exchanged channel waveguide with a sensing layer of silicone on the surface. In conjunction with a near-infra red (NIR) spectrometer they measured absorption at characteristic frequencies corresponding to C-H, N-H and O-H bonds and applied this to measuring trichloroethane both in solution and in air.

In recent work [28], input coupling to a waveguide has been achieved via an achromic coupler and the output via a grating which, by focusing onto a CCD array detector acts as an integrated spectrometer. Integrated optical sensors based on characteristic absorption of the analyte or of other indicators for the analyte have been demonstrated and in the future one may expect to see further development of the integrated spectrometers. One does, however, depend on having absorption that can be measured and this is not always the case. There is also a risk in absorption measurements of measuring attenuation due to turbidity or surface contamination rather than due to the desired chemical effect. This is especially true where monochromatic measurements are made rather than spectral measurements.

2.2.2 Refractometry

Changes in refractive index can be measured very precisely, often by interferometric techniques where light is split along two paths and changes in refractive index along one of the paths causes a phase difference which is seen by the interference on recombination. Integrated optical Mach-Zehnder interferometers [9, 29–34] do this using spatially separate paths for the light. This can be done, in a similar way to the bulk optical Mach-Zehnder interferometer, using a beam splitter to divide the light into two sections of waveguide. Their simplest monolithic form consists of two y-junctions — one to split the light into the two paths and one to join the two paths together again. The power output by a sensor formed in this way will vary sinusoidally with linear phase shifts. If one considers the simplest situation, where the smallest variation of power output that can be measured is the same for all output powers, it is clear that at the maxima and minima of output power the smallest detectable phase shift would be at a minimum.

The recombination part of the interferometer can also be modified to include a planar area [33] or a 3-output coupler [9]. These modifications help avoid the sinusoidal variation in sensitivity of the sensor. In the case of the planar device, the phase shift is measured by analysing the interference pattern at the end of the planar region. The 3 output coupler is engineered so that the 3 outputs are 120 degrees out of phase with one another, thus ensuring that one output is always in the sensitive part of its sinusoidal response curve. i.e. all three outputs vary sinusoidally and individually pass through maxima and minima in the output-power variation with phase difference, but at least one channel will be operating well away from its minimum sensitivity at any given time.

There has also been research using difference interferometers [5,35–37] where the difference in phase of transverse electric (TE) and transverse magnetic (TM) modes propagating in the same waveguide is measured. The waveguides are engineered to support only one mode of each polarization. The propagation constant varies by a small amount between the polarizations and they interact unevenly with superstrate media, causing the relative phase of the polarizations to change with superstrate refractive index. The disadvantage of this method is that it still requires several bulk optical components separate from the chip for the measurement of the phase difference. Difference interferometers have been demonstrated with refractive index sensitivity down to 1×10^{-6} refractive index units with improvements to 5×10^{-7} predicted as theoretically atainable [5,37].

Grating couplers have been applied to refractometry by several authors [6,37–41]. The angle at which light couples into/out of a guided mode is dependent on the modal effective index which in turn depends on the media through which the mode is passing. When the superstrate refractive index changes, so does the modal effective index and hence the coupling conditions. Using replicated plastic substrates, formed by pressing in a similar way to compact discs, with waveguides formed by coating with high index dielectric films, complex devices have been fabricated [39–41] that include input and output grating couplers. This technology has the potential for many sensors to be formed on a single substrate and then interrogated individually with a reader head.

Directional couplers [8] can be used to detect changes in complex refractive

index above the coupler region. Similarly to grating couplers, the coupling is very sensitive to changes in effective index of the guided modes. These devices have the advantage that the external componentry can be simpler and, because the devices are built from channel waveguides, there is the potential for many devices to be monolithically integrated and simultaneously interrogated.

Surface plasmon resonance (SPR) sensors [7] can measure changes sample refractive index by their effect on the coupling efficiency into a surface plasmon on the surface of a metal film, which again is due to the superstrate changing the effective index of a mode. In this case the mode affected is the surface plasmon. Devices are designed to operate slightly away from the most efficient coupling into the plasmon so that small changes in effective index cause a large change in coupling efficiency. SPR sensors have great potential for monitoring electrochemical processes because they already possess a suitable electrode, in the form of the metal film.

Refractometers have a notable weakness, which is common to all of them. There are interferences which change refractive index other than concentrations of chemicals or the formation of films on the sensor surface. The refractive index of water changes by approximately 1×10^{-4} with a 1°C change in temperature [38]. Most of the sensors referred to above were designed to operate in an aqueous environment and hence will act as thermometers. Many of these sensors are also aimed at monitoring biochemical processes such as the binding of antibodies to the surface sensor. Antibodies binding to the surface cause a change in refractive index which is indistinguishable from the binding of other impurities. In the application of river water sensing it is known that there are humic acids present in the water which tend to contaminate the sensor surface and can distort the data. The utility of refractometers is therefore limited more by their lack of specificity than by sensitivity.

2.2.3 Fluorescence, luminescence and phosphorescence

Fluorescence, luminescence and phosphorescence are three terms used to describe the emission of light by materials used in chemical sensing. They are generally applied to situations where light is emitted without a significant rise in the temperature of the emitter. The distinction between fluorescence, luminescence and phosphorescence

is not clear and these terms are often used interchangeably in the literature, e.g. the review in [42]. Luminescence does not necessarily imply any absorption of light, for example chemiluminescence where light is emitted as the result of a chemical reaction. Fluorescence is the most rigorously defined term and is used to describe situations where light of one wavelength is absorbed and re-emitted at a different wavelength: for example, ruby absorbs blue/green light and emits red light. The term phosphorescence is used in a similar way to fluorescence, and the choice of a different expression is normally used to emphasize a greater difference in wavelength of absorbed and emitted light or where the lifetime of the emission is especially long.

Fluorescence is often due to a three or more energy level system. Electrons in the ground state are excited to a higher energy level, for example by absorption of a photon carrying precisely the correct amount of energy to make that transition. The absorption band corresponds to this energy transition. It is a band because rather than sharp energy levels there are normally bands of energy levels very close together and hence a range of energies can excite electrons from one band to the other. The excitation is normally followed by a non-radiative shift to a lower energy level, which can be in a different atom, from which there is a radiative transfer back down to the ground state, the fluorescence therefore being at a longer wavelength (lower energy) than the initial absorption. This description is somewhat simplistic, but the salient points are that fluorescence is, in general, at longer wavelength than the initial absorption of light and that an energy transfer occurs in which a photon is not emitted which can be between different atoms. This latter process is the principle of sensors such as in [43] where two dyes are used; an absorber and a fluorescer. This enabled the effect of an analyte (potassium ions) on an absorbing material to be measured by measuring changes in the intensity of emitted fluorescence.

Evanescent wave sensors add an extra dimension of possibility to luminescence sensing. Interaction of the evanescent wave with a thin layer of sample on the waveguide surface is used to excite fluorescence, in common with evanescent absorption sensors. The emitted light can then be collected either externally to the device, or a fraction of the luminescence in the evanescent field region can be collected in the waveguide [44, 45]. If the waveguide has been used to excite fluorescence then the power at the excitation wavelength is often several orders of magnitude higher than

the collected fluorescent power. The fluorescence is generally of a longer wavelength than the excitation, and so can be distinguished e.g. using a filter or spectrometer. Fluorescence is also emitted in all directions, so an alternative collection strategy is to measure the fluorescence propagating in the opposite direction to the pump. Duveneck et al. [46] have demonstrated fluorescence collection both by the excitation waveguide and externally.

Luminescence is characterized by three main parameters: wavelength, lifetime and intensity. Changes in the intensity of the emitted light with a chemical species are in common use [46–51], but the signals measured can be strongly affected by changes in the intensity of illumination, the efficiency of collection or by photodegradation of the luminescent molecules. Fluorescent dyes exist which are easily attached to other molecules as markers, for example antibodies and other proteins can be labelled by standardized techniques. Fluorescent dyes also exist which have their absorption peaks at wavelengths across the visible and into the near infra-red, such as the Cy dyes (cyanine dyes available from Amersham), making these dyes suitable for use with inexpensive semiconductor lasers and detectors. Simultaneous measurement of intensity and wavelength of fluorescence has also been used to give improved specificity in the application of fibre optic zinc sensing [52]. In this case the fluorescence intensity at two wavelengths was measured.

The lifetime of luminescence can be used in some sensing applications to provide a means of determining the concentration of a chemical species. Much of the work on this has been in bulk configurations [53–58] and has been limited by the existence of suitable luminophores for the analytes of interest. The paper by Rolinski and Birch [58] gives a good description of how fluorescence resonance energy transfer (FRET) is now being used in sensing, with emphasis on metal-ion sensing. Many metal ions can cause luminescence quenching, creating problems with lack of specificity. FRET gives a potential route around this problem and has also opened up possibilities for a wider range of analytes which can be measured by lifetime sensing, such as glucose [55, 56]. It is still the case that finding suitable luminophores for lifetime based sensing is harder than intensity based sensing. Lifetime sensing also requires more complicated measurement apparatus including fast electronics for measuring the fluorescence emitted after a short pulse of illumination. However,

developments in both the instrumentation and the chemistry are making the necessary instruments cheaper and reducing the speed requirements of the instruments by producing luminophores with longer lifetimes.

2.2.4 Summary

Fibre optic sensors and integrated optical sensors have been used for detecting a wide range of analytes using the full range of techniques based on absorption, refractometry and luminescence. All of these methods have advantages and disadvantages and all depend on finding an optically detectable test for the analyte of interest. Refractometers, whilst having the potential for great sensitivity, suffer greatly from a lack of specificity. With refractometers care must be taken not only to exclude various contaminants from the sensors, but also to temperature stabilize the sensors for the greatest sensitivity. The work in this thesis was performed with the application of the European RIANA project in mind. In RIANA, specificity to the analytes of interest is gained from antibodies which bind to the surface of the sensor to a degree determined by the analyte concentration. Labelling the antibodies with fluorescent dye stands out as the simplest method for detecting the bound antibody and for developing sensors which can simultaneously measure at several positions on one chip. Measurement of the intensity of the fluorescence as opposed to lifetime was also chosen for simplicity; much less development was needed to produce a system where the analyte concentration affects the number of fluorophores bound at the sensor surface than to produce a system within which the analyte significantly alters the lifetime of the fluorophores bound at the sensor surface. The cost of this choice is that care must be taken to ensure that the data are not affected by ffuctuations in excitation intensity, collection efficiency or photodegradation of the dye.

2.3 The European Union River Analyser project

2.3.1 Project goals

The European Union RIver ANAlyser, or RIANA, project was a three year research project dedicated to developing a multi-analyte sensor for pollutants in river water.

The project goals, as expressed by the project consortium [59] were:

- The use of a single sample to detect a plurality of analytes; two separate panels of six analytes were chosen for the purpose of this project.
- A generic approach allowing the user to choose a panel of analytes from a large number of analytes available.
- A simple generic sample handling protocol for multi-analytes.
- A rapid measurement system; the aim was 15 minutes or less per cycle time.
- A low-cost system in terms of hardware, consumables and disposables.
- The capacity for system automation for use in on-line monitoring applications.
- A highly sensitive optical transduction scheme (Limits of detection targeted are 1ppb initially and below 0.1ppb with the final version of the system).

The project partners and their involvement break down as follows: The Institute of Physical and Theoretical Chemistry, Eberhard-Karls Universität Tübingen, provided surface chemistry and the auxiliary ligand system. The Optoelectronics Research Centre at the University of Southampton performed optical transducer development. Perkin-Elmer GmbH, the instrument manufacturer contributed experience of making a testbed instrument. Compagnie Generale des Eaux and Centro De Investigacion Y Desarrollo were involved as end users. GEC Marconi were a major sub-contractor on the project and developed most of the antibodies used in the course of the project.

To meet the objectives the partners chose to use antibodies for analyte recognition. A system was devised which allowed the panel of analytes to be varied by using a system of auxiliary ligands. It was decided before the project started to use antibodies labelled with fluorescent markers and to base the measurements on the intensity of the fluorescence rather than the lifetime. The optical transducer went through two main stages of development. The first stage was a bulk total internal reflection fluorescence (TIRF) chip. This operated by reflecting a laser beam down a glass slide. The reflections of the laser beam occured at discrete elliptical spots

which were used for sensing. The evanescent wave at the reflection spots excited fluorescent dye in the surface layer and the resultant fluorescence was collected through the chip by large core size (1mm), high numerical aperture (NA), polymer optical fibre. The bulk TIRF chip allowed the chemistry to be developed separately while integrated optical transducers were being developed. Similarly, the integrated optical transducers were tested on a simplified subset of the chemistry, using antibodies which were already known to function well and without the auxiliary system.

The remainder of this chapter will introduce in more detail the concepts behind the immunochemistry and will describe how this was used within RIANA. The transducers have to operate within the whole system and so the requirements of RIANA and the restrictions this placed upon transducer development are discussed.

2.3.2 Immunosensing in RIANA

To achieve the desired specificity of the sensors, antibodies are raised which have a high affinity for the analyte. This is normally achieved by raising an antibody to an analyte derivative — a large molecule which resembles the analyte, sometimes produced by attachment of analyte molecules to larger proteins. The use of the analyte derivative is often necessary because the analyte molecules are too small to produce an immunological reaction. For RIANA many of the antibodies were produced by injecting sheep with the analyte derivatives and then harvesting the antibodies that are produced by the sheep's immune system. The antibodies are then tested for affinity to the analyte, purified and used for sensing. Care has to be taken in this process as analyte derivatives are different to the analytes and so antibodies can have a much higher affinity for the derivative than for the analyte. In RIANA the analyte derivative is immobilized on the sensor surface, via an auxiliary ligand in the case of the final system, and then a binding inhibition assay is performed. Figure 2.1 is a representation of how a binding inhibition assay works.

The sample of water is mixed with antibodies and incubated for a short time to allow the antibodies to bind to the analyte. The sample is then pumped over the surface on which the analyte derivative has been immobilized. Antibody molecules have a limited number of binding sites and so cannot bind to the analyte if their binding sites are occupied by analyte molecules. The analyte therefore inhibits the

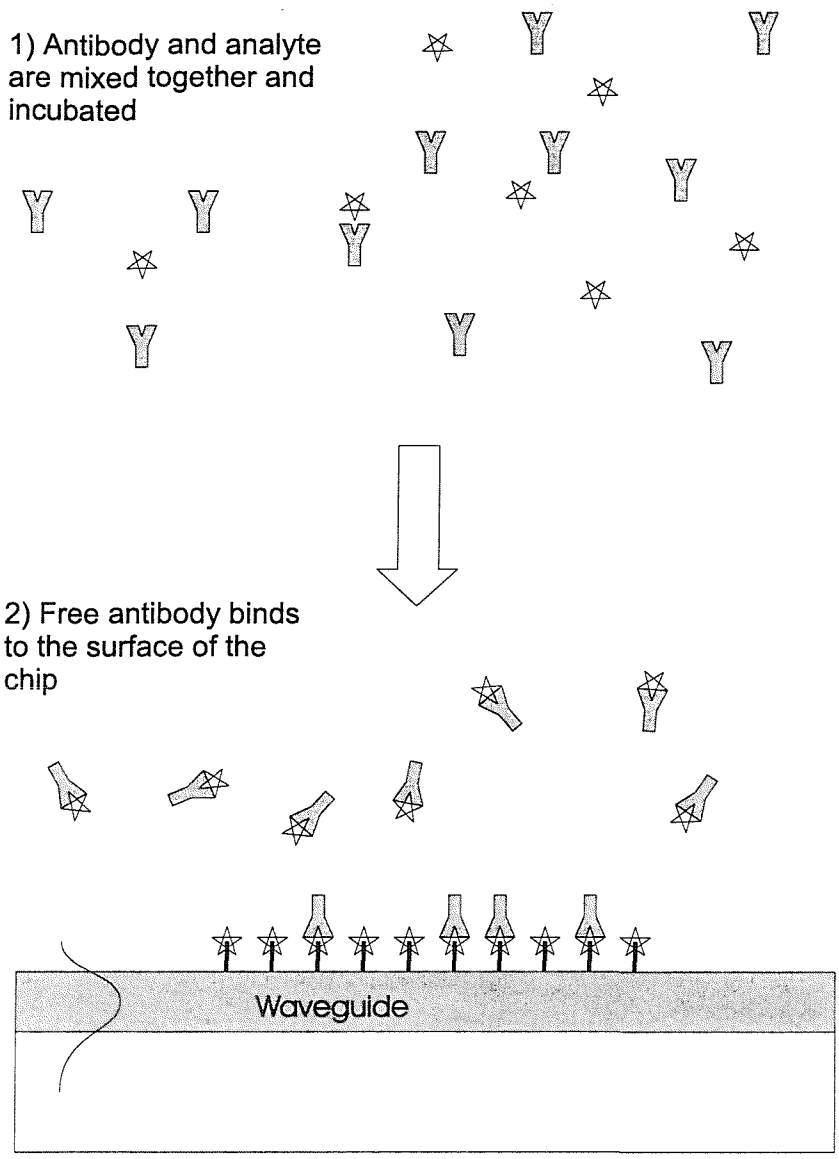

Figure 2.1: Format of competitive binding immunoassay

binding of the antibodies to the modified surface. The lower the concentration of analyte, the more antibody is free to bind to the surface and so the higher the intensity of the collected fluorescence. Generally the antibody concentration is chosen so that the surface loading is much less than a complete monolayer, even when no analyte is present.

The sensor surface can then be regenerated using standard techniques, for example by pumping through pepsin solution. This removes the antibody from the sensor surface without significantly affecting the surface modification of the surface. The sensor can thus be used many times without significant degradation of the surface; in the course of this work chips were regenerated in excess of 200 times without it

being necessary to renew the surface modification.

In the final RIANA system, chips are used which are modified to bind to different auxiliary ligands at each measurement spot. To this are bound the auxiliary molecules which carry the analyte derivative. In this way, by changing the auxiliaries used, the analyte at each sensing spot can be changed from test cycle to test cycle without modifying the chip. To test the antibodies and the transducers it is desirable to decouple any effects seen from the auxiliary system. For testing purposes, analyte derivative was immobilized directly to the chip without the auxiliary and only one analyte was measured.

2.3.3 Overview of RIANA system

The system breaks down into the following parts:

- the antibodies, raised to be specific to the analyte and labelled with fluorescent dye
- the fluid delivery system, to deliver the samples and reagents to the transducer
- the transducer chip, the platform to which the surface chemistry is attached
- the surface chemistry
- the fluorescence collection and detection system
- the light source, modulated and with a shutter
- lock-in amplifiers, to pick out the part of the detected signal modulated at the same frequency as the light source
- a computer, to control the experiment and to acquire data

As previously stated, RIANA aimed to produce a low-cost, portable solution of sufficient sensitivity to measure a panel of analytes to the sensitivities required by statute. In most cases this was at a level as low as 0.1 parts per billion. The final panel of analytes was:

- atrazine

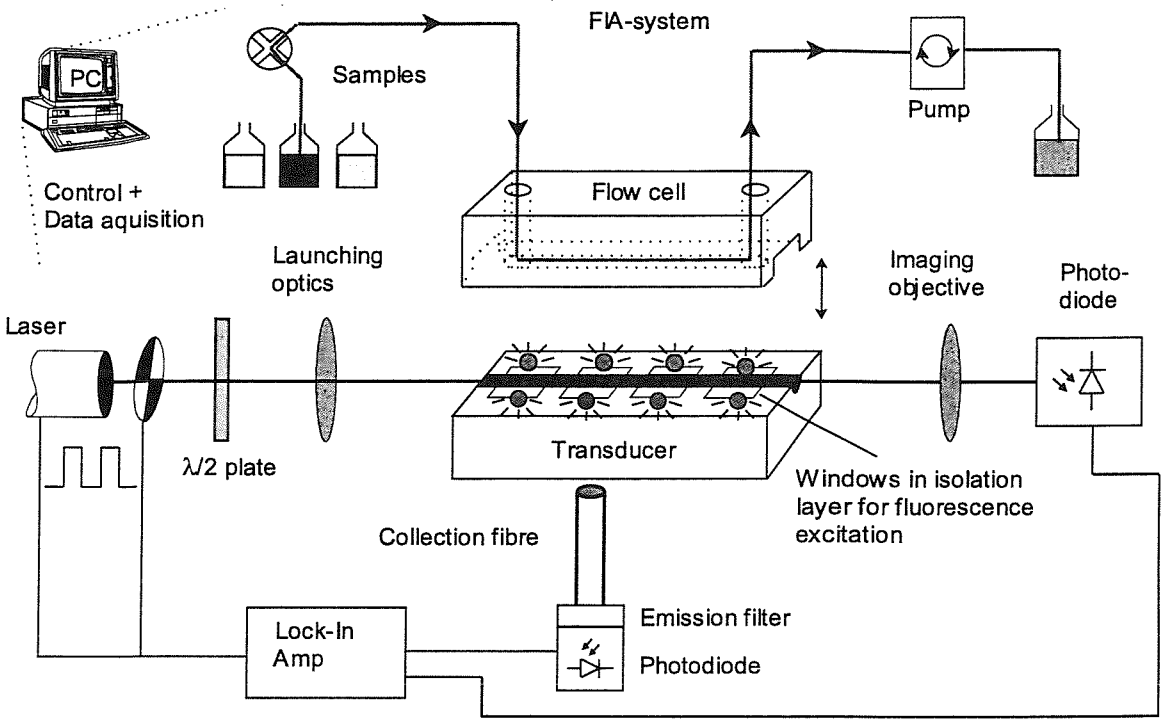

Figure 2.2: RIANA System

- simazine
- deethylatrazine
- isoproturon
- dimethylphenyl urea compounds
- pentachlorophenol
- 2,4,6-trichlorophenol
- 2,4-dichlorophenoxy acetic acid
- methyl-chloro-phenoxypropionic acid
- paraquat
- alachlor
- hydroxycarbufuran
- glyphosate

- toluene
- nonyl phenol

As is clear from the above, the complete system is complex and so in the course of the project each part of the system had to be individually tested. For example, it would have made little sense to try to test the optics in conjunction with the biochemistry fo the whole panel of analytes as it would have proved difficult to discriminate between effects due to the optics and due to variations the behaviour of the chemistry.

The final RIANA system uses low-cost components which for much of the development work were not used, but instead commercially available components of known reliability were used. The format of test cycles has remained fairly constant throughout to allow comparison.

The principle of operation is that light guided in the transducer, whether bulk TIRF chip or integrated optical waveguide, excites dye in the evanescent fields. The dye fluoresces in all directions and so some of the fluorescence passes through the chip. Large diameter (1mm), high NA fibre is used to collect the fluorescence and carry it to a filter and the detectors. The filter is used to remove any radiation at the pump wavelength and background fluorescence. The laser illumination is chopped, mechanically in early devices and later electronically. A sync signal is passed to lock-in amplifiers which receive the signal from the detectors. In this way, only the part of the signal which is fluctuating at the frequency of the sync is amplified and so the effect of background noise is reduced. The output of the lock-in amplifiers is passed to a PC for data acquisition. The fluid system is used to pump phosphate buffered saline containing through the flow cell. Into this flow plugs of other liquids can be injected, such as the sample or reagents for regenerating the transducer surface.

The transducers were made from soda-lime glass. The integrated optical transducers had channel waveguides formed by potassium-sodium ion-exchange in potassium nitrate at 400°C. Some of these chips also incorporated thin films of tantalum pentoxide, Ta_2O_5, on the surface which were used to increase the strength of the evanescent fields. Some of the chips also had isolation layers made from Teflon AF 1600, Teflon FEP or silica. After the initial fabrication of the chips, the group in

Tübingen modified the surface with the analyte derivative using a standard procedure. Prior to modification, the surface was cleaned by immersion in freshly prepared piranha (H_2O_2 : $H_2SO_4, 2$: 3) for 30 minutes and then rinsing in de-ionized water and drying at room temperature. 30μl of 3,Glycidyloxypropyl-trimethoxysilane (GOPTS) was applied to the dried surface and left to react for 1.5 hours in a nitrogen atmosphere. The silanised surface was then rinsed with dry acetone and dried with nitrogen. Aminodextran dissolved in water at a 2:1 ratio was then dropped on the silanised surface and left for 6 hours to couple. Activation of the silica surface with GOPTS helps to provide a surface that the aminodextran can bond to. Analyte derivatives dissolved in dimethylformamide (DMF) were attached to remaining amino-groups of the dextran using DIC. The aminodextran blocks non-specific binding to the sensor surface whilst supporting a high density of specific binding sites for the antibody. To produce multiple sensing spots for different analytes, or for use with the auxiliary system, instead of applying the aminodextran and the derivatives in separate steps, amino esters of the derivatives were mixed with the aminodextran in 50:50 water:DMF and applied with a microdrop dispenser [59]. For the purposes of transducer development this extra level of complexity was not needed or used.

The format of a test cycle is as follows. Antibodies in phosphate buffered saline (PBS), with ovalbumin at 100 times the antibody concentration, are added to a sample of water which may contain the analyte. The ovalbumin is a protein which will bind to surfaces in preference to the antibody. Alternatively fish gelatine has been used by other partners in the project. The antibodies are given some time, normally a few minutes, to bind to analyte molecules in the sample. Before injecting the sample into the flow-cell, a baseline measurement is taken. This should be a measurement just of the light due to any scattered pump-radiation or background fluorescence. The sample is then pumped over the surface of the transducer where free antibodies stick. In the course of the project, photobleaching of the dye was found to be a problem and so the laser is switched off while the sample is injected until rinsing of the flow cell commences. After the fluorescence has been measured the antibodies are removed from the sensor surface using firstly pepsin in PBS (pH 1.9) and then a mixture of water, acetonitrile and propionic acid in the ratio 50:50:1.

During investigation of the performance of the sensors, rather than the sample solutions described above, samples such as bulk solutions of dye in PBS, blank antibody samples and samples of antibody with standard solutions of analyte were used. Bulk dye solutions are used to evaluate the sensitivity to fluorescent molecules without the complication of the binding process. The test cycles with bulk dye are simpler because the laser does not need to be switched off during injection and no regeneration is necessary other than rinsing. Blank solutions of antibody (i.e. no analyte present) are useful in that they present the most reproducible scenario in which the antibodies bind to the surface. This allows investigation of the reproducibility of measurements in the presence of the problems associated with using dye labelled antibody.

2.3.4 Requirements of RIANA

As well as functional requirements for transducer chips, RIANA also imposed other restrictions. RIANA needed as low a total system cost as possible, removing the possibility of taking advantage of exotic materials or processes. To reduce the cost of the system, other workers within the project developed electronics for lock-in detection of optical signals. These lock-in amplifiers are much lower cost than commercial lock-in amplifiers (sold as stand-alone units) and some of this saving can be attributed to dispensing with many extra features found in commercial units. Unsurprisingly though, the RIANA electronics do not yet offer the same performance as the commercial lock-in amplifiers.

Another constraint discovered within RIANA is that the fluorescent dyes used are subject to rapid photo-bleaching when they are bound to the surface of a waveguide. This occurs without high index films being used to increase the power density in that region. It was anticipated that the addition of high index films would increase the rate of photo-bleaching substantially. This led to fears that the total amount of fluorescence per unit area that can be collected from a bound layer is fixed, and that making the photo-bleaching occur more rapidly would simply lead to increased variations in measured responses due to the reduced integration times.

Much of this thesis is dedicated to investigating the use of thin high index films to increase evanescent field strengths. The material chosen for this was Ta_2O_5. The

surface modification of the chips has been optimized for a silica surface and so there were concerns that the Ta_2O_5 would not provide a surface to which the chemistry would bond reliably, which needed to be investigated.

For an integrated optical transducer to be useful, these factors must be no more significant than for the bulk TIRF chips and the transducer must offer something extra to justify the extra cost. The choice of forming waveguides in soda-lime glass gives one of the cheapest routes to channel waveguide structures with low loss. The use of high index films offers a potential method for increasing the sensitivity of sensors based on such waveguides. In this thesis the practicality of using high index films is investigated in light of the requirements of the project.

Chapter 3

Theoretical description of high-index film enhancement of waveguide sensitivity

3.1 Introduction

The main focus of this chapter is a numerical model of multi-layer planar waveguides and the effect of the waveguide parameters on the irradiance distributions in the guide. The first section of this chapter is a brief discussion of the different approaches to this problem and why the matrix approach used here was chosen. More detailed discussions of the theory can be found elsewhere, e.g. [1, 60–62], and are not duplicated here.

The second section is concerned with the verification of the model both by producing dispersion curves and modal irradiance plots of the correct form and by calculating the eigenmodes of example guides to be the same as those found by other authors. This is performed for structures with a small number of layers and for graded index structures as approximated by a multilayer staircase approximation.

The next section is concerned with using the model to predict the gains in sensitivity possible in certain kinds of planar waveguide sensor by applying high index films to the surface. It is shown that the enhancements mentioned by Stewart and Culshaw [11] are easily achievable in theory, although the practical constraints they mention still exist.

The method of overlap integrals has been used to predict the waveguide losses induced by transitions between different regions of waveguides. The discussion focusses mainly on the loss induced by the presence of high index overlays on the surface of the waveguides at the transition between coated and uncoated waveguide regions.

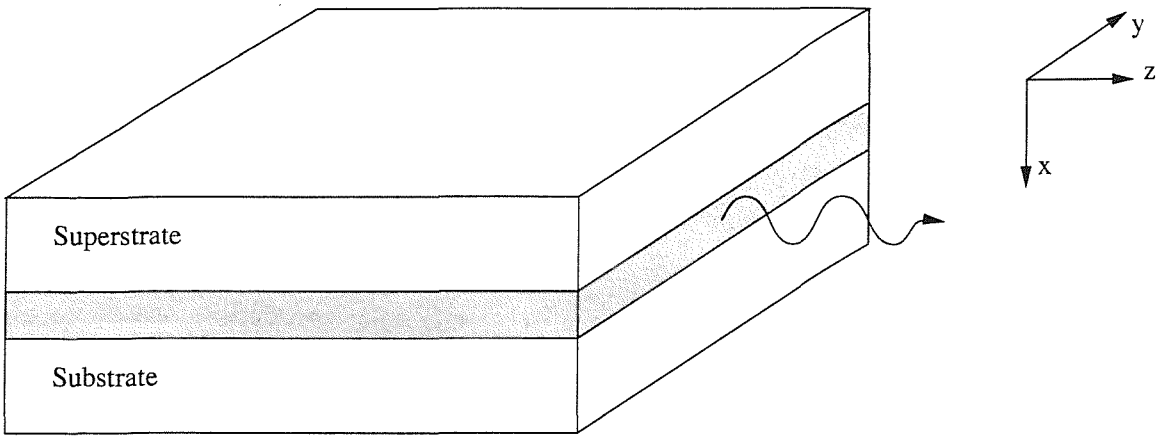

Figure 3.1: A slab waveguide

A short section on the operation of a Mach-Zehnder interferometer is included followed by a short summary with conclusions.

It is intended to use light sources at or around the helium neon laser wavelength of 633 nm for the experimental work as this leads directly to work on fluorescence based sensors excited at this wavelength. The choice of laser wavelength was a compromise. The integrated optical components are easiest fabricated to work with infra-red wavelengths due to good availability of cheap laser light sources, low attenuation optical materials and because features can be larger with longer wavelengths of light. The fluorescent dyes that can easily be attached to proteins are most commonly available for working with ultra-violet illumination. Within the RIANA project it was decided to use light at HeNe and diode lasers at and around 633nm wavelength. All the modelling was performed at 633 nm wavelength unless otherwise stated.

3.2 The numerical model

The structure under examination here is a planar slab waveguide. This consists of three or more parallel planar layers of dielectric material. For simplicity, the orientation of the stack is chosen such that the interfaces between layers are parallel to the y-z plane as indicated by figure(3.1).

By defining the system in this way, the problem reduces to solving the wave-equation in the x-direction only.

In the j^{th} layer

$$\mathsf{E}(x,y,z,t) = E_j(x)e^{i(\omega t-\beta z)} \tag{3.1}$$

where β, the propagation constant (in the z-direction) can be written, using a ray optical approach, as

$$\beta = n_j k_0 \sin\theta_j \tag{3.2}$$

θ_j is the angle of incidence of a ray in the jth layer with the y-z plane.

This yields

$$E_j(x) = E_j^+ e^{-i\alpha_j x} + E_j^- e^{i\alpha_j x} \tag{3.3}$$

$$\alpha_j = (n_j^2 k_0^2 - \beta^2)^{\frac{1}{2}} \tag{3.4}$$

Similar expressions can be written for the magnetic fields. Equation (3.3) can also be written:

$$E_j(x) = A_j \sin(\alpha_j x) + B_j \cos(\alpha_j x) \tag{3.5}$$

and

$$E_j(x) = A_j e^{\alpha'_j x} + B_j e^{-\alpha'_j x} \tag{3.6}$$

for α_j pure real and pure imaginary, respectively. α'_j is simply the imaginary part of α_j.

The boundary conditions are that the tangential components of the E and H fields must be continuous across the interfaces. There exist discrete values of β for which the light is confined to the waveguide, i.e. the fields outside the guide are decaying. From equation (3.6) it can be seen that the decay corresponds to imaginary values of α_j and is exponential.

At this point it is necessary to choose notation. There is a potential computational advantage in using the real number notation of equations (3.5) and (3.6), but only if the refractive indices of all the layers and hence the values of β and α_j are real. It being desirable to be able to calculate the attenuation caused by absorbing layers, complex refractive indices were to be used. Hence, implementation was simpler using the complex notation of equation (3.3). This approach was used in [11, 63], the other notation was used in [64, 65].

Chilwell and Hodgkinson [66] chose to calculate the tangential components of both the electric and magnetic fields for both positive and negative going waves.

Since, if necessary, the magnetic fields can be calculated from the electric fields, this was deemed unnecessary.

For the chosen system of notation we have the wave equation (3.3) in each layer and the boundary conditions at the interfaces. Following Ghatak et al. the equations can be rewritten in matrix form as:

$$\begin{bmatrix} E_j^+ \\ E_j^- \end{bmatrix} = \frac{1}{t_j} \begin{bmatrix} e^{i\delta_j} & r_j e^{i\delta_j} \\ r_j e^{-i\delta_j} & e^{-i\delta_j} \end{bmatrix} \begin{bmatrix} E_{j+1}^+ \\ E_{j+1}^- \end{bmatrix} = \mathbf{S}_j \begin{bmatrix} E_{j+1}^+ \\ E_{j+1}^- \end{bmatrix} \tag{3.7}$$

where $\delta_j = \alpha j d_j$, d_j is the thickness of layer j and $r_j$and t_j are the Fresnel reflection and transmission coefficients, given by (for TE polarized light):

$$r_j = \frac{\alpha_j - \alpha_{j+1}}{\alpha_j + \alpha_{j+1}} = \frac{n_j \cos\theta_j - n_{j+1} \cos\theta_{j+1}}{n_j \cos\theta_j + n_{j+1} \cos\theta_{j+1}} \tag{3.8}$$

$$t_j = \frac{2\alpha_j}{\alpha_j + \alpha_{j+1}} = \frac{2n_j \cos\theta_j}{n_j \cos\theta_j + n_{j+1} \cos\theta_{j+1}} \tag{3.9}$$

for TM polarized light $r_j$and t_j become

$$r_j = \frac{n_{j+1}^2 \alpha_j - n_j^2 \alpha_{j+1}}{n_{j+1}^2 \alpha_j + n_j^2 \alpha_{j+1}} = \frac{n_{j+1} \cos\theta_j - n_j \cos\theta_{j+1}}{n_{j+1} \cos\theta_j + n_j \cos\theta_{j+1}} \tag{3.10}$$

$$t_j = \frac{2\alpha_j}{\frac{n_{j+1}}{n_j}\alpha_j + \frac{n_j}{n_{j+1}}\alpha_{j+1}} = \frac{2n_j \cos\theta_j}{n_{j+1} \cos\theta_j + n_j \cos\theta_{j+1}} \tag{3.11}$$

From equation (3.7) we can write

$$\begin{bmatrix} E_0^+ \\ E_0^- \end{bmatrix} = \mathbf{S}_1 \begin{bmatrix} E_1^+ \\ E_1^- \end{bmatrix} = \mathbf{S}_1\mathbf{S}_2 \begin{bmatrix} E_2^+ \\ E_2^- \end{bmatrix} = \ldots = \mathbf{S} \begin{bmatrix} E_N^+ \\ E_N^- \end{bmatrix} \tag{3.12}$$

Equation(3.12) shows that the fields in the superstrate (layer 0) are related to the fields in the substrate (layer N) by a simple 2×2 matrix. The guidance condition is for the fields in these two layers to be exponentially shrinking with distance from the guide. By setting the value of E_N^+ to zero and finding the appropriate value of β the value of E_0^- can be zeroed. This corresponds to making the element s_{22} of the matrix $\mathbf{S}$ equal zero. Muller's method [67] was used to find the roots of $s_{22}(\beta)$. Other authors [11,63,64] have achieved this a different way — by simulating prism coupling and finding the resonance peaks. This has only been done by scanning through real

values of β and treating the imaginary part as a perturbation. By using Muller's method, the model can find roots much further from the real axis but there is a potentially much greater computational cost. This follows the choice earlier to use the complex notation for the fields. Since modern computers are fast and normally have plenty of memory, the extra computational cost of the fully complex approach is justifiable because it allows the model to simulate a greater range of waveguides. Care is needed in using Muller's method, though, as it is not always convergent.

3.3 Validation of the model

From equations (3.5) and (3.6) it is clear that, in the superstrate and substrate regions of the guide, we expect to see exponential fields and in the guiding layers we expect to see sinusoidal fields. A good first check as to whether or not the program was working was to plot the fields for the modes of some example guides, as found by the program. Figure (3.2) shows the TE modes of an example guide. The form of the modes is exactly as was expected. This guide was just one of the ones used for comparing this model with a model written by Pascal Mauron [68]. His model is specific to three-layer waveguides and makes use of this to provide a simple eigenvalue equation which is solved numerically using the Newton-Raphson method. The theory is well described in text books, e.g. [1, 60, 61]. The results of the two models are compared in table (3.1) and are in close agreement.

In the paper by Anemogiannis and Glytsis [69], they compare the results from their model with those published by Chilwell and Hodgkinson [66] for a six layer lossless guide and a similar guide with losses. Apart from a mistake in [66] of a factor of 10 in the imaginary part of the effective index in the lossy guide, there is very good agreement between [66,69] and the model presented here. The results from this model and from [69] are presented in tables(3.2, 3.3). The irradiance distributions of the four TE modes of the lossless six-layer guide are shown in figure(3.3). As well as total agreement with the published data on the location of the modes in effective index, the mode profiles are also as expected. Chilwell and Hodgkinson, [66], give the field amplitude cross-sections in their paper. These are essentially the square-root of the irradiance and are in agreement with the results in figure(3.3).

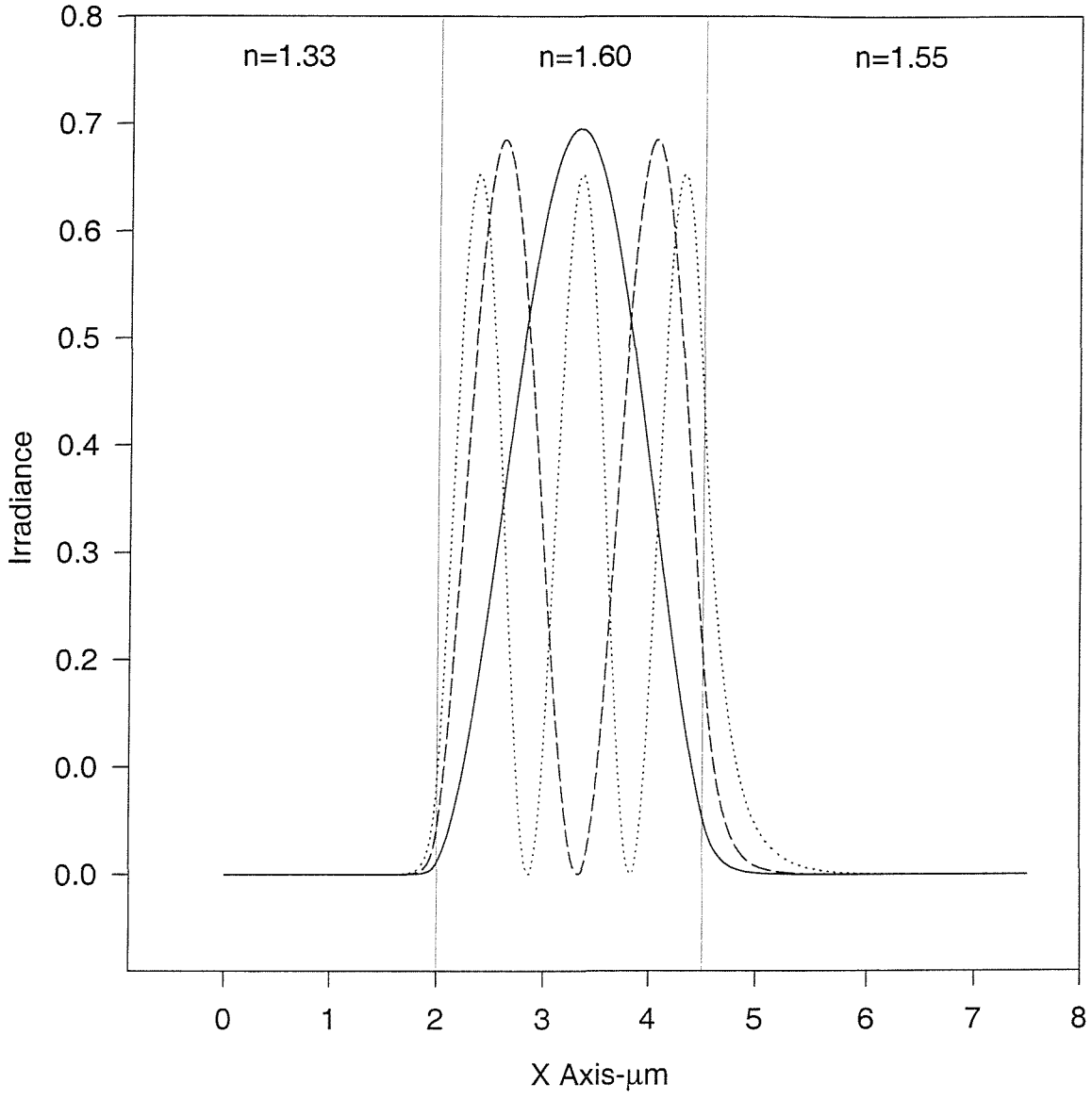

Figure 3.2: Irradiance distributions for the TE modes of a three layer guide

Thickness μm	Mode #	PM's n_{eff}	n_{eff}
2.5	2	1.566483	1.566483
	1	1.584876	1.584876
	0	1.596199	1.596199
2.0	2	1.552942	1.552942
	1	1.577991	1.577991
	0	1.594432	1.594432
1.5	1	1.565535	1.565535
	0	1.591086	1.591086
1.0	0	1.583606	1.583606
0.5	0	1.562819	1.562819

Table 3.1: Comparison of results with those from Pascal Mauron's model for a guide with index 1.6, superstrate index 1.33, substrate index 1.55

Mode	n_{eff} from [69]	n_{eff}
TM_0	1.6200313	1.620031318
TM_1	1.5947884	1.594788478
TM_2	1.5549806	1.554980690
TM_3	1.5018178	1.501817805
TE_0	1.6227286	1.622728682
TE_1	1.6052756	1.605275698
TE_2	1.5571361	1.557136152
TE_3	1.5035871	1.503587112

$n_0 = 1.0$, $n_1 = 1.66$, $n_2 = 1.53$, $n_3 = 1.60$, $n_4 = 1.66$, $n_5 = 1.5$

$d_1 = d_2 = d_3 = d_4 = 0.5\mu m$

Table 3.2: Comparison with published results for 6 layer guide

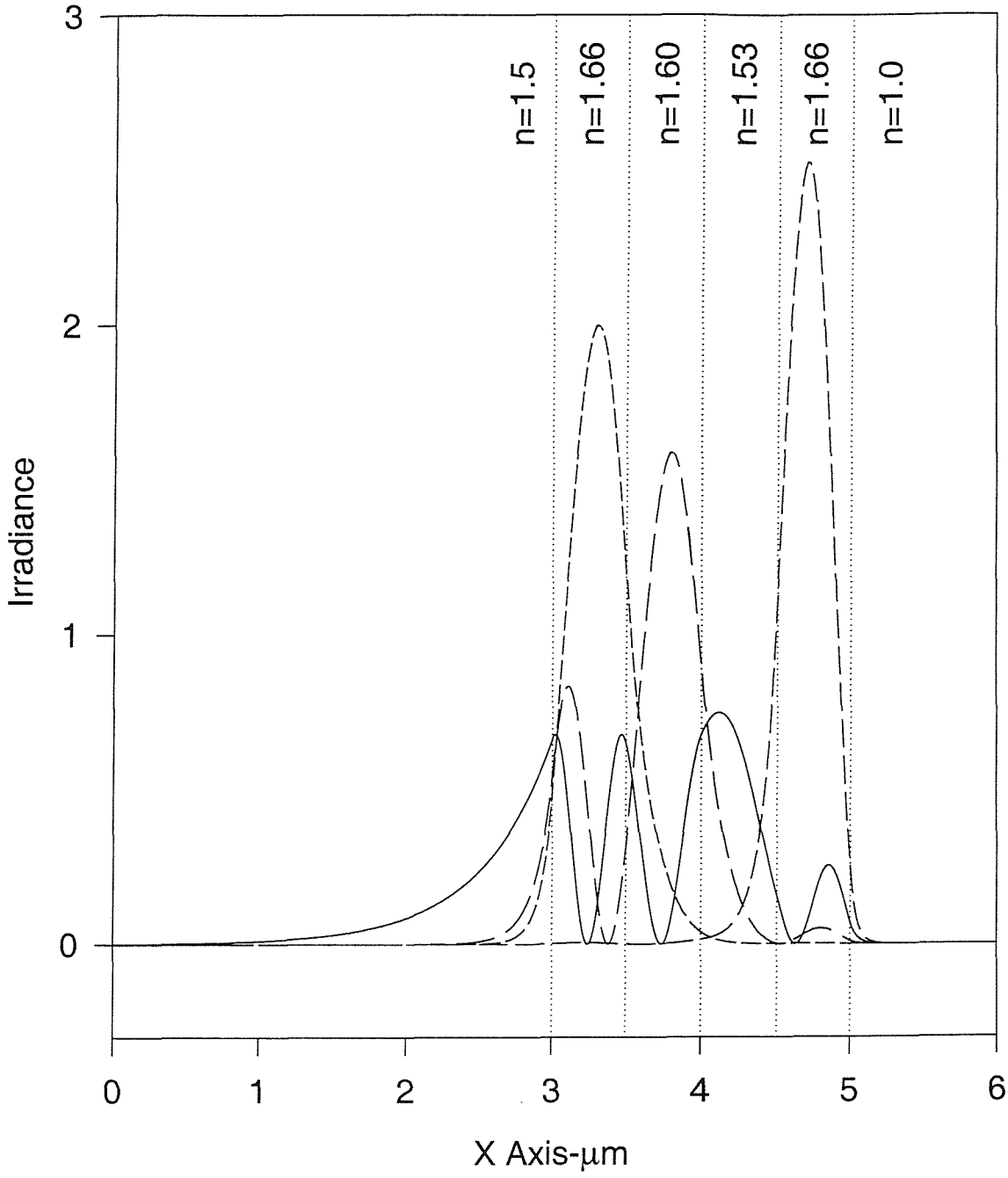

Figure 3.3: Mode profiles of the example six-layer guide

Mode	$Re[n_{eff}]$ from [69]	$10^4 Im[n_{eff}]$ from [69]	$Re[n_{eff}]$	$10^4 Im[n_{eff}]$
TM_0	1.6200313	0.00892	1.620031317	0.0089276
TM_1	1.5947884	1.65565	1.594788475	1.6556527
TM_2	1.5549806	0.23704	1.554980665	0.2370483
TM_3	1.5018176	0.42530	1.501817641	0.4253004
TE_0	1.6227286	0.00673	1.622728680	0.0067373
TE_1	1.6052756	1.66244	1.605275698	1.6624429
TE_2	1.5571361	0.20880	1.557136125	0.2088010
TE_3	1.5035869	0.55032	1.503586965	0.5503250

$n_0 = 1.0$, $n_1 = 1.66 - i1.66 \times 10^{-4}$, $n_2 = 1.53 - i1.53 \times 10^{-4}$, $n_3 = 1.60$, $n_4 = 1.66$, $n_5 = 1.5$

$d_1 = d_2 = d_3 = d_4 = 0.5\mu m$

Table 3.3: Comparison with published results for 6 layer absorbing guide

Dispersion curves for the first two TE modes of two different 3 layer asymmetric guides guides are given in figures(3.4, 3.5). These graphs are both of the well known forms to be found in the text books, e.g. [60].

In summary, the model produces graphs of the expected forms and numerical values which agree with published results.

3.4 Multilayer approximation to graded index waveguides

This computer model has also been applied to finding the modes of graded index structures using a multilayer staircase approximation. This approximates a smoothly varying index profile by a series of discrete layers, each of constant refractive index. This is illustrated in figure (3.6)

Results using the multilayer staircase approximation are compared with exact results and WKB approximation from the paper by Gedeon [70]. Comparisons are given in tables (3.4, 3.5, 3.6) for three index profiles.

$$n^2(x) = n_s^2 \cdot \Delta n \cdot e^{-\frac{x}{a}} \tag{3.13}$$

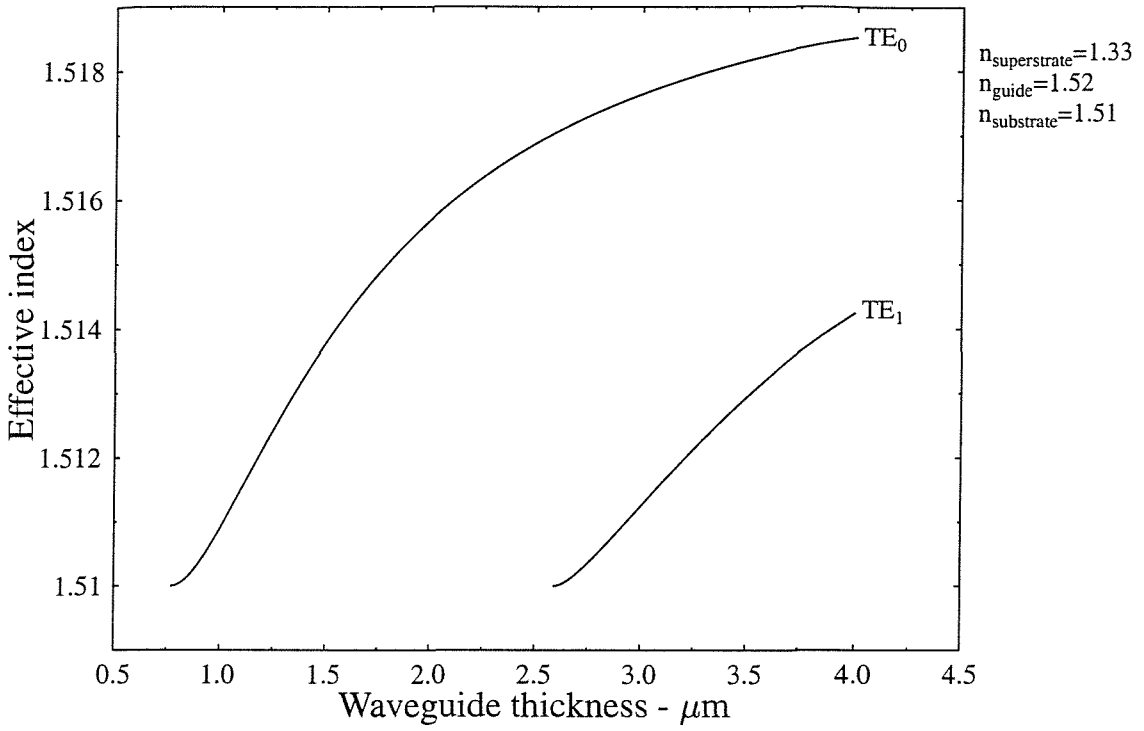

Figure 3.4: Dispersion curves for a 3 layer guide

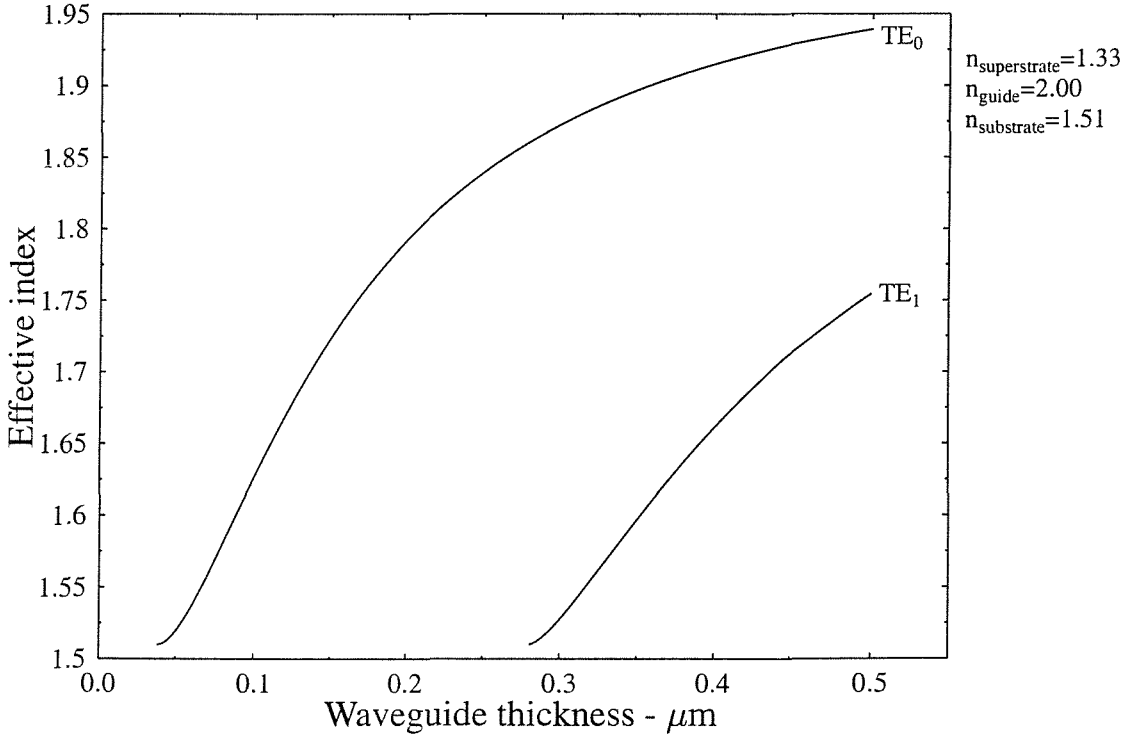

Figure 3.5: Dispersion curves for a three layer guide

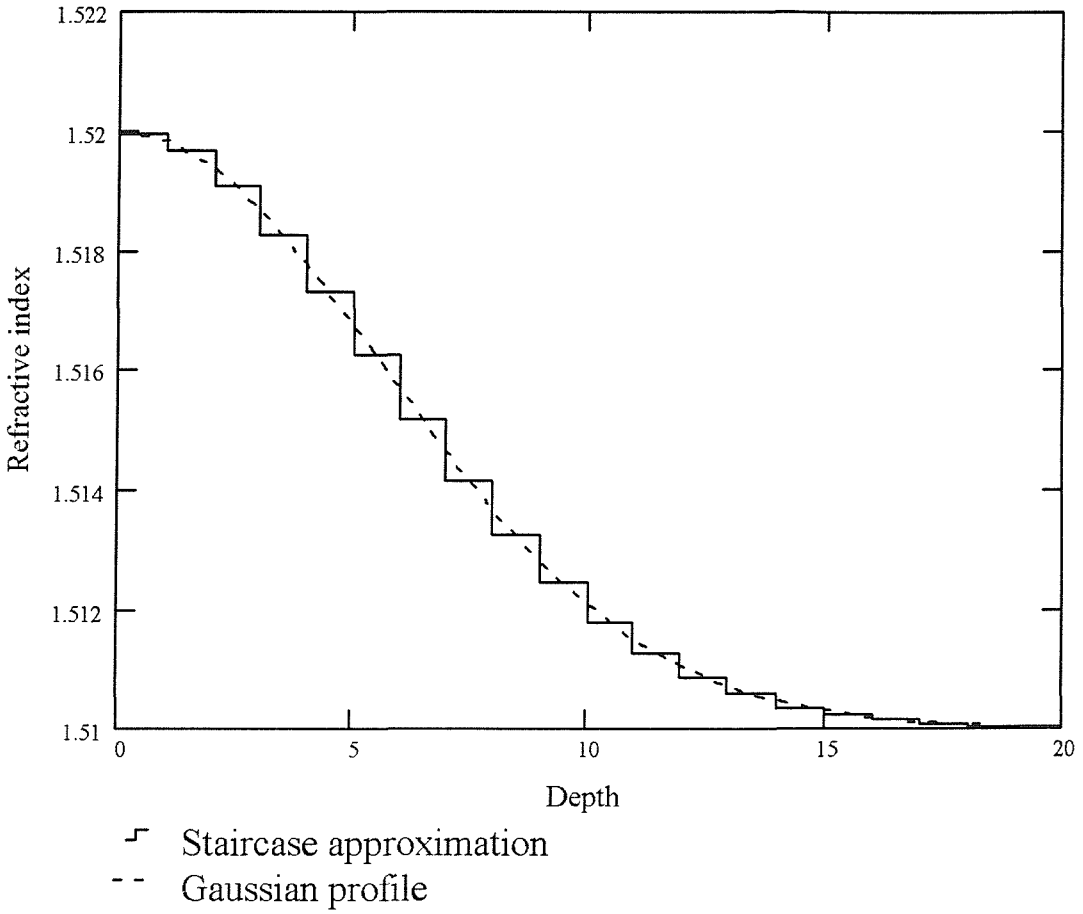

Figure 3.6: Multilayer staircase approximation to a Gaussian index profile

Mode	$n_{eff} = \beta/k_0$		
TE	Exact	WKB	Staircase
0	2.24135	2.24160	2.241386
1	2.22070	2.22075	2.220705
2	2.20680	2.20680	2.206799
3	2.19675	2.19675	2.196763
4	2.18940	2.18940	2.189419
5	2.18415	2.18415	2.184131
6	2.18050	2.18050	2.180497
7	2.17825	2.17825	2.178240
8	2.17715	2.17715	2.177169

Table 3.4: Comparison between staircase approximation and published results for the refractive index profile in equation (3.13)

$$n^2(x) = \left(n_s + \Delta n \cdot e^{-\frac{x}{a}}\right)^2 \tag{3.14}$$

$$n^2(x) = \left(n_s + \Delta n \cdot e^{-\frac{(x-d)^2}{a^2}}\right)^2 \tag{3.15}$$

n_s is the unperturbed index of the substrate, a and d are constants expressed in microns and Δn is a measure of the maximum refractive index perturbation.

Mode	$n_{eff} = \beta/k_0$		
TE	Exact	WKB	Staircase
0	2.24275	2.24290	2.242830
1	2.22160	2.22160	2.221656
2	2.20745	2.20740	2.207450
3	2.19725	2.19715	2.197215
4	2.18980	2.18970	2.189731
5	2.18440	2.18430	2.184343
6	2.18070	2.18060	2.180632
7	2.17835	2.17830	2.178315
8	2.17720	2.17715	2.177180

Table 3.5: Comparison between staircase approximation and published results for the refractive index profile in equation (3.14)

Mode	$n_{eff} = \beta/k_0$		
TE	Exact	WKB	Staircase
0	1.58935	1.58925	1.589330
1	1.57775	1.57765	1.577731
2	1.56680	1.56670	1.566767
3	1.55635	1.55650	1.556336
4	1.54620	1.54705	1.546198
5	1.53625	1.53580	1.536255
6	1.52680	1.52655	1.526788
7	1.51850	1.51830	1.518459
8			1.512633

Table 3.6: Comparison between staircase approximation and published results for the refractive index profile in equation (3.15)

3.5 Enhancement of the evanescent field

In general, integrated optical chemical sensors make use of the interactions of evanescent fields with the materials they pass through for their operation. Stewart and Culshaw use the enhancement in sensitivity of an evanescent wave methane sensor by the addition of a high index overlay as a modelling example in their paper [11]. They theoretically predict enhancements of greater than an order of magnitude for their example sensor, which is a four layer planar structure with an absorbing superstrate. This is clearly of great interest for developers of integrated optical sensors.

It is expected that in practice the overlay would have losses of its own, due to scattering and impurities, which would limit the length over which a device could be coated. The high index layer also will cause transition losses between the uncoated and coated regions.

Figure (3.7) shows the irradiance (optical power per unit area) enhancements predicted by this model. Irradiance was chosen as the best physical quantity to model for various reasons. It is the logical quantity to model when considering absorbing materials for example, as absorption is quoted in terms of power transmittivity. Looking at the variations in the distributions of irradiance in waveguides gives a more direct indication of the interaction of guided light with the materials that comprise the waveguiding structure for all types of sensor. The power carried by the various modes of different waveguiding structures was normalised such that the integral of irradiance across the waveguide for any given mode was equal to 1 (in arbitrary units).

The plot shows, for two different thicknesses of guide, the irradiance at the surface for TE modes normalized to the same arbitrary power. This plot also shows another potential problem for overlayed guides; the thicker the guide is, the closer it is to supporting two modes and so the overlay does not have to be as thick to produce a second mode in the guide. The $1\mu m$ thick guide is much further from supporting two modes than the $2\mu m$ guide, as can be seen from figure(3.4). The effective index of the TE_0 modes increases as the overlay thickness increases. For the $1\mu m$ guide it reaches 1.52 at $0.0435\mu m$ overlay and for the $2\mu m$ guide it reaches 1.52 at $0.042\mu m$. This is the point at which the mode is being guided in the overlay, the fields are exponentially decaying in the layer below. The transition to this point

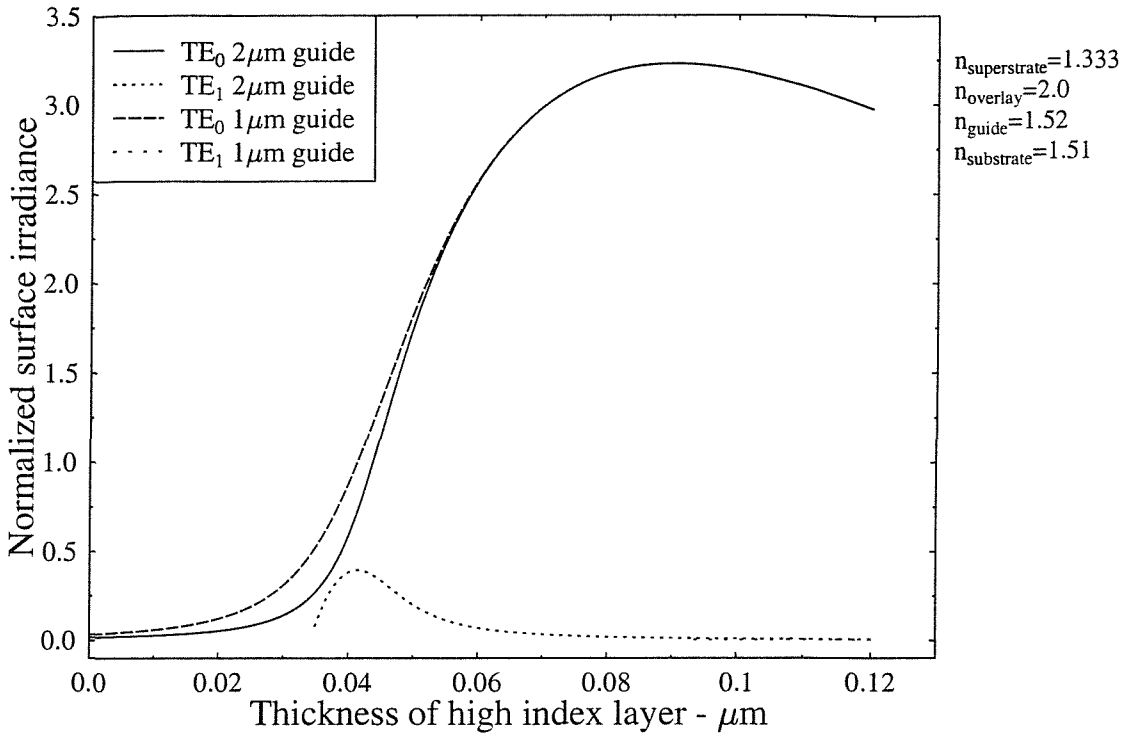

Figure 3.7: Variation of irradiance at the superstrate-guide interface with thickness of high-index layer

is shown for the $1\mu m$ guide in figures(3.8, 3.9). A line has been added to these plots to indicate the position of the interface with the superstrate. These plots show how the irradiance at the surface is increased by the addition of the extra layer. The factor by which the irradiance at the superstrate-guide interface is enhanced is plotted, for the $1\mu m$ guide, in figure(3.10).

Some devices, e.g. Mach Zehnder interferometers, detect changes in refractive index of the superstrate by making use of the change of the effective index of the modes that this causes. The enhancement of evanescent fields increases the interaction with the superstrate and it is therefore expected that this will increase the sensitivity to the superstrate index. Figure(3.11) is a plot showing how the rate of change of effective index with superstrate index varies with thickness of overlay. This follows a similar form to the irradiance enhancement. Also on this plot is the curve for the TM mode. The sensitivity increase for a given overlay thickness is less at first, but the peak is in a different place and is higher. For the TM mode the effective index does not reach 1.52 until the overlay is $0.074\mu m$ thick, as compared with $0.0435\mu m$ for the TE mode. This may be a disadvantage since the losses

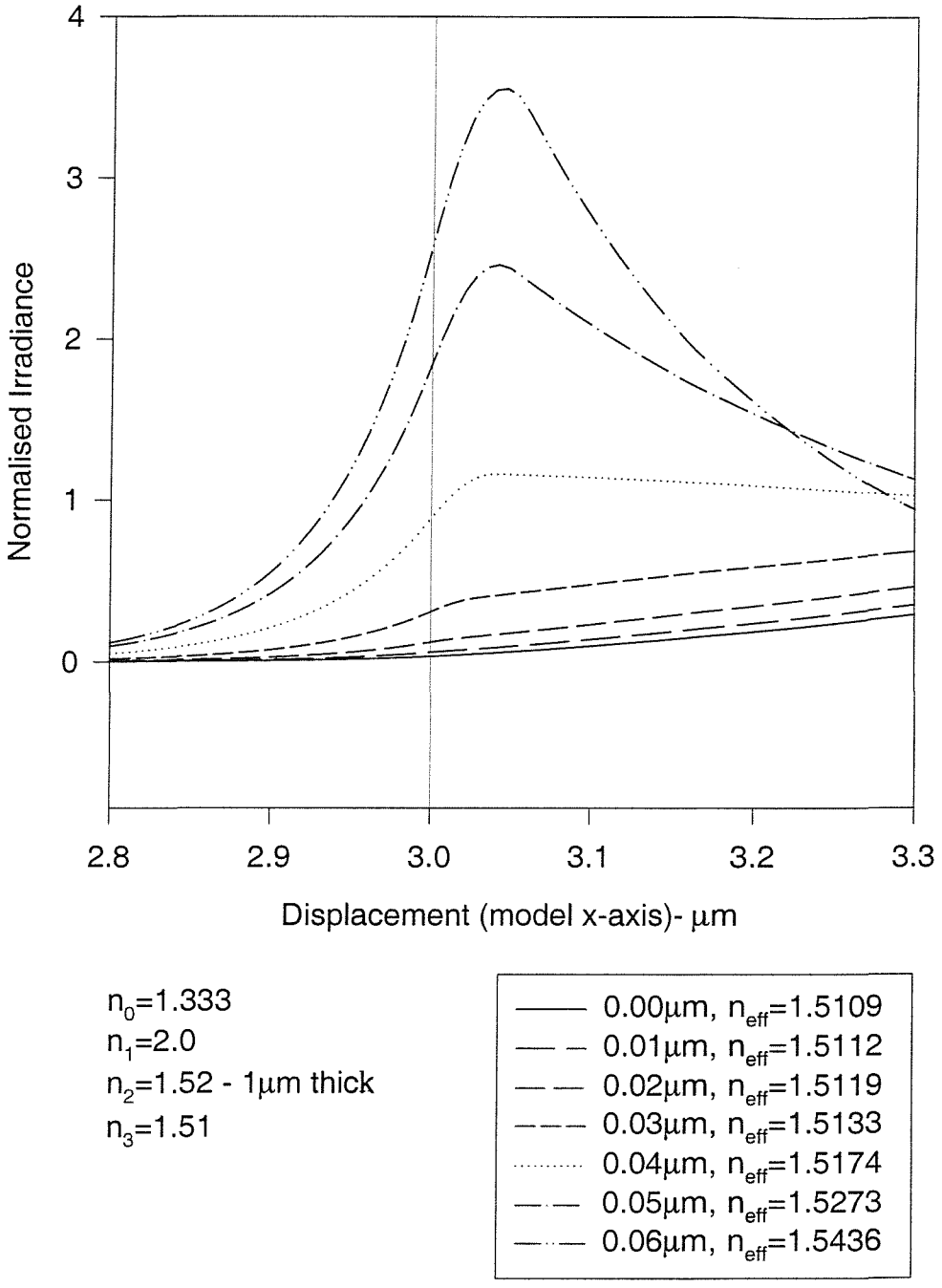

Figure 3.8: Irradiance distributions of TE_0 modes of a 4-layer guide for various thicknesses of high-index layer

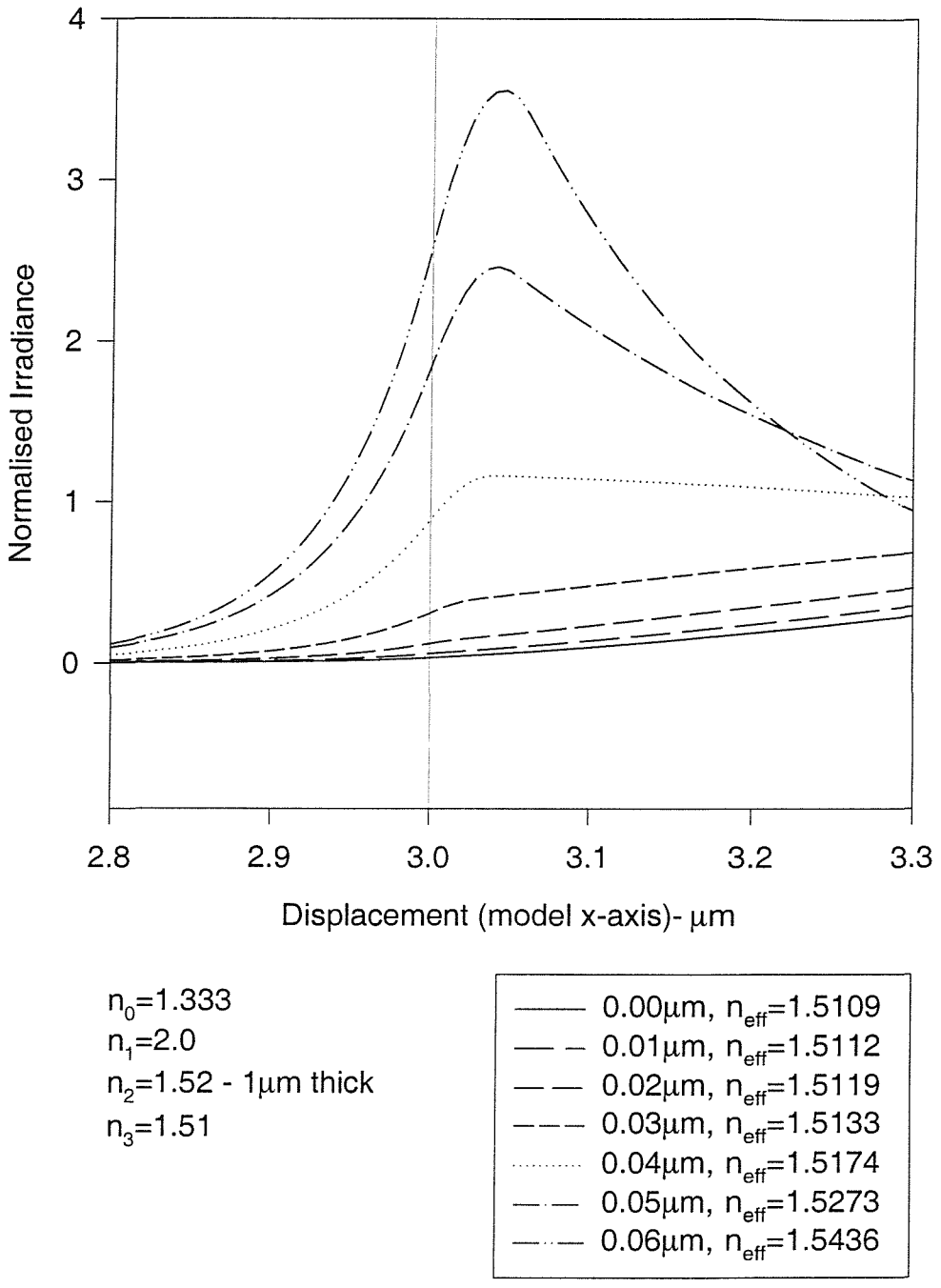

Figure 3.9: Irradiance distributions of TE_0 modes of a 4-layer guide —zoomed on the superstrate-guide interface

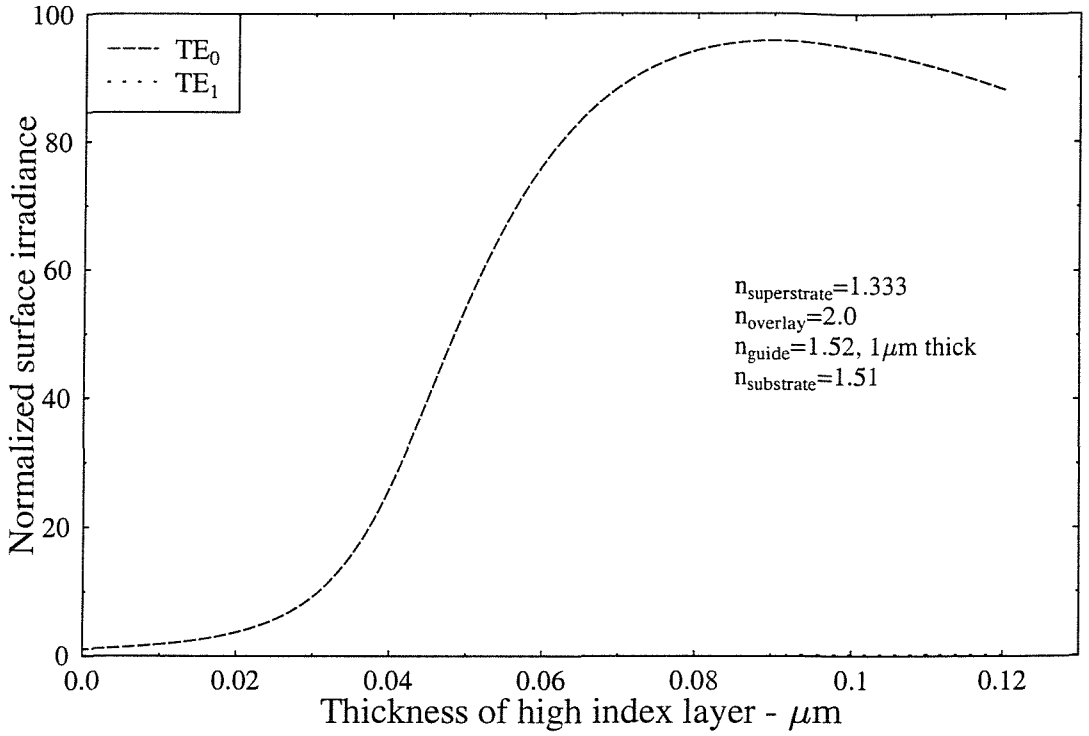

Figure 3.10: Enhancement of irradiance at the superstrate-guide interface with thickness of high-index layer

involved in having a thicker film would probably be greater.

Many chemical sensors work by observing changes in the absorption of a reagent as it reacts with another chemical. By putting a layer of material on top of a waveguide and measuring the loss of the waveguide the absorption of the material can be deduced. The sensitivity of such a device would be greater if the loss due to a given layer of a given material could be maximized. Figure (3.12) shows how the addition of a high index overlay increases the loss caused by a $0.1\mu m$ thick film of an absorbing material. The imaginary part of the refractive index was chosen as 0.0001 of the real part, following [66, 69](as in table 3.3). The form of this curve is, again, like that of figure (3.10).

The sensitivity to optical properties of thin films on the surface of a waveguide is related to the irradiance at the surface, but the sensitivity to the bulk superstrate is dependent on the proportion of the modal power carried by the superstrate evanescent fields. The enhancement factors for the two scenarios are plotted in figures(3.13, 3.14) for various thicknesses of a range of different refractive index overlays. As was observed earlier, the light becomes guided by the overlay when the effective index

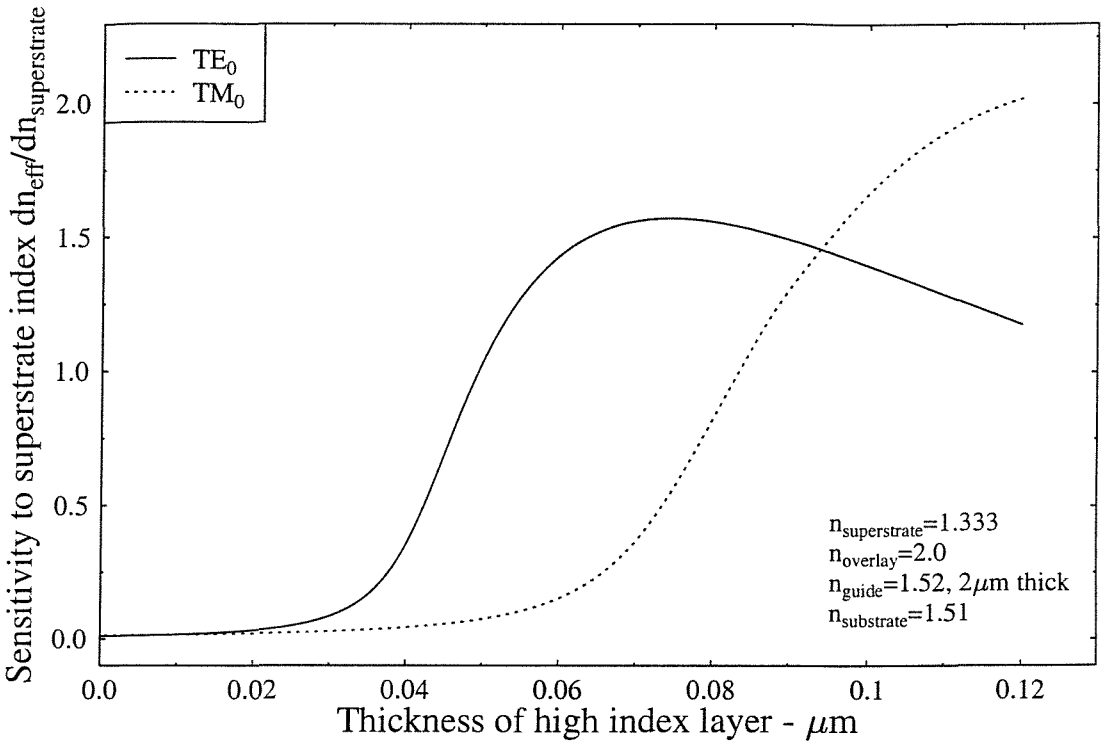

Figure 3.11: Effect of a high-index film on sensitivity to superstrate index

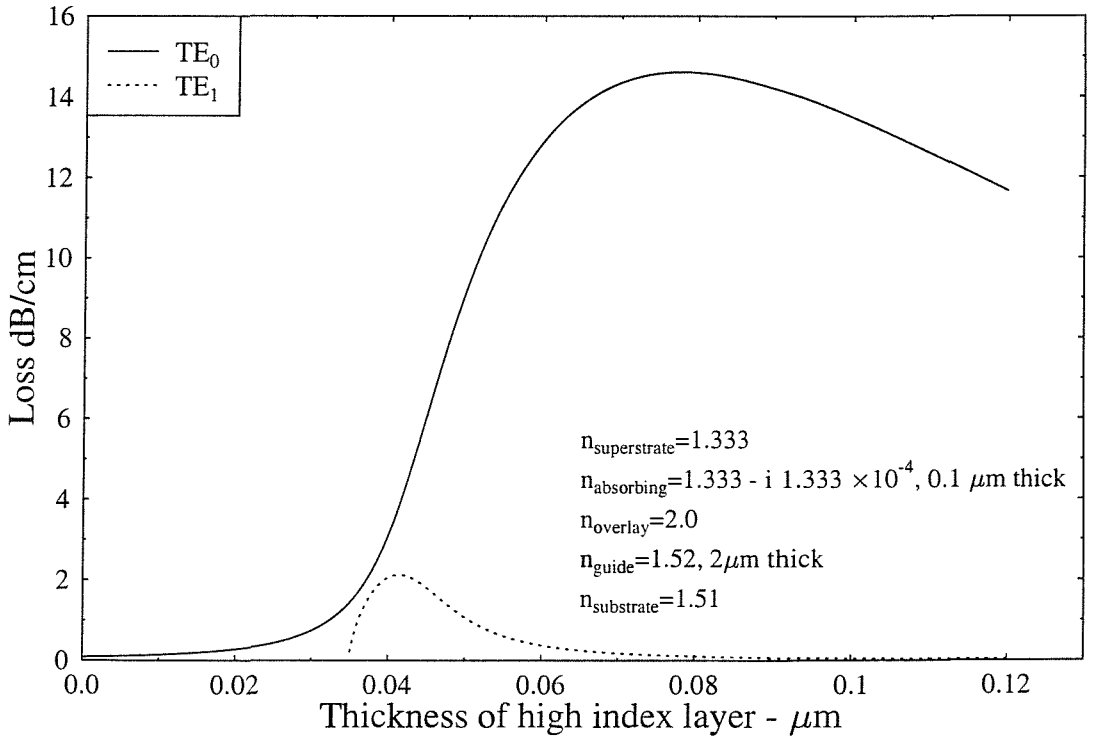

Figure 3.12: Variation of loss in an absorbing structure with thickness of high-index layer

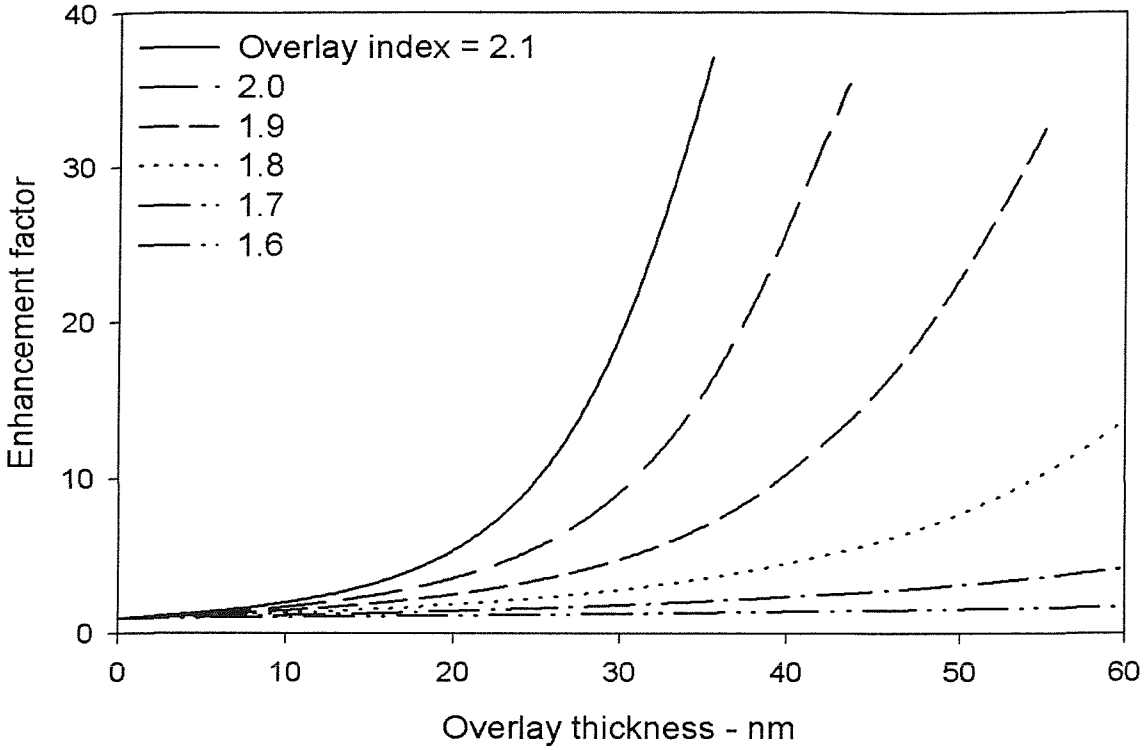

Figure 3.13: Enhancement of surface irradiance by high index films

of the mode exceeds the refractive index of the underlying waveguide. The curves have been truncated at this point. These graphs show that the same general form and approximately the same values of enhancement factor are predicted for thin film and bulk sensors with high index overlays. The enhancement factor increases with the refractive index of the overlay, but the maximum film thickness that can be used before the film starts guiding becomes smaller.

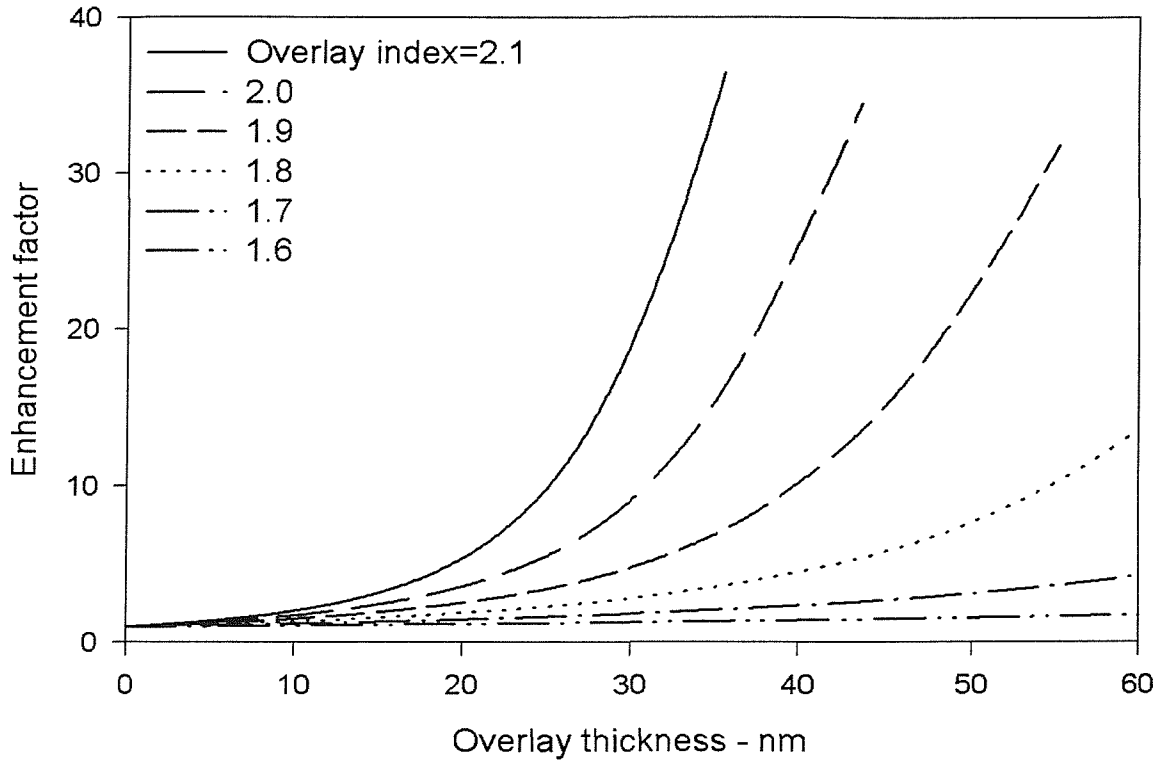

Figure 3.14: Enhancement of power carried by superstrate evanescent fields by high index films

3.6 Coupling of guided modes across an interface

3.6.1 Overview of theory

The previous section investigates the potential benefits from overlaying a waveguide with a thin high index film. The change in mode profile caused by such an overlay is predicted to increase the sensitivity of an integrated optical sensor. This film in practice may not cover the whole length of the waveguide, in which case there will be an interface between coated and uncoated regions. The difference in mode profile and propagation properties mean that the coupling from the guided mode in one waveguide to that in the other will be less than 100%. It would be advantageous to be able to estimate the losses that will be generated from such interfaces and other waveguide discontinuities as may be caused by other changes in the waveguide structure. For the purposes of modelling the structures of interest to this research it is sufficient to use approximations such as weak guidance (low numerical aperture waveguides) and fully real refractive indices. It is also beyond the scope of this thesis to develop a model which fully considers back-reflections, radiation modes and leaky modes.

The coupling efficiency of a given start field into a guided mode can be calculated by overlap integrals. From chapter 6 of Syms and Cozens [1], we write the amplitude coupling coefficient from a general electromagnetic field into the νth guided mode of a waveguide as:

$$a_\nu = \iint_A [\mathbf{E} \times \mathbf{H}_\nu^* + \mathbf{E}_\nu^* \times \mathbf{H}] \cdot \mathbf{k}\, dx\, dy / \iint_A [\mathbf{E}_\nu \times \mathbf{H}_\nu^* + \mathbf{E}_\nu^* \times \mathbf{H}_\nu] \cdot \mathbf{k}\, dx\, dy \quad (3.16)$$

The waveguide model only deals with planar waveguides, so the integration with respect to the y-variable is dropped. Looking at the case of TE polarization and substituting the relevant field components yields [1]:

$$a_\nu = \int_{-\infty}^{\infty} E_y E_{\nu y}\, dx / \int_{-\infty}^{\infty} E_{\nu y}^2\, dx \quad (3.17)$$

This can be written in inner product notation as:

$$a_\nu = \langle E_y, E_{\nu y} \rangle / \langle E_{\nu y}, E_{\nu y} \rangle \quad (3.18)$$

In [1] they continue to considering the case of coupling from the fundamental TE mode with electric field E_{0y} to the fundamental mode in a second waveguide with electric field E'_{0y}. Defining the coupling efficiency, η, as the ratio of output power to input power, they obtain:

$$\eta = |\langle E_{0y}, E'_{0y}\rangle|^2 / \langle E_{0y}, E_{0y}\rangle \langle E'_{0y}, E'_{0y}\rangle \tag{3.19}$$

Whichever units are chosen, it then clearly simplifies matters greatly if the normalization of all modes is such that $\langle E_{0y}, E_{0y}\rangle = 1$, yielding:

$$\eta = |\langle E_{0y}, E'_{0y}\rangle|^2 \tag{3.20}$$

Within the same approximations it can be shown that for TM modes:

$$\eta = |\langle E_0, E'_0\rangle|^2 \tag{3.21}$$

In the latter case the variable E is used to represent the amplitude of the electric field rather than just the transverse component of the amplitude. The weak guidance approximation has the two take the same value.

3.6.2 Verification of the mode coupling model

The model established following the above theoretical description does not need to be highly accurate for the intended purpose of guiding the design of optical chips. It was still necessary to check that the implementation of the model does at least agree with examples presented in texts such as, e.g. Syms and Cozens [1]. The models use the trapezium rule for integration and so the accuracy is highly dependent on the number of points used. 1000 points was selected as being more than adequate for the simple structures under consideration here.

The most basic checks are best performed considering the coupling of light from an example waveguide to an identical waveguide. First consider the coupling of a mode to the same mode of an identical waveguide which is in perfect alignment, i.e. there is no transition. In this case the coupling should be 100% efficient and hence $\eta = 1$. In a similar situation, but considering the coupling between two different modes we expect no coupling and hence $\eta = 0$. The model passes these tests within

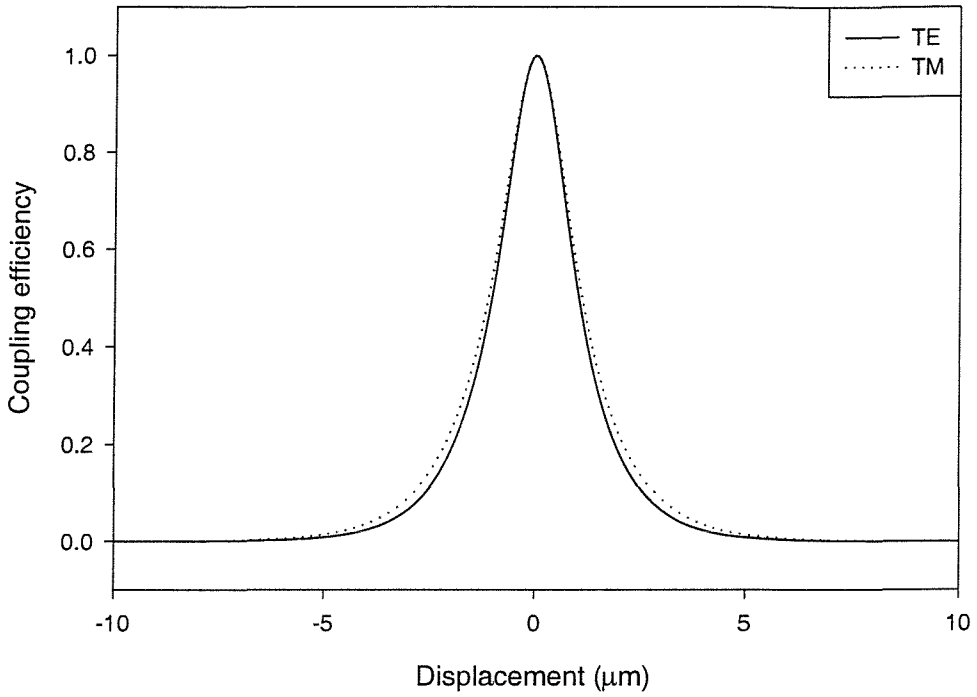

Figure 3.15: Variation of the coupling efficiency between identical single moded waveguides with displacement parallel to the interface

the numerical inaccuracies one might expect — the model gave exactly $\eta = 1$ for the first case and $\eta \approx 1 \times 10^{-15}$ for the second. Here a double moded waveguiding structure consisting layers with refractive indices 1.33, 1.52 and 1.51 was used. The waveguiding layer (n=1.52) was 4μm thick.

Another interesting test of the model is to look at the variation of coupling efficiency with a varying offset between two identical waveguides. Figure (3.15) shows the result of altering the relative positions of two identical single moded waveguides, refractive indices as above with the guiding layer 1μm thick.

As expected, the coupling efficiency reaches unity when the relative displacement zero. The figure also shows both TE and TM polarizations, giving a broader curve for the more dispersed TM mode.

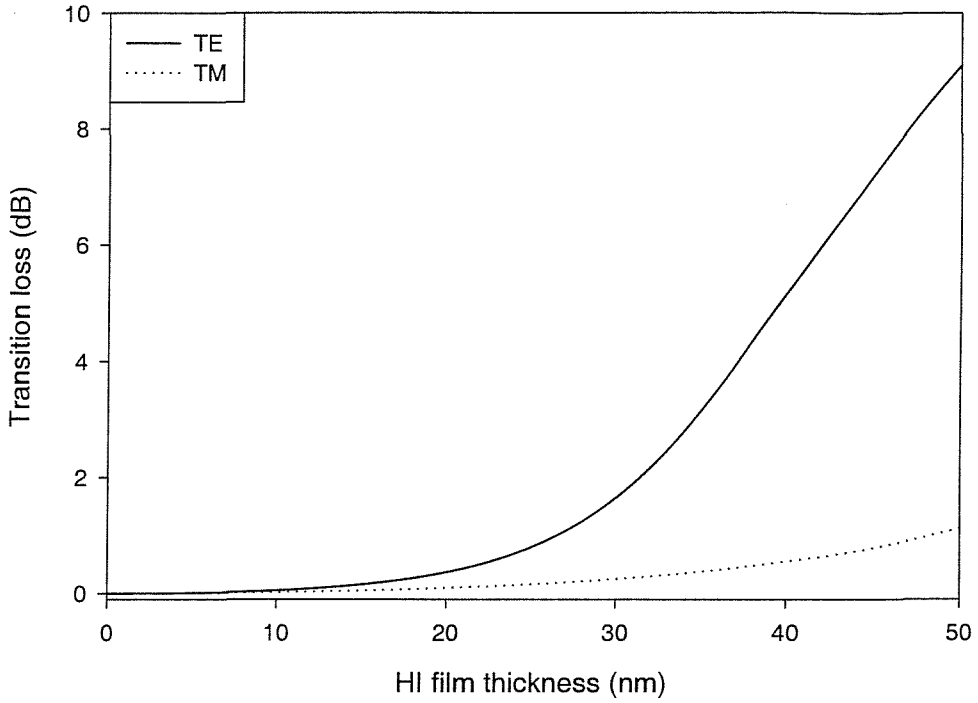

Figure 3.16: Variation with overlay thickness of the transition loss going from non-overlaid waveguide to waveguide with high index overlay of refractive index 2.1

3.6.3 Predictions of the mode coupling model

The main purpose of modelling the coupling of modes across interfaces was to examine the loss induced going from a non-overlaid piece of waveguide to one with a high index overlay. Earlier it was shown that the addition of a thin film of high index material to the surface of a waveguide alters the distribution of light in the guided modes to have a greater proportion carried in the superstrate evanescent fields, as illustrated in figure (3.8). Shown in figure (3.16) is the coupling efficiency going from a 1μm thick waveguide of refractive index 1.52, superstrate index 1.33, substrate index 1.51, to an identical waveguide in perfect alignment with the addition of an overlay of refractive index 2.1.

From the modelling it can be seen that a 30nm film of refractive index 2.1 would cause a loss of 1.6 to 1.7 dB due to the transition between the coated and uncoated waveguide. The same film can be estimated from the modelling in figure (3.14) to

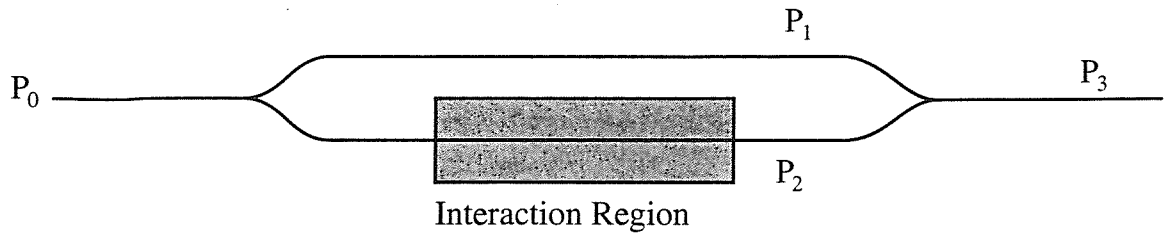

Figure 3.17: An integrated optical Mach-Zehnder interferometer

increase the power carried in the evanescent fields by a factor of 20 and so would be expected to provide an increase in sensitivity of a sensor by more than an order of magnitude despite the transition losses.

It is common when constructing sensors to use a film of a low refractive index material to prevent direct interaction of the waveguide with the sample except in a defined interaction region. At either end of this interaction region there will be a transition from uncoated to coated waveguide and hence a loss. To estimate how large the loss is the example waveguide above was modelled, but this time using a transition to waveguide coated with 1μm of a material with refractive index 1.46 (approximately the refractive index of silica). The model predicts a loss for this situation of 0.1 dB. This loss is small compared with the loss predicted for high index films and is not regarded as a great concern.

3.7 Operation of integrated optical Mach-Zehnder interferometer

The Mach-Zehnder interferometer, in the form it most commonly appears in in integrated optics, consists of two y-junctions as shown in figure(3.17). The first divides the light down two paths and the second re-combines the light from the two paths. If the two paths are of equal optical path-length then the signals interfere constructively on recombination and the output power is equal to the input power, less any losses in the splitting and in the waveguides.

The losses can be divided into symmetric and asymmetric losses. A symmetrical loss source will reduce the amplitude of the output signal, but the signal will still reach zero at π phase difference. Asymmetry in the loss means that at π phase shift

the two signals cannot fully cancel each other out. The minimum in the combined output will be greater than zero. This can be shown by looking at the guidance of light by the two arms of the interferometer in terms of symmetric and asymmetric supermodes. A detailed description of the passage of light through y-junctions can be found in texts such as [1].

Consider the device in figure(3.17). There may be a symmetric loss such that the power passed by each arm is a fraction, s, of the input and an asymmetric loss such the power passed by the arm with the interaction region is reduced by an additional factor a. If the input to the whole device is P_0 then

$$P_1 = \frac{sP_0}{2} \tag{3.22}$$

$$P_2 = \frac{asP_0}{2} \tag{3.23}$$

When the two arms are in phase:

$$P_3 = 2P_2 + \frac{1}{2}(P_1 - P_2) \tag{3.24}$$

$$P_3 = saP_0 + \frac{sP_0}{4}(1 - a) \tag{3.25}$$

the transmittivity is then

$$T_{max} = \frac{s(3a + 1)}{4} \tag{3.26}$$

When the two arms are out of phase:

$$P_3 = \frac{1}{2}(P_1 - P_2) \tag{3.27}$$

giving the transmittivity as

$$T_{min} = \frac{s(1 - a)}{4} \tag{3.28}$$

From equations 3.26 and 3.28 we can express a and s in terms of the maximum and minimum transmittivity of the interferometer.

$$s = T_{max} + 3T_{min} \tag{3.29}$$

$$a = 1 - \frac{4T_{min}}{s} \tag{3.30}$$

Equations 3.29 and 3.30 can be used to locate the sources of loss in experimental Mach-Zehnder interferometers. In the case of experimental devices it will not be possible to account for all the symmetrical losses but those due solely to the interferometer can be identified, e.g. y-junction losses. This theoretical approach makes the approximation that losses do not vary with the relative phase of the signals in the two arms.

3.8 Summary

The model presented here, based on the matrix approach of Ghatak et al. [63], is capable of finding the modes of a multilayer planar waveguide with any of the layers possessing complex refractive index. The model has been validated by comparison with published data.

The model has been used to reproduce results by Stewart and Culshaw [11] which predict sensitivity enhancements of greater than an order of magnitude in absorption based planar waveguide sensors by addition of high index overlays. It has also been shown that similar sensitivity enhancements are possible for devices which detect changes in refractive index. It is predicted that higher sensitivity will be possible for TE operation than TM, as indicated by figure(3.11). The model supports the findings in [11]. The loss at transitions between waveguides with and without high index overlays has been modelled and has been found to be significantly less than the enhancement of evanescent power due to the films. As an example, a 30nm film of index 2.1 increases evanescent power of the fundamental TE mode by a factor of 20 but causes a loss of only 1.6-1.7 dB. Therefore, despite the loss due to the transitions it is expected that the power carried in the evanescent fields of a waveguide can be increased by more than an order of magnitude by the addition of a thin high index film.

A theoretical treatment of the losses in a Mach-Zehnder interferometer is given. This allows the calculation of the symmetric and asymmetric losses of a Mach-Zehnder interferometer if the maximum and minimum transmittivity of the device are known. This relies on the loss being constant as the relative phase of the signals in the two arms varies and will allow determination of the losses due to a high index

layer on one arm of an experimental Mach-Zehnder interferometer device.

Chapter 4

Experimental verification of the numerical model

4.1 Introduction

Having predicted large enhancements in the sensitivity of integrated optical sensors by the addition of thin high index films, it was necessary to construct an experiment with which to demonstrate this effect. Since it was expected that the sensitivity enhancements would be partially counterbalanced by higher losses, it was desirable to design an experiment where the loss and the fundamental sensitivity of a device could be separated. A Mach-Zehnder interferometer as described earlier was deemed to be suitable for this purpose. By using these devices to measure relatively large refractive index changes, compared with that which would be seen eg. in a biosensor, the effect of a high index film on the sensitivity to refractive index would be clearly seen despite the high losses expected for the thicker films.

To aid in removing noise due to variations in the amount of light coupled into the waveguide, the Mach-Zehnder interferometers were incorporated on one arm of a y-junction. The other arm of the y-junction was then used as a reference. The ratio of the two signals is the transmittivity of the Mach-Zehnder assuming the power split is symmetrical and the waveguide losses in both the interferometer and the reference are the same.

Figure(4.1) is a representation of the devices tested. The channel waveguides were made by potassium-sodium ion-exchange in soda-lime glass. These devices were then coated with different thicknesses of high refractive index film in a sensing region over one arm of each device. A reference device without a patch of high index material was also fabricated. Each device was then coated with an isolation layer of Teflon FEP and a window opened over the sensing region. This restricts the interaction of the guided light with the sample to the region in the window. The

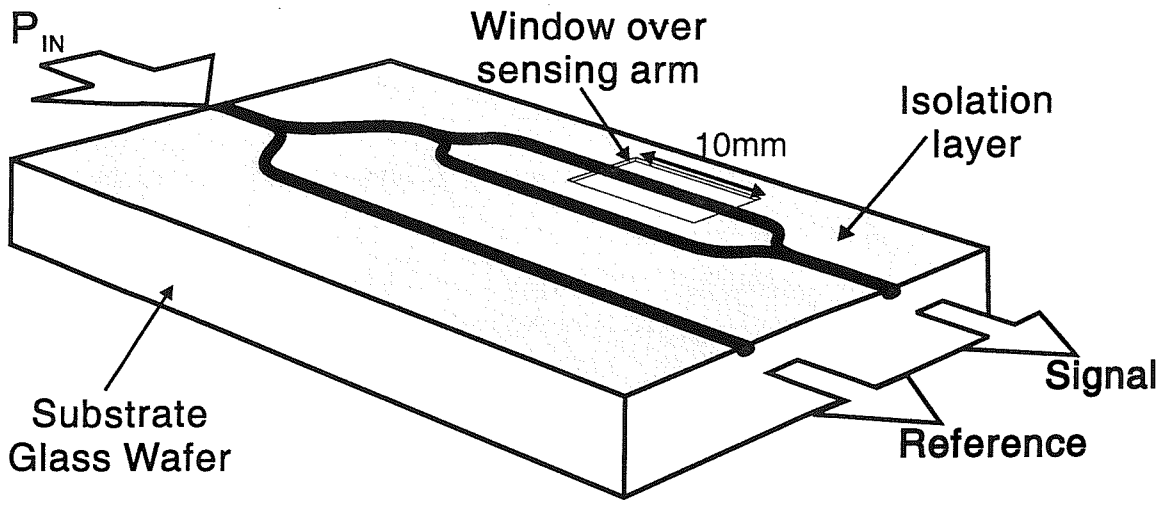

Figure 4.1: Mach-Zehnder interferometer

length of this region will be refered to as the interaction length and is 10mm for the device shown in the diagram.

The responses of these devices to different refractive indices were tested by flowing different concentrations of sucrose solution over the devices. The induced phase changes in the interaction regions were then deduced from the changing output signals from the interferometers.

From these results it was possible to calculate an approximate phase response of each device to refractive index and by comparing these phase responses the factor of sensitivity enhancement was calculated for each film thickness.

These devices also allowed estimates to be made of the loss induced by the high index films and of the practical detection limit for the system.

4.2 Fabrication and characterisation of waveguide devices

4.2.1 Fabrication of ion-exchanged channel waveguides

The channel waveguides were fabricated by potassium-sodium ion-exchange into soda-lime glass. The channels were defined by coating the surface of the glass substrate with aluminium and opening 3μm wide channels in that aluminium mask by a standard photolithographic technique. The ion-exchange was then performed

by suspending the sample in a potassium nitrate melt at 400°C for 25 minutes. Thermal diffusion allows potassium ions from the melt to be exchanged with sodium ions in the glass. The end faces of the chips were then lapped and polished to allow end-fire input coupling, reducing the size of the chip from an initial 50mm square to 40-45mm in length.

The masks used for photolithography have a variety of devices on them, including straight waveguides, y-junctions and Mach-Zehnder interferometers. The extra devices are useful for checking the fabrication has been performed correctly.

The time for which to perform ion-exchange for was deduced by making a series of samples with different times and measuring the range of wavelengths over which the waveguides support a single mode. The soda-lime glass substrates were found to be prone to breaking if they were not cooled very slowly. Unfortunately, to cause the diffusion to stop quickly it is necessary to cool the sample quickly. This is true to the extent that the distance that the sample was withdrawn above the melt after the ion-exchange was found to have an effect on the waveguides produced. The shorter the ion-exchange time, the more marked the effect of different cooling rates on the waveguides produced. It was therefore necessary to try to balance the fact that a short exchange time was required, but that the waveguides needed to be as consistent as possible between samples. In the next section the measurement technique used in finding the range of suitable ion-exchange times is described.

4.2.2 Spectral attenuation measurements

Spectral attenuation measurements are a very useful way of determining the cut-offs of guided modes in waveguides. The apparatus used for performing these measurements is shown in figure (4.2). The waveguide to be investigated is excited with a white light source via an optical fibre. The transmission spectrum is acquired by a computer which scans a monochromator through the wavelength range of interest and measures the signal at each wavelength. By comparing the transmission spectrum of the optical fibre with that of the combination of the fibre and the waveguide, the spectral attenuation of the waveguide can be calculated. These measurements are also offset by the coupling loss as light passes from the fibre to the waveguide. This loss is only very weakly dependent on wavelength for the setup described and

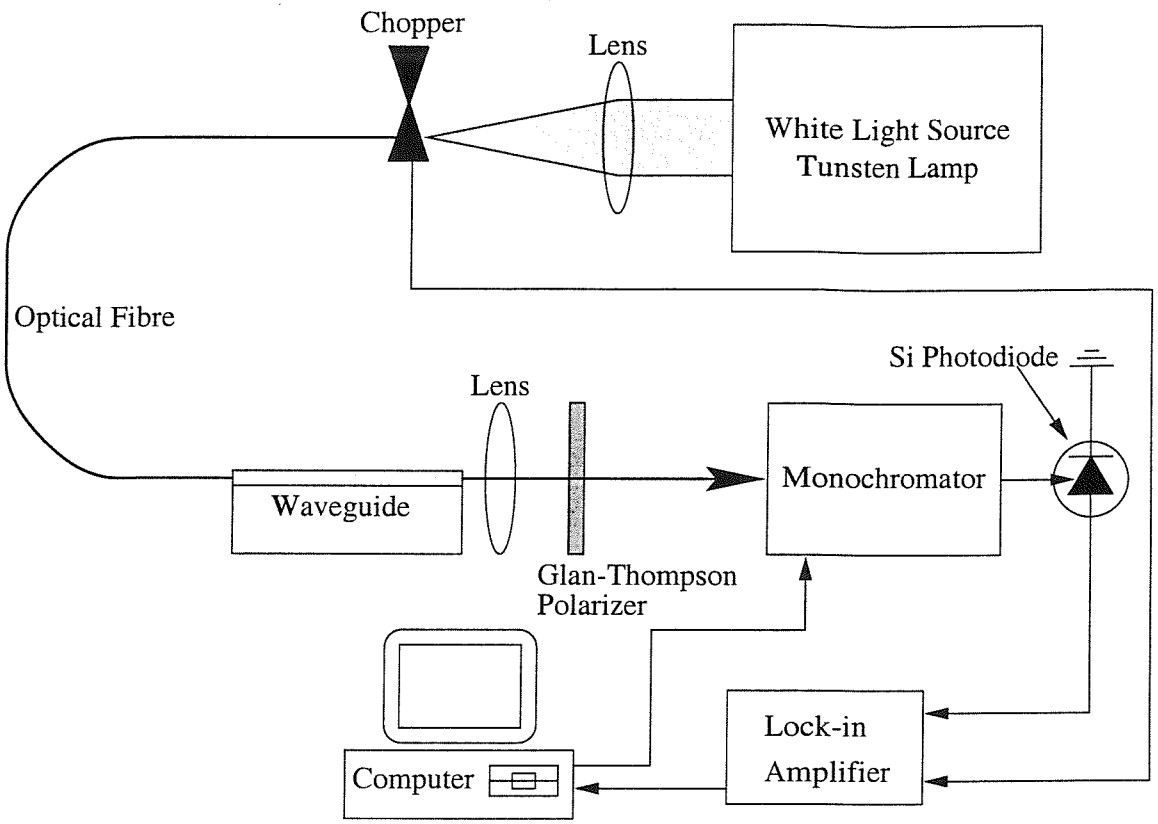

Figure 4.2: Spectral attenuation apparatus

is normally assumed to be a constant component. Due to the great sensitivity of the coupling efficiency to the relative position of the IO chip and the fibre it is envisaged that some errors will be incurred if the system is not mechanically stable.

In order to determine the range of wavelengths for which the waveguides support only one guided mode, spectral attenuation measurements were carried out on Y-junction devices. In the double-moded wavelength region, beating of the modes in the input waveguide and splitting region causes the amount of light coupled into each arm to vary with wavelength. The variation is expected to be sinusoidal with the difference in propagation constant of the two modes and the outputs of the two arms vary π radians out of phase with each other The onset of single moded opperation with increasing wavelength can be determined from the point at which these variations cease. Cut-off of the fundamental mode is deduced, as for single channels, by a rapid rise in attenuation with wavelength. An example trace is shown in figure(4.3). There is an offset of approximately 5dB due to fibre input coupling losses and the region of single-moded operation was from approximately 570nm to 770nm wavelength. The waveguides measured for this figure were fabricated using

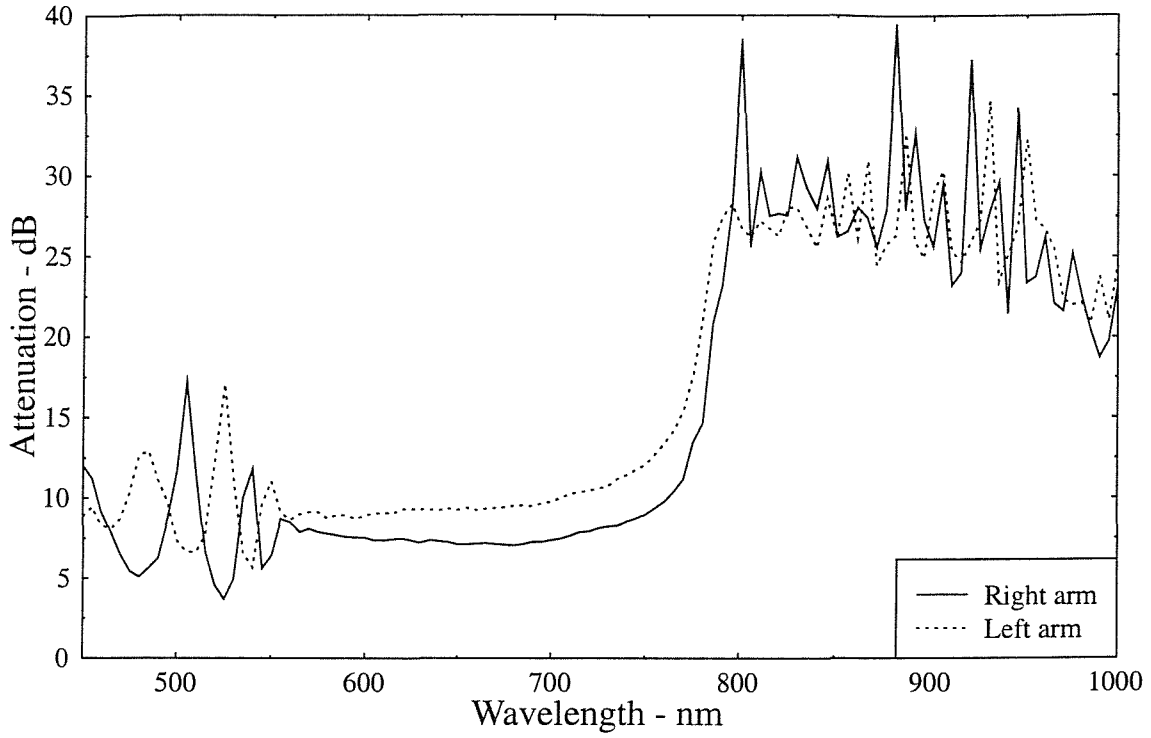

Figure 4.3: A spectral attenuation plot for an ion-exchanged y-junction

a 25 minute ion-exchange, which can be seen from this to be suitable for chips that are intended for use with light sources at and around 633nm wavelength.

Notably, this was performed with air as the superstrate. The superstrate refractive index has a small but significant effect on the position of the waveguide cut-offs. For example the addition of the Teflon FEP isolation layer (refractive index 1.3) shifts the fundamental mode cut-off to a wavelength 30-40nm longer.

4.2.3 Thin film deposition and patterning

To take full advantage of the predicted sensitivity enhancements from thin high index films it is necessary to find the optimum material to coat with. Problems were foreseen from transition losses at the ends of the coated region and scattering and absorption losses within the region. The transition losses remain an issue for future work. Absorption losses can generally be reduced by producing a high purity film. Since the materials which give high refractive indices tend to be refractory metal oxides, the oxidation state of the deposited material is important for controlling absorption and refractive index.

For thin high-index waveguides materials such as titania, tantalum pentoxide and silicon nitride are commonly used. The cleanrooms at the ORC had the materials and the equipment to attempt depositing titania and tantalum pentoxide. For this reason these materials were the ones initially investigated.

Amorphous titania is expected to have a refractive index in the range 2.1 to 2.75, the upper limit being the refractive index of the bulk crystal. Others [71] have found, for example, that oxidation of a titanium film can produce a dense high index film. It has also been reported that reactive magnetron sputtering of titanium in an oxygen/argon atmosphere provides a means of producing films of controlled refractive index and oxidation state.

Films produced at the ORC by thermally evaporating titanium sesqui-oxide in an oxygen atmosphere had a refractive index of approximately 2.1 [72]. These films had a slight blue colouration which may indicate incomplete oxidation. Attempts have also been made to oxidize titanium films in air. This is a very slow process at ambient temperatures and so had to be speeded up in a furnace. The films produced in this way were also visibly discoloured and the temperatures needed to oxidize the films in less than a day were high enough that ion-exchanged waveguides would diffuse further and change their guidance properties.

Deposition of tantalum pentoxide by reactive rf sputtering from a tantalum target in an oxygen-argon atmosphere yielded better results. In this process the sample is suspended a few centimeters above a tantalum sputtering target. The sample holder is grounded. An rf power supply is used to strike a plasma above the target. Collisions of ions in the plasma with the target remove tantalum which is oxidized by the partial oxygen atmosphere and deposited on the sample. This is a relatively slow process, but produces dense uniform films. The plasma may also help to remove adsorbed molecules from the sample surface. Adhesion of the films is good; they are unaffected by the tape test. Films of 100-200nm thickness were made on separate samples and were measured by ellipsometry to have a refractive index of 2.1. These films were not visibly absorbing to the naked eye.

It was found that thin films could be patterned by lift-off and so this process was adopted. Lift-off is performed by patterning a film of photoresist on the surface of the slide. When the deposition is performed the film only adheres to the slide in

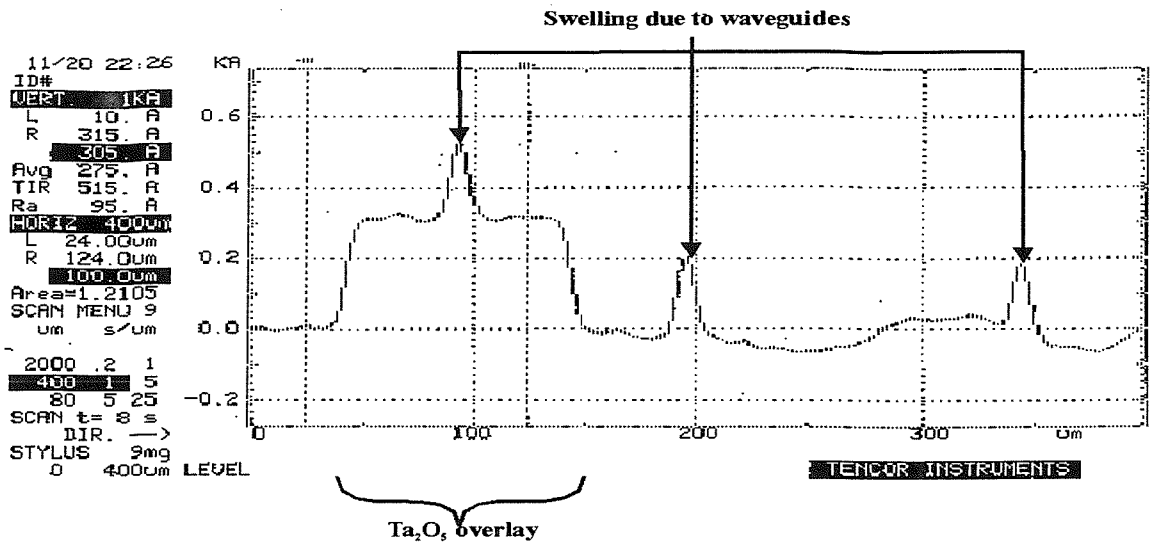

Figure 4.4: Alpha-step scan across a Mach-Zehnder interferometer device with a thin film of tantalum pentoxide

places where there is no resist. When the resist is removed by soaking in solvent the rest of the film is lifted off.

Figure(4.4) shows a surface profile across a Mach-Zehnder interferometer with a thin film of tantalum pentoxide deposited in a patch over one arm. With reference to figure(4.1), looking from input end of the waveguide to output this scan would go from the window over the sensing arm on the left to the reference waveguide on the observer's right. The profile was taken on a chip which had the ion-exchanged waveguides and a 30nm Ta_2O_5 film in the window region, but did not have the isolation layer deposited. On the scan the position of the waveguides can be clearly seen from the swelling caused during their formation by ion-exchange. The wider raised region (100μm wide) is the film of Ta_2O_5.

4.2.4 Spectral Response of Mach-Zehnder interferometers

It is interesting to compare figure(4.3) with a similar plot for a Mach-Zehnder interferometer which has had a patch of high index material applied. Such a plot is shown in figure(4.5) for a device with approximately 30nm of tantalum pentoxide on the surface. The patch of high index material causes the optical path length of that side of the Mach-Zehnder interferometer to be greater than that of the other side. The phase shift this produces is different for different wavelengths of light,

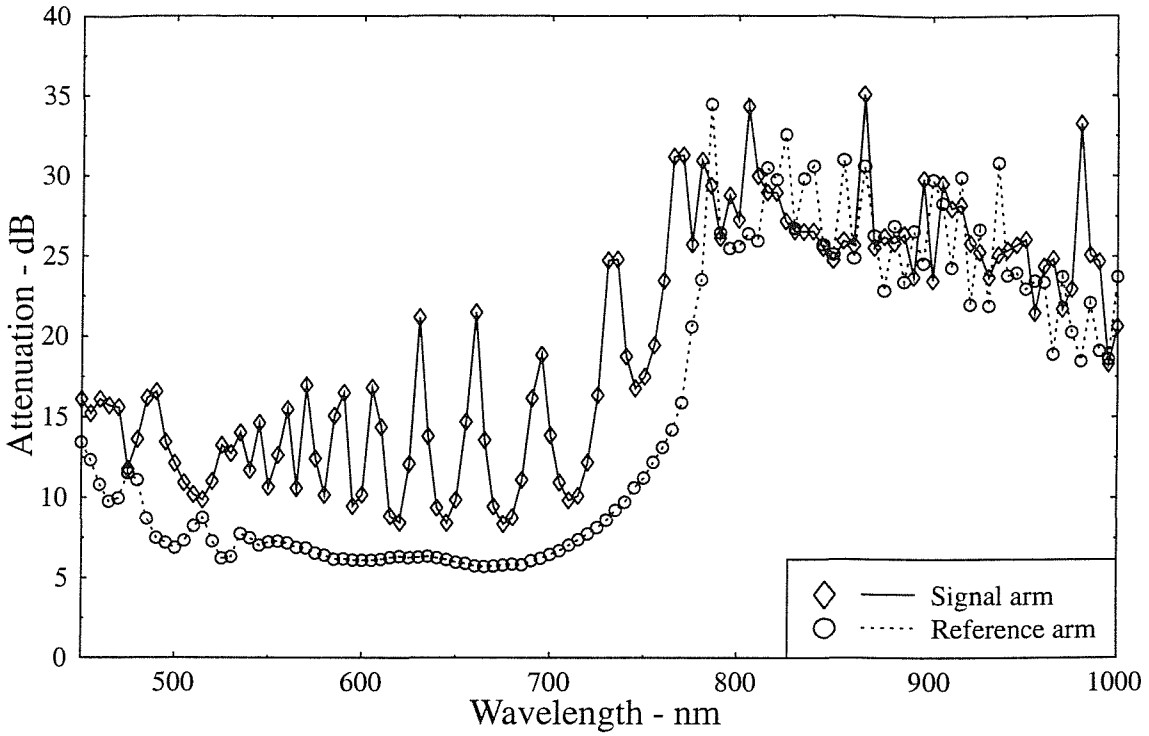

Figure 4.5: Spectral attenuation of a device incorporating a Mach-Zehnder interferometer with a reference arm

so on recombination the phase of the interference changes. This causes the fringes which can be seen superimposed on the trace in figure(4.5). The reference arm gives a useful comparison so that the effect of the interferometer can be seen. The peaks appear very sharp due to the comparative frequency of the oscillations and the sampling frequency; the data points have been marked to help show this.

4.2.5 Isolation layers

The fluoropolymer Teflon FEP was thermally evaporated in a high vacuum and then patterned by lift-off yielding a transparent film of refractive index 1.3. Films of approximately half a micron thickness were used. This should be sufficient to isolate the evanescent fields, as can be seen by reference to figure(3.9). A window was opened in the isolation layer to allow interaction of the waveguide with the analyte over part of its length. For the devices used here an interaction length of 10mm was used, although the same set of photolithographic masks includes devices with a range of other interaction lengths.

This material was chosen for use because of its low refractive index and the simplicity of the deposition and patterning. The deposition process does not heat the sample excessively, which could adversely affect the waveguides if they became hot enough for the ions to start re-diffusing in the glass.

Teflon FEP proved an adequate choice of material for these initial experiments where proof of the concept was the primary concern. There have, however, been some problems with this material; mostly because of its lack of durability. Teflon FEP is very soft and is even damaged by many of the cleaning techniques normally used. It is also attacked by some solvents which may in the future cause problems for the application of surface chemistry. It has also been found that Teflon films are slightly porous.

Without any kind of isolation layer the device without a high index film would have no response to refractive index — both arms of the interferometer would have the same change in optical path length. Clearly this is not true for the devices with a high index overlay, as was demonstrated by the spectral attenuation measurement of figure(4.5). For these devices the important advantage is that with no isolation layer the flow cell would be in direct contact with the surface of the waveguides. This would cause extra losses. It is proposed that in the future a different material would be used as an isolation layer instead of Teflon FEP.

4.3 Refractometry of aqueous sucrose solutions

The experimental setup is shown in figure(4.6). The waveguides were excited with a chopped, polarized, helium neon laser. Input and output coupling were achieved using lenses. The outputs were focused onto silicon photodiodes which were connected via lock-in amplifiers to a computer for data acquisition.

A flow cell was attached to the surface of the sample and a Flow Injection Analyzer (FIA) used to pump a continuous flow of de-ionized water over the sample. The system was pressurized with argon to approximately 0.5 bar above ambient pressure to help reduce the risk of air bubbles entering the system. Samples of sucrose solution were then introduced into the flow to produce a change in refractive index. The maximum refractive indices of the samples of sucrose solution were

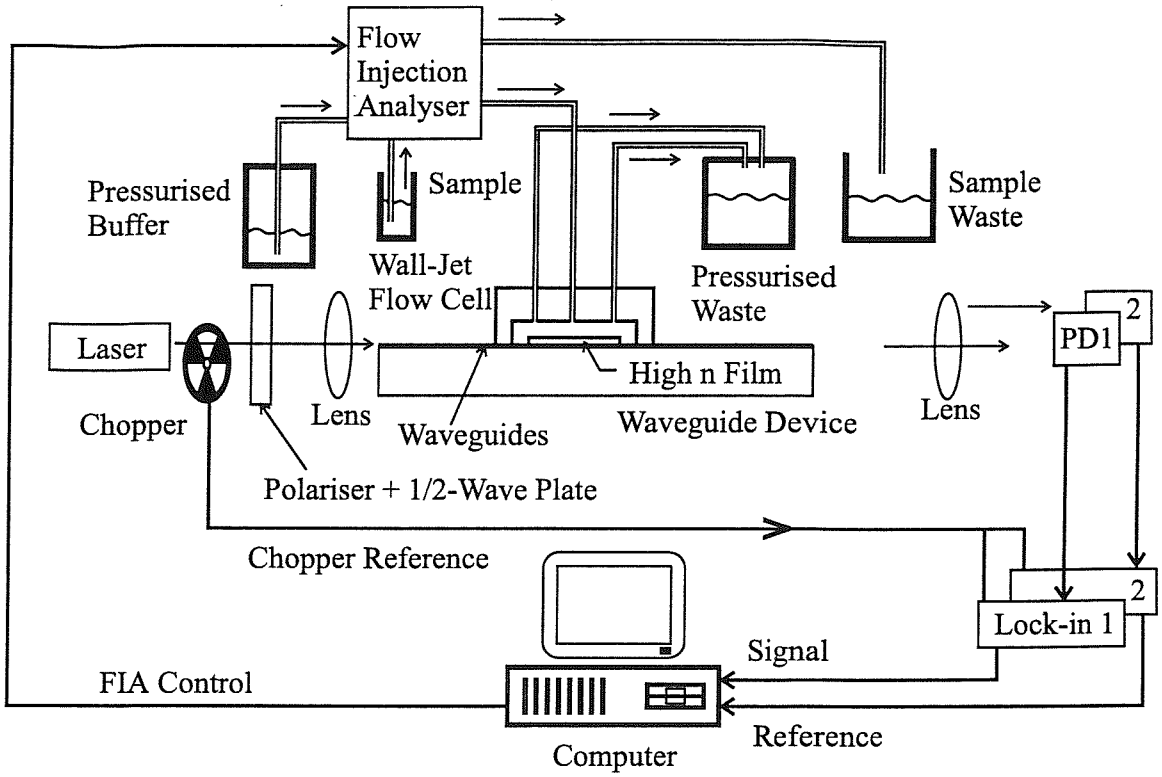

Figure 4.6: Apparatus for flow injection analysis

measured at sodium wavelength using an Abbe refractometer. From the ratio of the outputs of the device, the response to the different refractive index in the pulse of sucrose solution was measured.

4.4 Results and Analysis

4.4.1 Response to a pulse of sucrose solution

Figure(4.7) shows the effect on the ratio of the outputs of a device to a pulse of sucrose solution. The approximate variation of refractive index with time has been sketched on the figure also.

The oscillations in the signal correspond to the diffused regions at the beginning and end of the sugar pulse. It was convenient in this experiment that the trailing edge of each sugar pulse was diffused more than the leading edge as for the larger responses this allowed easier counting of the number of oscillations that the system went through. In a practical biosensor system the refractive index changes would be so small that this would be a disadvantage. The output would not pass through

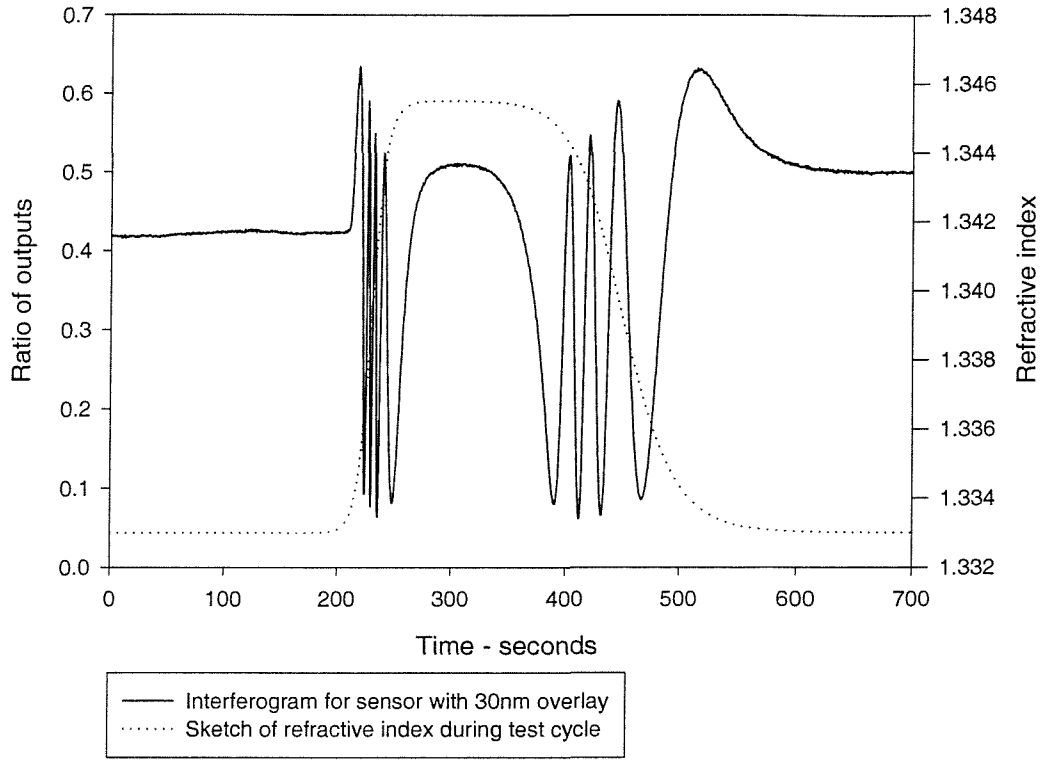

Figure 4.7: Response of a Mach-Zehnder interferometer to a pulse of sucrose solution

Thickness of overlay (nm)	Gradient -method 1	Enhancement factor	Gradient -method 2	Enhancement factor
0	174	1	151	1
20	504	2.9	528	3.5
30	2345	13.5	2287	15.1
40	8085	46.5	8294	54.9

Table 4.1: Experimentally determined enhancement factors for TE modes

multiple maxima and minima and an extended wash-out would cause any drift of the signal with time to have a larger detrimental effect on the uncertainty in measurements. This can be easily solved by increasing the pump speed while the diffused parts of the sample are passing through the flow cell.

The phase shift induced by the sucrose solution was directly read from the graphs by comparison with a sine wave with the same maximum and minimum values. Over a series of measurements the maximum and minimum signal for a given device was found. The output of the interferometer is expected to vary approximately sinusoidally with refractive index (assuming optical path length of the waveguide is linear with superstrate refractive index).

There is a potential source of error here, due to the fact that the maxima and minima in the output of the MZI do not occur at constant levels but rather there is some kind of an envelope around the curve. The cause of this is not known with any certainty, but the importance of this can be reduced by inducing large numbers of oscillations in the output with large refractive index changes.

The results are shown for the TE polarization in figure(4.8). Straight lines have been fitted to the data using least squares. Arguably the lines should be forced to pass through the origin because the response for zero change in refractive index is a zero phase shift. In table(4.1) these results (method 1) and those without forcing the lines to pass through the origin (method 2) are presented. The estimated error bars for the points were smaller than the markers for the points and so have not been included except for on the line for the 40nm thick film which had the largest estimated error. These errors were estimated by examining the accuracy of estimation of the phase shift induced by a refractive index variation using the very

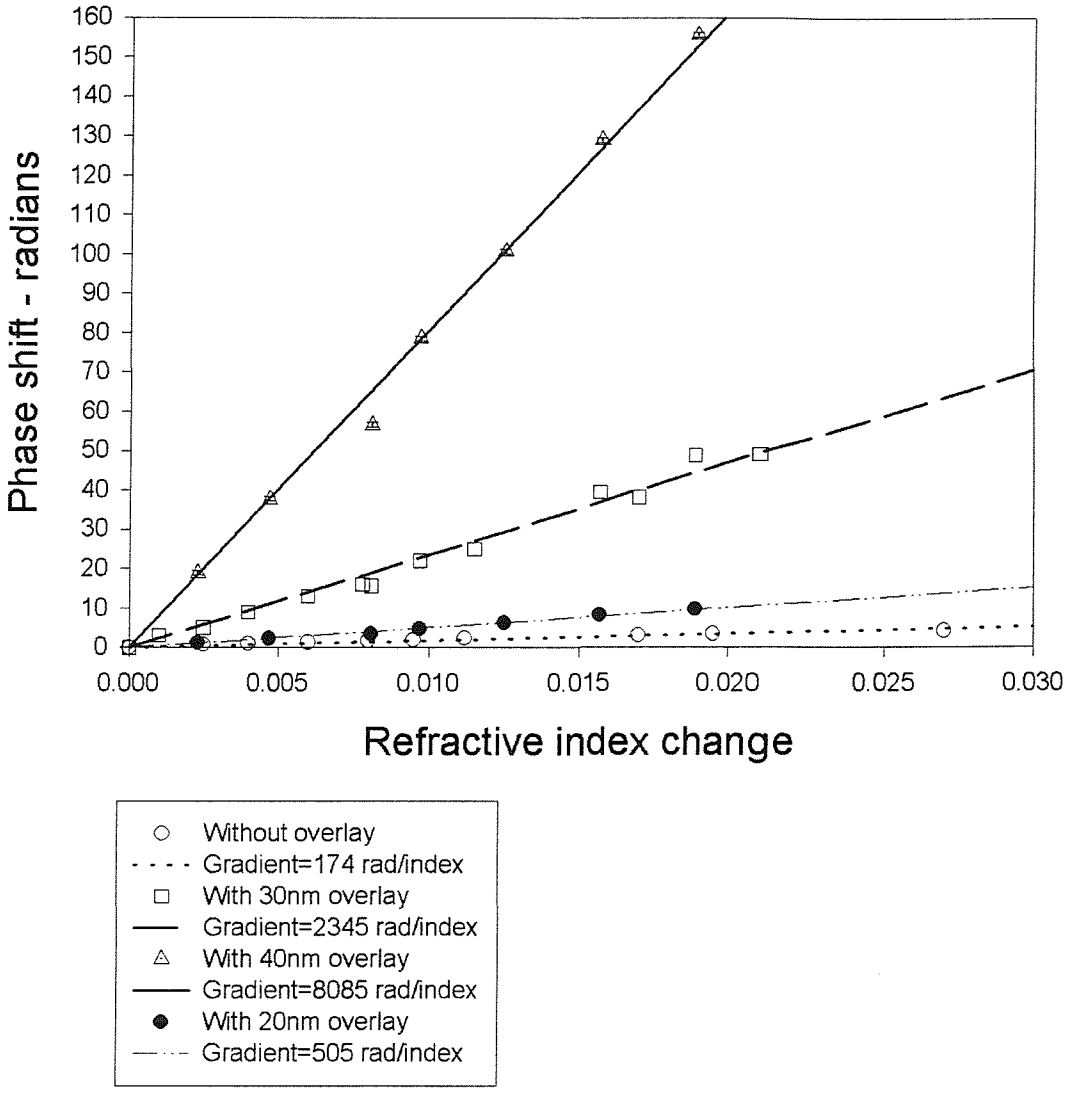

Figure 4.8: Phase response of interferometers to different refractive index perturbations — TE operation

simple method employed.

There were two main sources of the errors estimated in this way. When there is a constant flow of de-ionized water passing through the flow-cell the signal should remain constant. This is referred to as the baseline. After a pulse of sucrose solution has passed through the system, the output should return to the same baseline. The baseline was seen to be different before and after some, but not all, measurements. On performing repeat measurements with identical sucrose samples this effect was not found to be consistently reproducible. The cause of this has yet to be identified.

The other effect that caused significant uncertainty in the measurement was the changing value of the ratio of the outputs at the maxima and minima. It is believed that this is due to the polarizer being incorrectly mounted which will have led to both the TE and TM modes being excited, or due to depolarisation within the structure. Depolarisation may be occuring due to scattering, or to coupling effects with regions such as bends and the region of the y-junctions where the splitting occurs. In these areas transitions in waveguide geometry are occuring and hence the guided modes are changing, conditions under which not all the light will couple into the desired mode.

The output powers for these orthogonal modes would simply add giving shifts similar to those seen. For example, figure (4.7) is an example trace for a device with a 30nm thick Ta_2O_5 overlay. The difference between the TE and TM sensitivites for this device (comparing figure(4.8) and figure(4.10)) is a factor of approximately 7. If the output were a combination of TE and TM, the two would simply add in intensity (orthogonal modes do not, in general, interfere) giving a trace much the same as that shown. However, while this explanation is plausible, these experiments were not sufficient for proof.

The gradients of the fitted lines have been included in the key. From this it can be seen that, in terms of the phase change induced for a perturbation of refractive index, the sensitivity of the devices has been increased by up to approximately 50 times. The sensitivity enhancements indicated by the gradients have been plotted alongside theoretical curves in figure(4.9). To give an indication of the uncertainty in the gradients calculated, the data for both methods of fitting are plotted. The horizontal error bars show the uncertainty which exists in the measurement of film

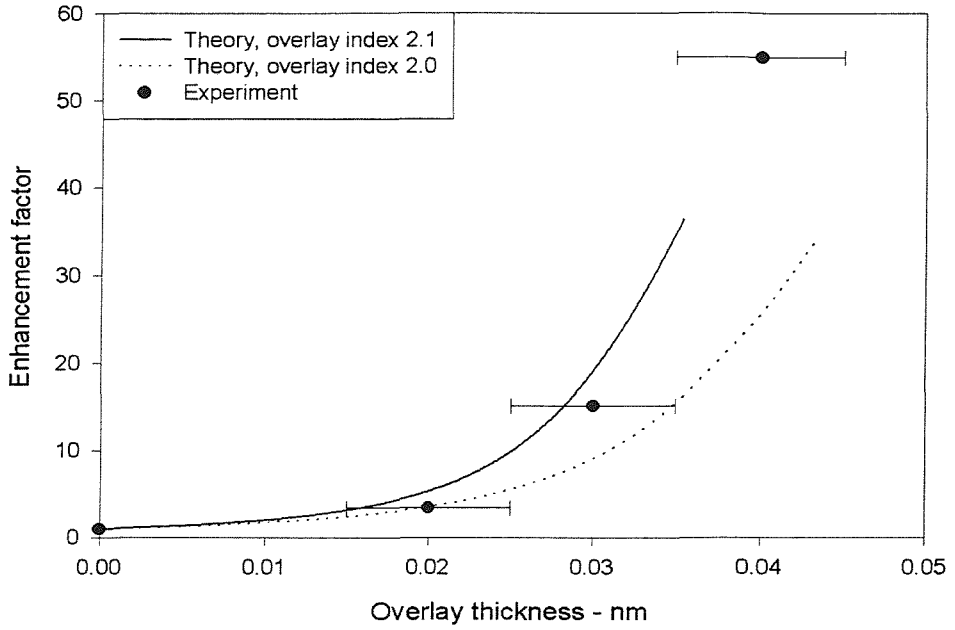

Figure 4.9: Comparison of theory and experiment — TE operation

thicknesses due to the surface roughness of the samples. This shows two things of interest. The first and most significant is that the theory fits the experiment very well. The second is that the theory would predict that for the sample with the 40nm overlay the mode is being guided in the overlay film. The theoretical curves were truncated when they reached this point and the measured point lies well beyond. This sample was observed to have much higher losses than the others for TE operation. The losses are examined in more detail later.

The results for the TE polarization are well fit by straight lines. The exact method used for fitting the lines has a small effect on the results, but not drastic. The same is not true of all the results for the TM polarization. These results are from a single series of experiments and so it is proposed that the experiments should be repeated before any conclusions are drawn.

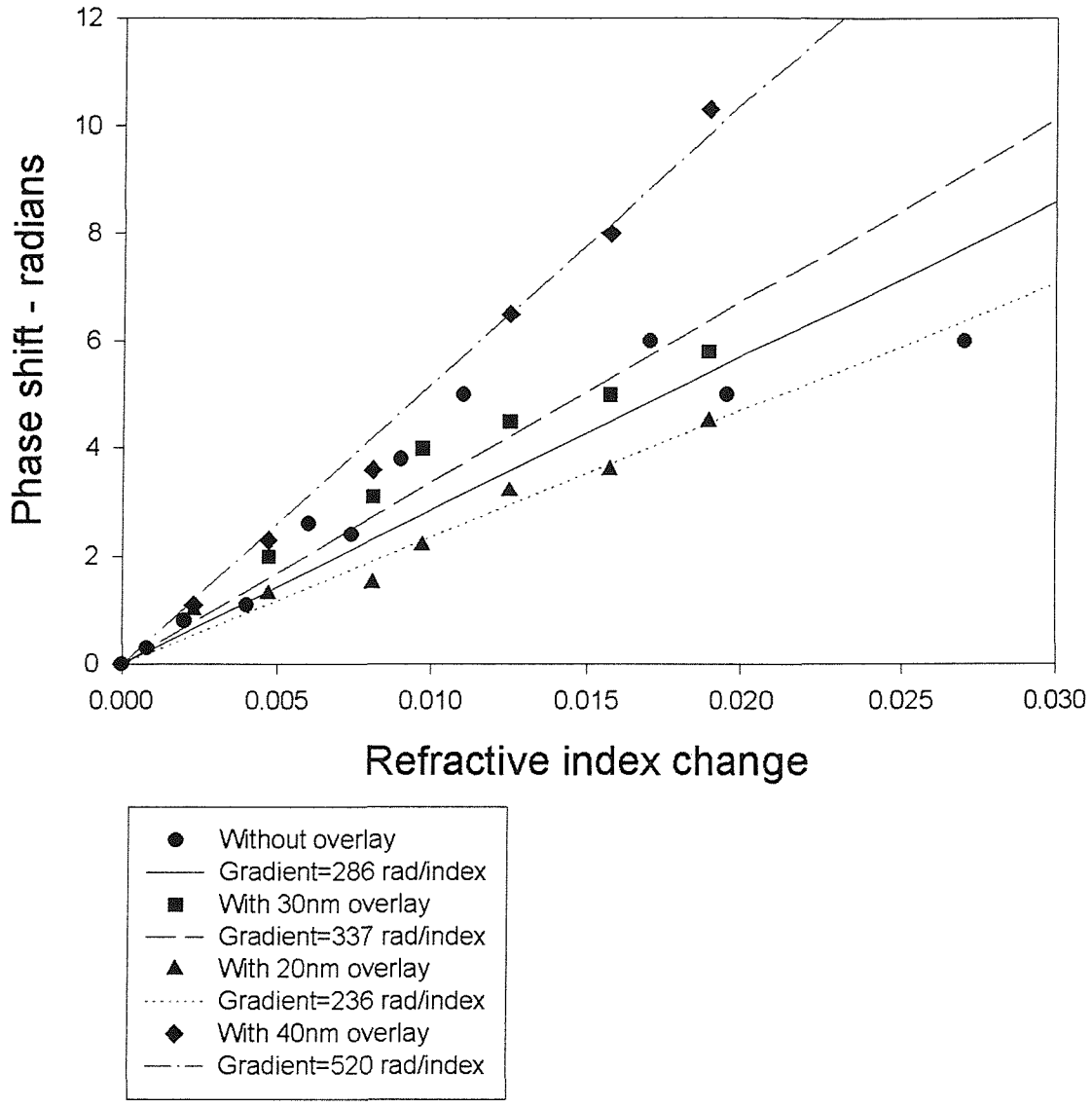

Figure 4.10: Phase response of interferometers to different refractive index perturbations — TM operation

4.4.2 Estimation of the detection limit

Various factors affect the limit of detection of the system. The first major factor is the noise in the signal. This is minimized by use of the reference arm on the device and by use of lock-in amplifiers, but it is inevitable that there will always be some noise. The fundamental noise sources that will not be escaped are shot noise and thermal noise in the detectors. Other forms of noise in this experiment will be optical noise and noise due to vibrations (effecting the coupling of light into the waveguides). The effect of optical and vibrational noise should largely have been eliminated by the referencing as they effect the intensity of light passing through the whole device. It should also be noted that, as the refractive index of water changes with temperature, temperature variations during the experiment will have caused a form of noise, although this should be slowly varying due to the thermal mass of the apparatus. A more complete discussion of noise in this system can be found in [73] where the same apparatus was used to characterise waveguide SPR sensors.

Noise limits the minimum variation in output level that can be attributed to a reasonable degree of certainty to be due to a change in signal.

To estimate the detection limit the noise on the signal was analyzed. For one of the baseline regions between measurements, where only water was flowing through the flow-cell the mean was calculated and then the residuals plotted. This is shown in figure(4.11). The mean was 0.1095 and the 99% confidence interval was calculated as 7.37×10^{-3}. The ratio of these is 1485. From this the 99% confidence interval can be estimated for any part of the graph. This gives an estimate of the smallest detectable variation in the signal. By correlating this to a phase shift and using the gradient from figure(4.8, 4.10), the smallest detectable refractive index change can be estimated. This has been performed using the two methods of gradient fitting for the TE mode. For the TM excitation only the first method of fitting a gradient to the refractive index responses has been performed.

It is noteworthy that the ratio of signal to noise was of order 1×10^3 while, if the noise were purely shot noise, the ratio of signal to noise would be estimated as being of order 1×10^6. This is calculated using parameters from [73] with the approximate power levels in these experiments and is accurate to within one order of magnitude given the variations in optical power during the experiments. The

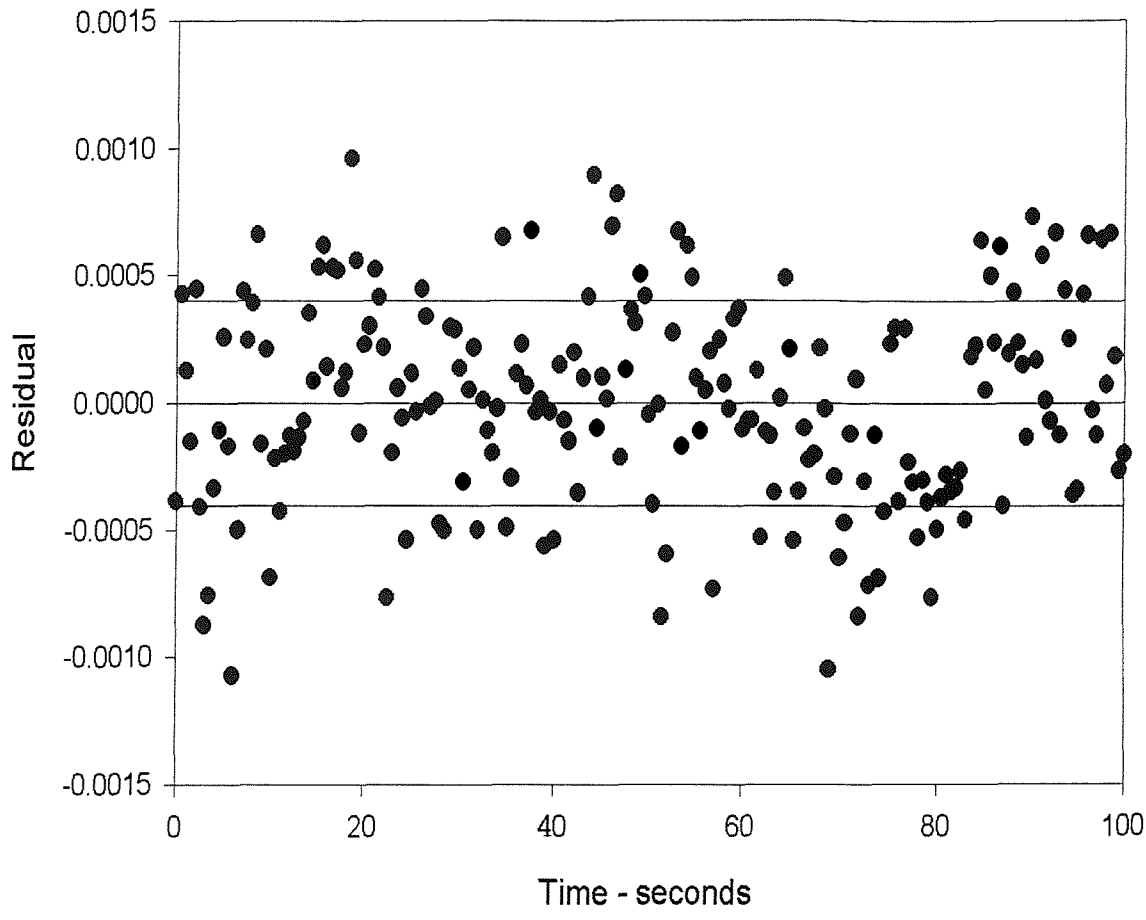

Figure 4.11: Residuals of baseline noise

system is therefore clearly operating well away from the shot noise regime. Since thermal noise for these detectors is estimated as an order of magnitude smaller than the shot noise, the major sources of noise are determined to be optical noise and noise due to the mechanical stability of the apparatus.

The phase shift caused by a variation in refractive index varies linearly with the size of that perturbation, but the variation in signal varies sinusoidally. When the signal is in the vicinity of a maximum or minimum the change in output level for a given phase change is small. For maximum sensitivity a device should be designed to operate away from these points in the region where the response for a given phase shift is greatest.

Overlay thickness (nm)	Polarization	Method 1	Method 2
0	TE	4.8×10^{-6}	5.6×10^{-6}
0	TM	3.4×10^{-6}	—
20	TE	1.75×10^{-6}	1.7×10^{-6}
20	TM	2.8×10^{-6}	—
30	TE	4.0×10^{-7}	4.1×10^{-7}
30	TM	2.2×10^{-6}	—
40	TE	1.8×10^{-6}	1.8×10^{-6}
40	TM	1.7×10^{-6}	—

Table 4.2: Detection limits of Mach-Zehnder interferometers (method 1 uses gradia of best-fit straight lines that are forced to pass through the origin)

4.4.3 Losses induced by high-index films

Using equations (3.29) and (3.30) it is possible to separate the symmetric and asymmetric components of the loss. Calculation of the ratio of the signal passed through the interferometer with that passed through the reference arm gives the transmittivity of the interferometer. Using the maxima and minima in transmittivity with equations (3.29) and (3.30) the symmetric and asymmetric transmittivities are found and hence the losses.

If the waveguide losses in the interferometer and the reference are the same the calculated symmetric loss would be the loss due to the y-junctions.

One problem for these calculations is that they are very sensitive to the exact values used for the maximum and minimum transmittivity. The changes in these values over the course of a measurement means that the estimates of the loss vary significantly.

The asymmetric loss in the interferometers, which is the loss due to the interaction region, is between 1 and 3 dB for all the measurements except the TE polarized measurements on the sample with a 40nm overlay. There the loss is very much higher, approximately 17dB from the 1 cm interaction region. This compares favorably with [14] where losses of 60-80dB/cm were reported for a waveguiding film of refractive index 1.7 overlaid on potassium-sodium ion exchanged waveguides. This very large loss was primarily due to absorption in their high index waveguides.

Overlay thickness (nm)	Polarization	Transmittivity	Loss (dB)
0	TE	0.7	1.5
0	TM	0.5	3.0
20	TE	0.6	2.2
20	TM	0.7	1.5
30	TE	0.6	2.2
30	TM	0.8	1.0
40	TE	0.02	17.0
40	TM	0.6	2.2

Table 4.3: Losses in Mach-Zehnder interferometers due to interaction regions

4.5 Mach-Zehnder interferometer with no isolation layer

The influence of the isolation layer upon the tendency of the devices not to return to the baseline value following a sucrose pulse was investigated by fabricating three devices with 20, 30 & 40nm thick Ta_2O_5 films over the interaction region but with no isolation layer. These samples were tested using the same procedure and the gradients and detection limits are given in table 4.4. One detail of the experiments that was necessarily changed was the method of sealing the flow cell to the chip. In the earlier experiments the seal was achieved by a black, nitrile rubber, o-ring. This caused unworkable losses to be induced and so an alterantive was devised. Gaskets were made from clear silicone rubber and used to seal the flow cell to the chip. This reduced the losses to the level seen with a teflon isolation layer and the nitrile rubber o-rings, but increased the overall volume of the flow cell. Flow cell volume is not a problem for experiments using bulk fluid samples, but where the transducer is being used to measure chemical binding to a surface the volume of the flow cell determines the time for chemicals to diffuse to the surface and hence the rate of binding. In this way large flow cell volumes can drastically reduce the practicality of immunosensors.

Results were not obtained for the 30nm and 40nm Ta_2O_5 films in the TE polarisation due to high losses. However, in the other cases, the removal of the isolation

Table 4.4: Sensitivities and detection limits for MZI's without isolation layers

Overlay	Sensitivity (rad)		Detection limit	
Thickness (nm)	TE	TM	TE	TM
20	326	175	8.1×10^{-6}	1.1×10^{-5}
30	—	286	—	2.3×10^{-5}
40	—	687	—	3.7×10^{-6}

layer was observed to eliminate the baseline drift over the course of a test cycle, the baseline always returning to within 2×10^{-5} refractive index of its pre-sample value,equivalent to a 0.2°C temperature change. It is believed that the larger baseline drift exhibited in the first four samples was due to porosity of the isolation layer leading to interaction of the analyte with modal evanescent fields outside the interaction region. A 20-30nm Ta_2O_5 coated device without isolation layer is shown to be more sensitive than an uncoated device with isolation layer, and demonstrates improved stability. The addition of a high-index film is thus an alternative to use of an isolation layer.

4.6 Summary

The initial experiments show that increases in the sensitivity of integrated optical sensors of greater than an order of magnitude can be achieved using thin high index films when using TE polarised excitation. The enhancements agree well with those predicted by the numerical model.

The data for TM excitation were not so well fit by straight lines. This was especially significant for the data for the device with no high index film which made it impossible to calculate enhancement factors for the devices. Whilst these measurements do not yield detailed quantitative comparisons of the devices with different film thicknesses, the measurements are sufficient to clearly demonstrate the lower sensitivity of the overlaid devices in TM operation than in TE.

The losses associated with the patches of high index film have been calculated. The sample with a 40nm thick film had much higher loss for the TE mode than the other samples. The TM mode is not affected in the same way. This is believed to

indicate that the film was thick enough that it became waveguiding and the lateral confinement of the TE_0 mode was lost. Since the high index film has to be thicker to start guiding the TM mode than the TE mode, the TM mode is still laterally confined.

These experiments have demonstrated the theoretical predictions to correspond to experimental results. The devices used have not undergone any design optimization and have already been shown to be as sensitive as optimized devices in the literature. However, the refractive index changes measured in these experiments were relatively large. Before measurements closer to the calculated detection limit can be made it will be necessary to rigorously identify the cause of some of the shifts in base line and the drifting values of the maxima and minima. To do this further experiments need to be devised which separate effects due to temperature, polarisation and diffusion of the analyte into isolation layers.

The isolation layer used in the first devices limited reproducibility through baseline drift believed to be due to porosity, and omission of the isolation layer was shown to reduce this drift. The experiments without isolation layers also demonstrated that use of high index films on Mach-Zehnder interferometers can be regarded as a viable alternative to isolation layers, although the transparent gaskets used to seal the flow cells to the chips cause an increase in flow cell volume that may be unacceptable in applications such as immunosensing.

This work has demonstrated that highly sensitive refractometers can be readily realised in cheap, simple, ion-exchange technology. The devices fabricated in this way will allow fibre coupling to be combined with sensitive detection. Work on improved mechanical and thermal stability of instruments incorporating such devices is expected to result in further improvements in detection limits. Development of these devices has been left to other workers in order to pursue the primary goal of this research – a multi-channel fluoroimmunosensor for pollutants in river water.

Chapter 5

Silica film deposition and annealing

5.1 Introduction

Isolation layers perform two tasks on the sensors described in this thesis. The first task is to limit the interaction of a sample with the sensor chip to well defined zones. The second task is to protect the waveguide from other influences at the surface of the chip. The most notable of these is the loss induced by the nitrile rubber o-rings used to seal the flow-cells to the chips if the o-rings are allowed to be in direct contact with the waveguides. Some work was presented in the previous chapter where a silicone rubber gasket was used to good effect to seal flow cells to chips without isolation layers without incurring excess loss. This was successful, but significantly increased the effective volume of the flow-cell, which makes this method undesirable for immunosensing where low volume is critical to keeping samples small and allowing sufficient diffusion within a sample as it passes through the flow-cell to maximise binding.

The experiments on Mach-Zehnder interferometers described in chapter 4 demonstrated a fundamental weakness in practical application that the fluoropolymer used as an isolation layer lacked the mechanical stability necessary for a reusable sensor chip. There were also problems in those experiments which were attributed to the porosity of the isolation layer.

An isolation material was needed which is non porous, low loss and rugged enough to survive flow cells being clamped to it. This material also needs to be patternable, so that the waveguides can be exposed where necessary, and the processing needs to be performed at a low enough temperature that the waveguides do not re-diffuse: the potassium ions in the glass become mobile and spread out in the glass at high temperature, causing the peak refractive index of the structure to drop and changing

the properties of the waveguides. For potassium ion-exchanged waveguides in soda-lime glass this means that in practice the temperature of the substrate should not exceed 300°C during further processing.

The deposition of silica by rf magnetron sputtering from a silica target was selected as an appropriate method. The deposition can be performed at room temperature yielding hard films with good surface adhesion. The films produced in this manner can also be patterned by a photolithographic lift-off process. The process was, however in need of optimization to produce films of acceptably low loss and porosity. For RIANA porosity of the isolation layer is not a great concern because if the interaction regions need to be controlled, it is possible to place the surface chemistry where it is needed using micro-drop technology. Also, the final system makes use of tagged antibody molecules which are large protein molecules and therefore need larger pore sizes if they are to penetrate an isolation layer than the dye molecules in their free state or the sucrose and sucrose molecules used during the interferometer experiments of chapter 4. The waveguide loss induced by the silica films was of great concern and the target figure was that the induced loss should be less than 1dB per cm. This figure was chosen by the RIANA project partners as one which gave an acceptable difference in power at the beginning and end of a sensor chip so that, for a series of sensing positions along the length of a 3 centimeter long waveguide, the power at the first and last position would be within a factor of 2.

The work on optimizing the deposition of silica films for use as isolation layers on integrated optical sensors was performed by a group of researchers involved in work for RIANA and other projects. The design and fabrication of the test devices is attributable jointly with members of this group.

It was decided to hold the thickness of film and rf power as constant as practical between samples whilst varying the gas constitution, substrate temperature and the duration of a post annealing step. The large number of combinations of parameters meant that the full data set had not been collected by the time of writing. A suitable set of deposition parameters has been found, as is shown by the results to date. It is anticipated that other members of the group will continue this work.

5.2 Format of the experiments

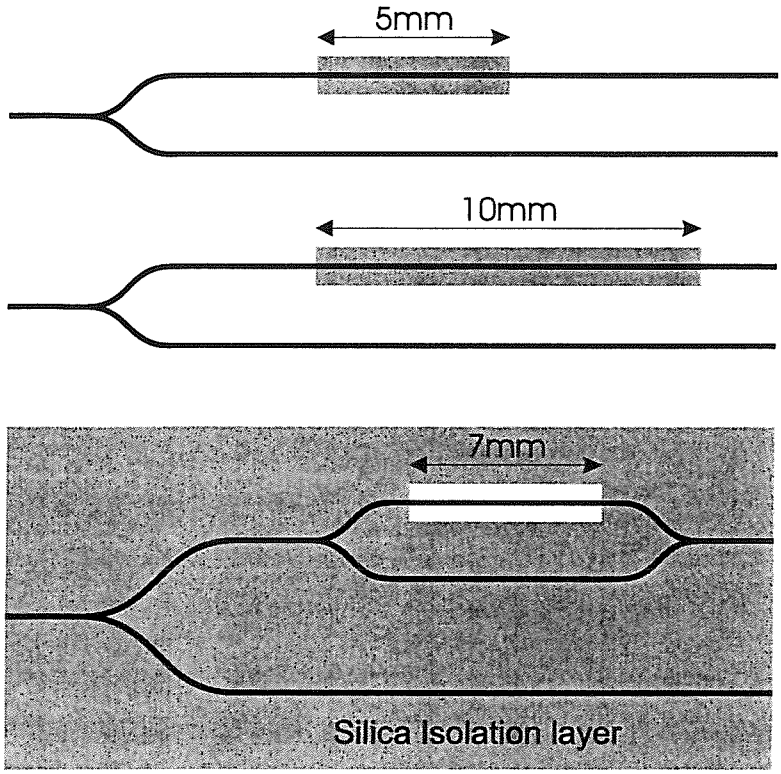

Figure 5.1: Schematic representation of integrated optical devices for evaluating the performance of silica isolation layers

Figure 5.1 shows schematically the devices that were fabricated to measure the loss and porosity of the sputtered silica film. To measure loss, y-junctions were made with a patch of silica on one arm. Each chip featured 10 y-junctions with a 10mm silica patch and 10 y-junctions with a 5mm patch. The y-junctions are designed to be symmetrical, so the ratio of the powers transmitted by the two arms of the device is the transmittivity of the silica patch relative to the uncoated waveguide. To investigate the porosity of the silica films, Mach-Zehnder interferometers were made. These had silica deposited over the entire surface except for a 7mm interaction region on one side of the interferometer. The intention was to perform refractometry experiments using these devices and to monitor for a drift in signal with time that would indicate penetration of the isolation layer by analyte solutions.

Waveguides were fabricated by potassium-sodium ion-exchange in soda-lime glass at 390–400°C for 20 minutes. The waveguides were defined by 3μm wide openings in aluminium masks 200-250nm thick, patterned by a standard photolithographic

process. The samples were then end-face polished, cleaned and checked for single moded operation at 594nm wavelength. The wavelength of operation and hence the fabrication conditions were selected to give results of broadest applicability to the projects for which the results were needed. 594nm is the wavelength of a helium-neon laser that was available at the time and is conveniently close to the sodium emission wavelength doublet, wavelengths that are historically used as standards in the field of refractometry.

To pattern the silica films, the surface of the samples was once again spin coated with resist and patterned by photolithography before the silica was deposited. Before the development stage of the photolithographic process, the resist coated substrate was soaked in chlorobenzene for 5 minutes. This creates a more durable layer of resist at the surface which is then undercut during developing. Once developed the substrate only has resist where the sputtered films are to be removed. The undercutting is intended to shadow a small part of the substrate from deposition so that there is a gap in the film through which acetone can penetrate to dissolve the photoresist and remove the unwanted material.

In preliminary experiments by other workers in the group, before the systematic study, the thickness and attenuation of silica films was not found to be consistent across deposition runs with nominally the same parameters. Due to the previous variability of results, modifications were made to the sputterer before commencing this series of experiments. Use of the sputterer for other materials was avoided over the time the samples were being produced to avoid contamination. The sputterer gas supply was changed to dedicated cylinders of high purity oxygen and argon, where previously the gas supply was shared with other labs. This reduces the risk of contamination. The sputterer was also fitted with mass flow controllers to better control the plasma composition during sputtering and modifications were made to allow control of the substrate temperature during sputtering.

The films were deposited in an oxygen/argon atmosphere which had a pressure of 11mTorr before the plasma was struck. Measurements have been performed on devices deposited with no oxygen, 10% oxygen in the plasma and one sample fabricated with 20% oxygen in the plasma. The samples were fabricated with three different substrate temperatures - not heated, heated to 130°C and heated to 200°C.

The samples had loss measurements performed before annealing in oxygen at 250°C for 1 hour, another hour then another two hours, i.e. measuring after cumulative annealing times of 0, 1, 2 and 4 hours.

The measurements on the samples were kept deliberately simple due to the large amount of data that was to be acquired. Light from a HeNe laser was coupled into the waveguides using a ×10 microscope objective lens. The beam was mechanically chopped and the synchronization signal fed to two lock-in amplifiers. The two outputs of each device were focussed with another microscope objective lens onto two photodiodes which were connected to the lock-in amplifiers. Initially the signal was read directly from the lock in amplifiers, but later a PC was used which displayed the two signals and their ratio.

Since the efficiency of coupling into the different waveguides can vary a great deal, it was decided to make use of the ratio of signals between the two arms of y-junctions. One arm of each acts as the reference which can be ratioed out to give the transmission independent of coupling efficiency. Because of imperfections in the waveguides, ten devices each with 5mm and 10mm long silica films were measured and the mean transmittivity was found. Loss in dB is calculated as -10 log (transmittivity). The number of devices allows random fluctuations in the ratio of the outputs to be averaged out and the two different lengths of patch allow losses due to the transitions at the ends to be factored out. This gives the loss caused by the 5mm difference in the length of the silica film. Despite the averaging across multiple devices, the errors are estimated to be at least 0.2dB/cm, from the standard deviation of the transmittivity for the lowest loss devices.

To investigate the porosity of the isolation layer, a simple experiment was devised whereby the two outputs of the interferometer devices would be measured while the surface of the sample went from being dry to being covered in water. It was expected that a non-porous film would yield a sharp change to a new output ratio and then hold constant. If the film was porous it was expected that the output ratio would drift with time as the water penetrated, changing the mean refractive index of the film and hence the optical pathlength of the waveguide beneath the film.

Thickness μm	% Oxygen	Deposition Temperature °C	TE loss (dB/cm ±0.2dB/cm)			
			No anneal	1 hour	2 hours	4 hours
0.62	0	ambient	2.95	1.18		
0.67	0	130	11.15	1.66	0.99	
0.56	0	200	4.09	2.49		
0.43	10	ambient	13.67	0.93	0.39	0.33
0.65	10	130	7.71	3.02		
0.49	10	200	7.00	0.06		
0.58	20	130	1.60			

Table 5.1: Waveguide loss induced by silica films deposited with different parameters and effect of annealing at 250°C :TE polarization

5.3 Results

Tables 5.1 and 5.2 show the results from the transmission of y-junctions. Losses have been converted to dB/cm for convenience and the tables give the total times the samples have been annealed for. As can be seen from these tables, the target of $<$ 1dB/cm loss induced by the silica film has been achieved for two samples out of those measured. From the tables it can also be seen that, despite modifications to the sputtering system, the films have very different loss characteristics before they are annealed. Part of the variation is due to the difference in the film thicknesses — clearly thin films will cause less loss than thick films because less of the evanescent field is filled with the attenuating material. After annealing for just one hour the losses are reduced in all cases and are homogenized somewhat. Time constraints prevented the rest of the measurements being made to fill in the table which makes it impossible to identify any other strong underlying trends.

Only one of the samples received the full 4 hours of annealing. To illustrate the effect of annealing, the ratios of the outputs from the various y-junctions on this sample have been plotted in figure 5.2. Due to surface imperfections on the soda-lime glass substrates, not all of the devices on the chips transmitted light and so some of the waveguides are omitted from the analysis. The figure shows that there are smaller imperfections which cause the output ratios of the y-junctions to vary from device to device. By tracing the changes in output ratio with annealing

Thickness μm	% Oxygen	Deposition Temperature °C	TM loss (dB/cm ±0.2dB/cm)			
			No anneal	1 hour	2 hours	4 hours
0.62	0	ambient	3.87	2.98		
0.67	0	130	10.56	2.67	0.87	
0.56	0	200	3.53	2.47		
0.43	10	ambient	14.84	0.26	0.52	0.70
0.65	10	130	6.59	2.96		
0.49	10	200	8.27	0.58		
0.58	20	130	5.86			

Table 5.2: Waveguide loss induced by silica films deposited with different parameters and effect of annealing at 250°C :TM polarization

time on each device it can also be seen that there is a high degree of variance on each individual device as well as between devices. One may conclude from this that after the first hour of annealing, the beneficial effect of further annealing was much reduced.

The attempted porosity measurements gave ambiguous results which do not give a reliable indication of the porosity of the films. The drifts in output after the water was placed on the interferometers were slow enough to be due to temperature changes of the water. For this reason the results are not presented.

5.4 Summary

Deposition parameters have been found for silica films which induce losses less than 1dB/cm in an ion-exchanged waveguide. Losses vary greatly from sample to sample prior to annealing, but after annealing for 1 hour at 250 °C the losses are more evenly spread.

Taking the estimated losses for TE and TM polarisations together, the optimum parameters were chosen to be a deposition with 10% oxygen atmosphere at ambient temperature, followed by annealing for 2 hours or more. For the work in the next chapter, 4 hours of annealing was selected.

The attempt at evaluating the porosity of the silica films was unsucessful. The

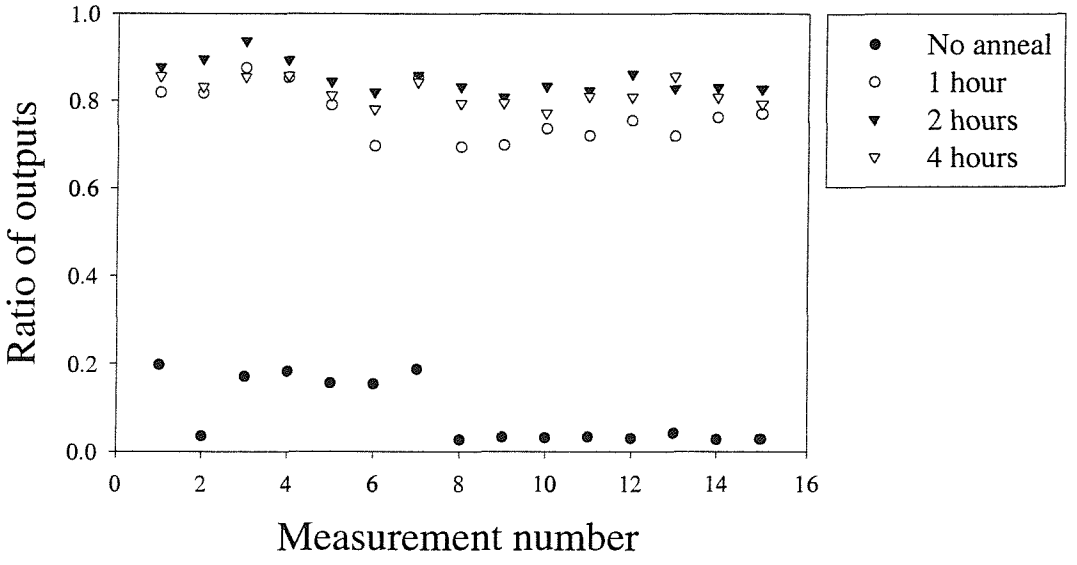

Sample deposited in 10% O_2 at 11 mTorr with no substrate heating.
Annealing was performed at 250 degrees Celsius in an O_2 atmosphere.

Figure 5.2: Transmission of waveguides coated with 5mm and 10mm long silica films as a function of annealing time

experiment was unable to distinguish between fluctuations in output due to penetration of the film by water and fluctuations due to temperature change.

This study is incomplete, but the extra information that would be gained by completing the study would probably not justify the expenditure of effort as the desired loss figures have been achieved. The films are sufficiently rugged for sensing applications and can be patterned by lift-off. The films are, however, still believed to be porous, which could be a problem for some applications. For the sensors reported here the silica films produced with the parameters found here meet the necessary specification, that of RIANA.

Chapter 6

Multi-channel fluorescence sensing experiments

6.1 Introduction

The work using Mach-Zehnder interferometers demonstrated that thin high-index films can be used to increase the sensitivity of evanescent wave integrated optical sensors by more than an order of magnitude. The degree of enhancement was in approximate agreement with the model despite the model only treating one dimension.

Whilst the refractometers proved useful as simple proof of principle devices, the use of fluorescence had been chosen for the transduction mechanism in RIANA. The transducers used for fluorescence sensing can be very simple in construction and they are far less sensitive to temperature than refractometers. The peak intensity of fluorescence also increases monotonically with the intensity of illumination and with the quantity of dye being excited.

In this chapter the development of multi-channel integrated optical fluoroimmunosensors, for use within RIANA, is described. The aims were to produce integrated optical sensors capable of multi-channel operation, using antibodies labelled with fluorescent Cy5.5 dye as the recognition element. This requires that the different sensing channels be at different positions on the chip and that the chip surface be compatible with the processes used in RIANA to provide regions to which the antibodies can specifically bind. Within this project there was also great emphasis on using cheap and flexible designs which can easily be extended in the future, for example to measure large arrays of analtyes. It had also been decided that the final sensors, produced by the project, would use fibre pigtails for delivery of light, giving mechanically stable input coupling and reducing the amount of optical alignment that an end-user would be required to perform.

For the purposes of a demonstration of the optical principles it was decided to restrict the sensors reported here to measuring a limited number of channels (2–4) and to only measure a single analyte at a time. In the course of the work in this chapter the only analytes examined were simazine and isoproturon. These analytes were chosen because the antibodies were known to be reliable early in the project. For both of these analytes the target limit of detection was 1 part per billion initially with the intention of achieving 0.1 parts per billion later.

Limiting the chemistry in this way enables some separation of optical effects from the performance of the chemistry. The chips used here also did not have fibre pigtails attached, although the later experiments did use a butt-coupled optical fibre to deliver light to the chip. At the time of performing these experiments, the in-house pig-tailing process was still under development and the extra fabrication time and risk of irreparably damaging chips could not be justified.

Fluorescent labels were used to identify and quantify antibody molecules at the surface of the sensor chip. This has many advantages, as described in chapter 2. RI-ANA also demands that devices be able to excite fluorescence at several well-defined positions on the surface of the chip simultaneously to allow multisensing. Achieving multi-channel operation simply through spatial separation of the different measurement areas allows a simple sensor design to be used in which the measurement zones are arranged in series along the length of the waveguide. This arrangement when used on a waveguide around 4cm long allows good spatial separation of a small number of measurement zones.

If losses along a device are high, the intensity of laser radiation will be much lower at the output end of the device than the input end and hence the sensitivity at sensing positions closer to the output may be correspondingly lower. One of the aims of these experiments was to ensure that the loss along the chips is not too high. Here we arbitrarily define "too high" as a loss of 1dB from one patch to the next. This loss figure would correspond to a factor of four difference in the optical power at the first and last patches of a six channel sensor. An alternative may have been to examine the signal:noise and insist that it remains within certain limits. The various contributions to loss are investigated and compared to the predictions of the numerical modelling. These experiments also look at the system as a whole and try

to track the performance limitations imposed by the different parts of the system. Connected with both of these things and of particular relevance to this thesis is an investigation into the optical power budget.

Concerns were raised by one of the project partners that the surface chemistry, to which the antibody molecules attach themselves, would not adhere properly to the Ta_2O_5 films. If this was the case then the sensors would either not work at all, or their performance would degrade rapidly with regenerations of the sensor surface. Another aim of these experiments was therefore to investigate the stability of the surface chemistry over the course of a large number of binding/regeneration cycles.

To assess the performance of the chips within the RIANA system, two sets of experiments were performed. In the first set of experiments a design for a multi-sensor chip was selected and the chip used in fluorescence experiments with only two measurement channels. The primary aim of these experiments was to ensure that the Ta_2O_5 films were compatible with the surface chemistry. The secondary aim of these experiments was to examine the loss along the chip for different Ta_2O_5 film thicknesses and to ensure that it was not excessive. The second set of experiments examined more closely the differences between the responses of uncoated regions of waveguide and those with Ta_2O_5 films. The second series of experiments also examines more closely the operation of different parts of the system and demonstrates the simultaneous use of four measurement channels. Detection limits well below the target figure of 0.1ppb were measured for the pesticide isoproturon.

These experiments demonstrate the feasibility of multi-channel integrated optical multisensors with detection limits of less than 0.1ppb. These experiments also reinforce the data from experiments performed using high index overlays on Mach-Zehnder interferometers to increase the proportion of guided power carried in the evanescent fields of the waveguide. They also show that devices fabricated with these films are compatible with RIANA, both in terms of low enough loss for multi-sensing and in terms of compatibility with the chemistry. The performance of the different parts of the system is investigated and the major limitations to performance identified.

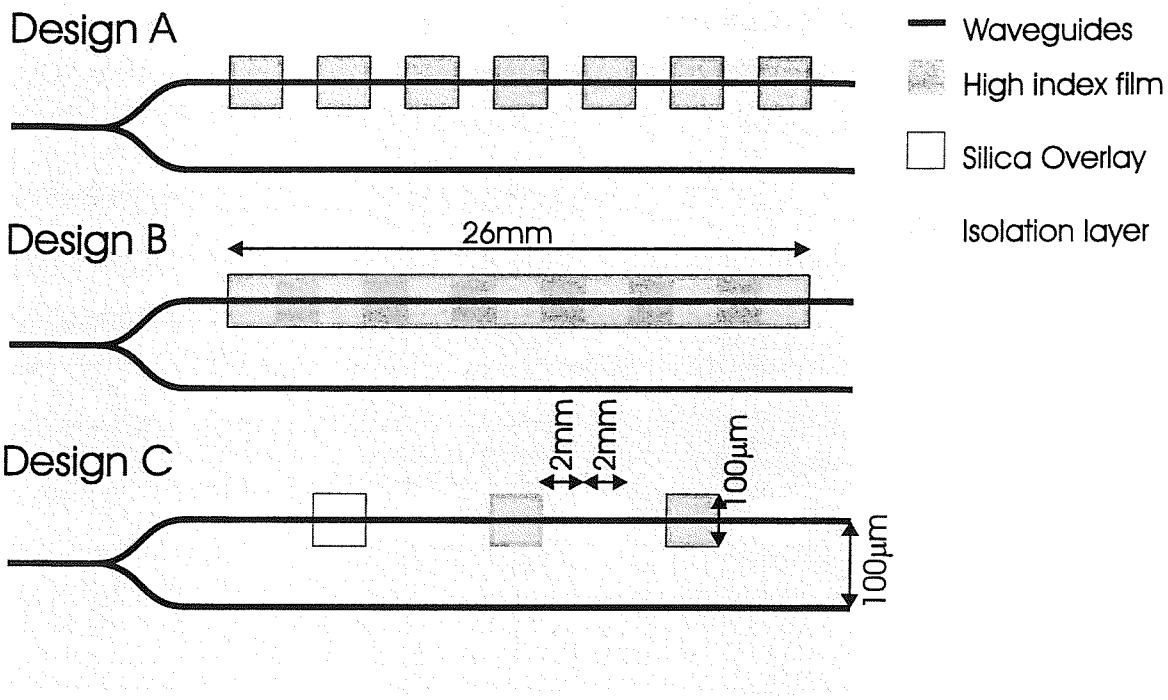

Figure 6.1: Devices designed for fluorescence sensing experiments

6.2 Two channel fluorescence sensing experiments

6.2.1 Design of integrated optical chips

The chips used for these experiments had two different designs of device on them, designated A and B in figure (6.1). The major difference between the two designs is that design A uses a series of short patches of tantalum pentoxide covering only the interaction zones and design B uses one long patch extending underneath the isolation layer between patches. Design C in the figure was used for the later experiments.

It was envisaged that the abrupt transitions between coated and uncoated waveguide would induce losses which would be larger for greater changes in the modal irradiance profile. In chapter 3 the loss induced by 30nm of a material of refractive index 2.1 was estimated at around 1.6 dB per transition. This figure will be dependent on the geometry of the underlying waveguide, and is based on a planar model rather than a channel waveguide.

It was also known that the high index films cause extra loss due to absorption and scattering. To ascertain which source of loss was dominant, a chip was fabri-

cated with 30nm thick tantalum pentoxide and a some simple measurements were performed. Light was coupled into devices of each type and the ratio of the outputs of the y-junctions measured by focusing them onto photodetectors. The superstrate medium was air for these measurements.

For the TM polarization the losses were 2dB and 7dB ±1dB for designs A and B respectively. The TE polarization yielded a loss figure of 4.5dB ± 1dB for design A. For design B the loss was so high that the waveguide output was not reliably distinguishable from the background of scattered laser light.

This simple experiment demonstrated very clearly that it is better for this waveguide geometry to use design A in which the high index film is only applied to the interaction zones than to apply one continuous film that covers all of the interaction zones as in design B.

6.2.2 Apparatus

These experiments were performed in Tübingen with the assistance of Albrecht Klotz and others in the optical spectroscopy group at Tübingen University.

The apparatus was as shown in figure (2.2) with the exception that rather than just a single collection fibre, detector and lock-in amplifier two fibres held with their centres 4mm apart in a precision machined holder were used, along with an extra detector and lock-in amplifier. The fibre holders used here were designed for use with up to 4 fibres, although in the final RIANA system this was extended to 6 fibres. Course alignment was made possible by making marks on the plate used to clamp the waveguide to the flow- cell and on the fibre holder. Fine alignment was found to be easiest performed by injecting a solution of fluorescent dye into the flowcell with the laser switched on and simply adjusting the alignment until all the measurement channels were simultaneously reading as high a signal as possible.

Illumination was by helium-neon laser operating at 632.8 nm wavelength. The laser was mechanically chopped and shuttered and the beam was free-space coupled into the waveguide end face using a $\times 10$ microscope objective lens. Two high numerical aperture (0.47), large core ($\approx 1mm$), polymer fibres were used for fluorescence collection. The collected light was passed through a Schott bandpass interference filter (DAD 8-1, max transmittivity 0.914 at 692.8nm, half-width 8.4nm) on to sil-

icon photodiodes with integrated amplifiers. The output from these was passed to commercial lock-in amplifiers which received their reference signal from the chopper. The analog outputs of the lock-in amplifiers were fed to a Keithley data acquisition board in a PC. Fluid handling was performed using a syringe pump system connected to an autosampler. The syringe pump has a multi-way valve that enables the input to be switched between different bottles of reagents, such as phosphate buffered saline (PBS), pepsin, etc. and the autosampler. The autosampler is a piece of equipment that can be loaded with a number of small samples in individual containers and then automatically load them into the system in sequence. Both the pump and the autosampler were controlled by the computer, allowing for a high degree of automation in the experiments. This proved to be of great use for acquiring large data sets.

Figure (6.2) shows the normalized absorption and fluorescence spectra of Cy5.5 dye and the transmission spectrum of the Schott filter. The laser wavelength range marked covers HeNe at 632.8nm and the laser diodes which were selected for the RIANA fluorescence experiments. The lasers were selected to have a wavelength on the shoulder of the absorption curve to minimise any change in absorption with changes in laser wavelength, commonly caused by temperature fluctuations. The figure also illustrates that the selection of filter is something which could be far better optimised — the current filters in use only transmit approximately 25% of the fluorescence emitted.

As in the earlier experiments, the waveguides in these experiments were formed by potassium-sodium ion exchange in soda lime glass. The waveguides were defined by 3μm wide openings in an aluminium mask. The ion exchange was performed for 25 minutes at a temperature of 400°C. The Ta_2O_5 films were deposited by reactive rf sputtering from a tantalum target in a 1mTorr:10mTorr oxygen:argon atmosphere and were measured to be approximately 20nm and 30nm thick. The silica isolation layer was deposited by rf magnetron sputtering from a silica target in a 6mTorr:17mTorr oxygen:argon atmosphere. Surface modification was performed using the standard techniques described in chapter 2 to give a simazine sensor.

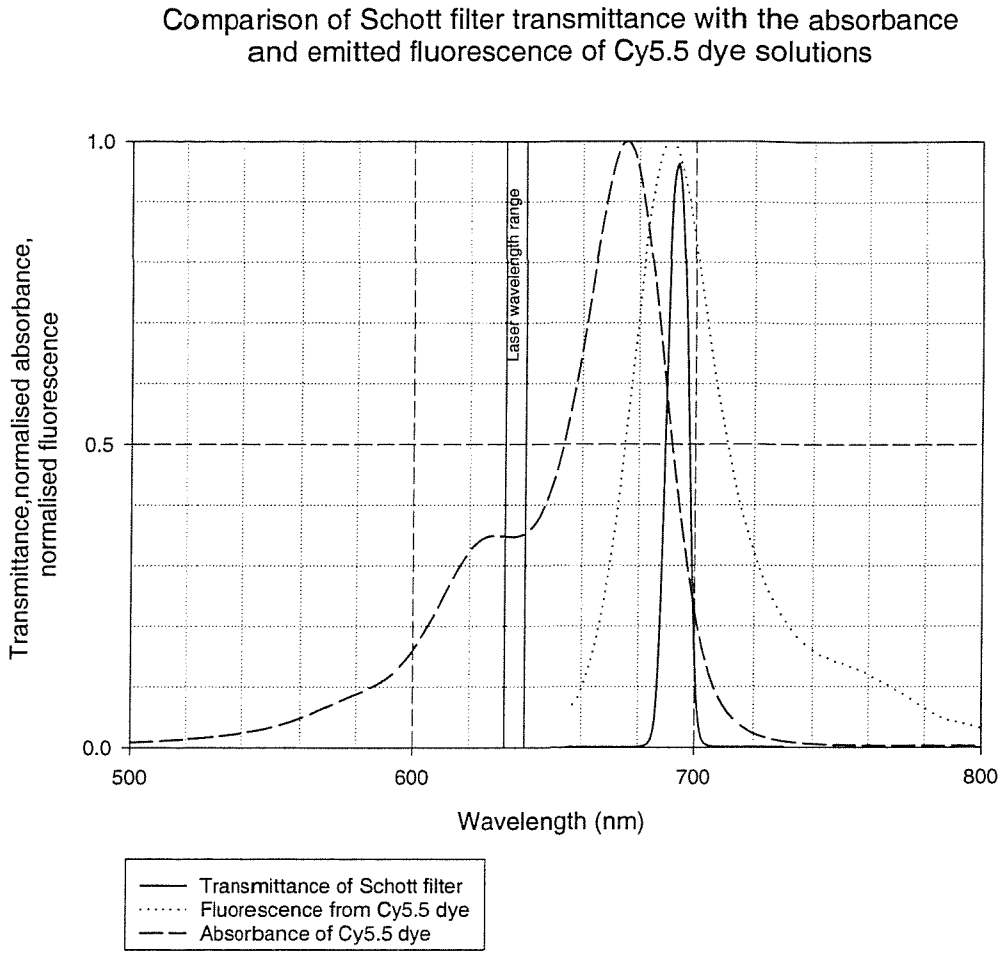

Figure 6.2: Normalized fluorescence and absorption spectra of Cy5.5 dye compared with the transmission spectrum of the Schott filter

6.2.3 Bulk dye experiments

Comparison of TE and TM responses to fluorescent dye solution

Bulk solutions of Cy5.5 dye in PBS were prepared. By absorption measurements in a spectrophotometer, the concentration of the primary solution was calculated to be 5×10^{-7}M.

Samples of the dye solution were pumped over the sensors, immediately preceded and followed by a continuous stream of PBS. The difference in collected signal, averaged over 30 seconds, between when the buffer flow and the dye are in the flow cell was measured.

By scanning the collection fibres spot by spot along the chip and injecting dye solution, the variation of the response to fluorescent dye solution along the length of the waveguide was established. By measuring several places with both fibres it was possible to see the extent of the differences between the two measurement channels. Due to time constraints, these measurements were only performed to completion on the chip with a 30nm overlay. The results are shown in figure 6.3. Losses were found by fitting exponentials to the data. A simple single exponential is however a poor fit to the data as the measurements all include a level of background radiation that does not decay significantly along the chip, so a constant was included in the fit. This background may come from various sources, such as substrate modes, ambient light and simply scattered light from the laser source.

The exponentials fitted to the data in this figure are fitted to all the data, but the first measurement position gives an abnormally high response for both polarisations, probably due to a high intensity of non-coupled light. Ignoring the spurious first point, fitting exponentials gives a loss figure of 5-6dB/cm for the TE polarization. For TM any loss is smaller than the uncertainty in the data.

Comparing these loss figures with those from the measurements of the ratio of the outputs of the device with air as a superstrate we obtain an estimate of the loss contributions from the silica isolation layer and the Ta_2O_5 film. The ratio of the outputs gives the loss from seven 2mm patches of Ta_2O_5 as being 4.5dB above the loss of the reference arm which is coated in silica. This then gives the loss of the Ta_2O_5 patches as 3.2dB/cm *above* the silica loss. Using the higher estimate of loss for the TE mode of the device, we get loss due to the isolation layer of 4.4dB/cm and due to the Ta_2O_5 patches of 7.6dB/cm. The target figure was a loss of 1dB from one patch to the next - a distance of 4mm (length of one patch + spacing). The target is therefore a total of 2.5 dB/cm for these devices. Despite the excess loss, the response of the sensor was measureable at all seven patches.

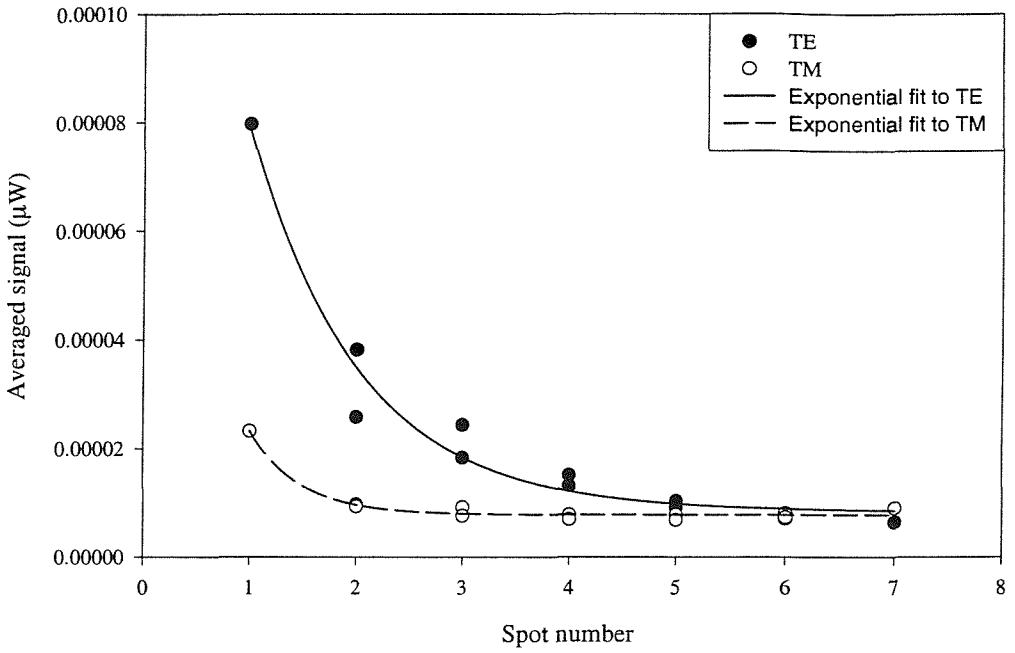

Figure 6.3: Responses to bulk dye solution along chip with 30nm Ta_2O_5 patches

6.2.4 Antibody experiments

Choice of antibody concentration

The experiments with bulk dye solutions yielded useful information about the performance of the chips, but for sensing in the RIANA project there is the added compexity that the fluorescent dye is atttached to antibodies that attach themselves to the sensor surface. The main aim of the antibody experiments was to test the compatibility of the sensor surface with the chemistry that allows the antibodies to attach themselves to it. This was examined by performing a large number of test cycles using as much automation as possible to make the cycles as reproducible as possible. Isolation porosity was examined, comparing the penetration of bulk solutions of Cy5.5 dye with dye-labelled antibodies. Finally in this section, calibration curves were generated for the sensors to show how far from the target sensitivity the sensors were.

Figure 6.4 shows an example antibody test cycle for the fluorosensors under investigation. At the beginning of the measurement a baseline is recorded with the

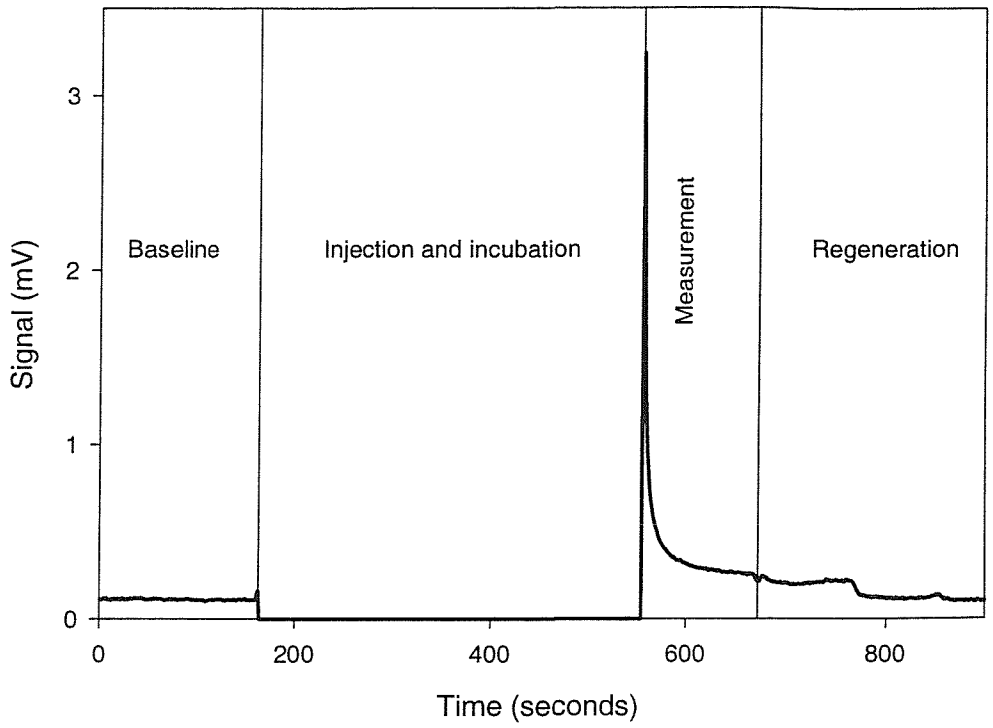

Figure 6.4: Example antibody test cycle

laser switched on and no fluorescent material being injected. A continuous flow of PBS is pumped through the flowcell during this time. This baseline measurement gives the background signal caused by scattered laser light that has passed through the filter and any fluorescence of the materials used in the fabrication of the sensor. Whilst the sample containing the labelled antibodies is injected into the flow cell and given time to "incubate" and bind to the sensor surface the laser is switched off or blocked by a shutter. Rinsing with PBS then begins again and the shutter is opened/laser switched on. The reason for stopping the laser illumination of the sample can be clearly seen from the response after illumination is resumed. In the intense light the Cy5.5 dye is rapidly photobleached, causing the decay in collected fluorescence that can be seen in the figure. After a period of time, 120 seconds in this case, regeneration of the sensor surface first by injection of pepsin and then by injection of 50:50:1 acetonitrile : water : propionic acid begins. The sample is then left being rinsed by a flow of PBS once again. To perform comparative

measurements, the signal from collected fluorescence is integrated over all or part of the time between the shutter opening and regeneration of the surface beginning. From this figure is subtracted the integral of the baseline over the same length of time yielding a signal difference which represents the change in signal caused by the presence of the fluorescent material.

As a preliminary check that the surface chemistry was working, antibody solutions of different concentrations were injected and the responses measured. The results are plotted in figure (6.5). This demonstrates the way that the collected fluorescence varies with the amount of antibody that is in solution and hence the amount that binds to the sensor surface. For immunoassays a concentration of 0.5μg/ml of antibody was used. The choice is somewhat arbitrary and so could be optimised much further. In general, the choice of antibody concentration is a trade-off between detection limit and dynamic range. High antibody concentrations allow measurements over a large range of analyte concentrations, but they tend not to perform so well at very low concentration. Low concentrations give a small range before all the antibody is bound to analyte molecules but tend, due to the form of a calibration curve, to be useful at lower analyte concentrations.

Porosity of the isolation layer

To complete the earlier work on the responses of the sensors to dye solutions at different points along the chip, a brief examination of the porosity of the silica isolation layer was performed, in this case with both bulk dye solutions and with antibody solutions.

The collection fibres were placed over the isolation layer between measurement spots and dye solution pumped through. This was also performed for antibody samples, with the different test cycle that entails. The graphs in figures(6.6, 6.7) show that the dye penetrates the isolation layer when in solution, but the dye labelled antibody does not penetrate the silica film.

Performance of sensor after multiple regeneration cycles

Large numbers (around 50) of identical samples, containing antibody in PBS with ovalbumin, were injected making use of the autosampler. The automation of the

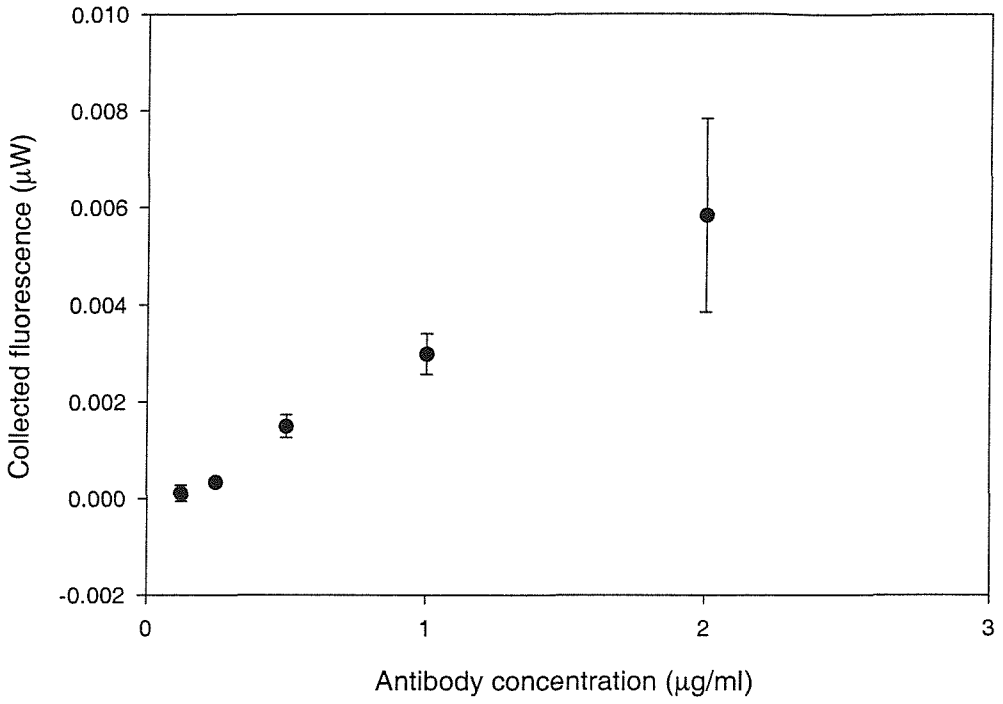

Figure 6.5: Variation of collected fluorescence with antibody concentration

experiment helps to ensure that the timings of test cycles are identical from one sample to the next. Figure (6.8) shows the response for repeated samples of the same antibody concentration on two consecutive days of experimenting. This experiment was performed after the chip had been calibrated, a task which itself involved a similar number of regeneration cycles. The jump in response between the two days is believed to be due to a change in input coupling to the chip. This clearly shows that there is no significant degradation in the performance of the surface chemistry, despite the chip having been regenerated over 150 times in the course of the experiments. This establishes that Ta_2O_5 is a suitable material for chemical attachment using conventional protocols.

It is also an important re-affirmation of the choice of silica as the isolation layer material that, on the completion of these experiments, there was no significant degradation of the silica isolation layer. Once cleaned, the samples did not show any damage due to mechanical contact with the o-rings or due to attack by the chemicals.

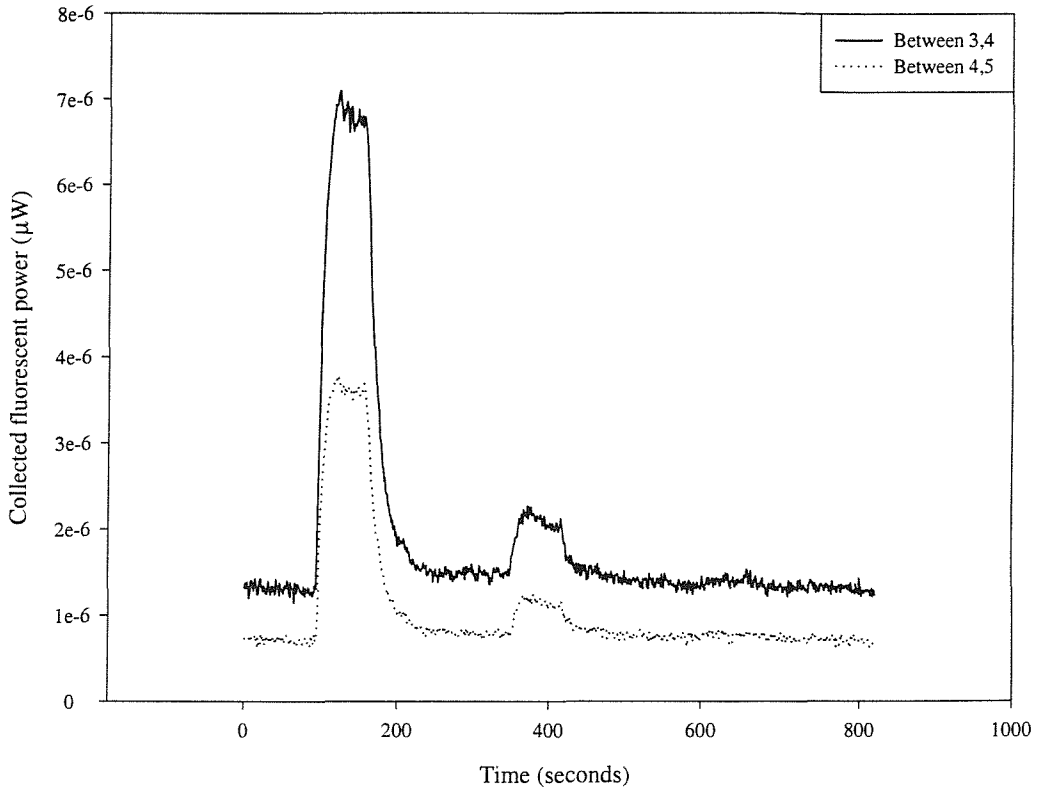

Figure 6.6: Responses to bulk solutions of Cy5.5 dye between patches on chip with 30nm Ta_2O_5 overlay

In this respect these films show a great improvement over the fluoropolymer films used in chapter 4.

Calibration curves

As part of the investigation into the performance of these chips over a large number of test cycles, samples containing simazine to a known concentration were injected. Five concentrations from 0 to 100ppb concentration were injected cyclically in repeated order. The repeated order aids this examination of reproducibility of measurements, but for an accurate calibration curve it is normally considered to be better to inject the samples in random order and so to give a better idication of how the sensor will perform under "real" conditions.

This was performed for both chips. The means of the data have been calculated

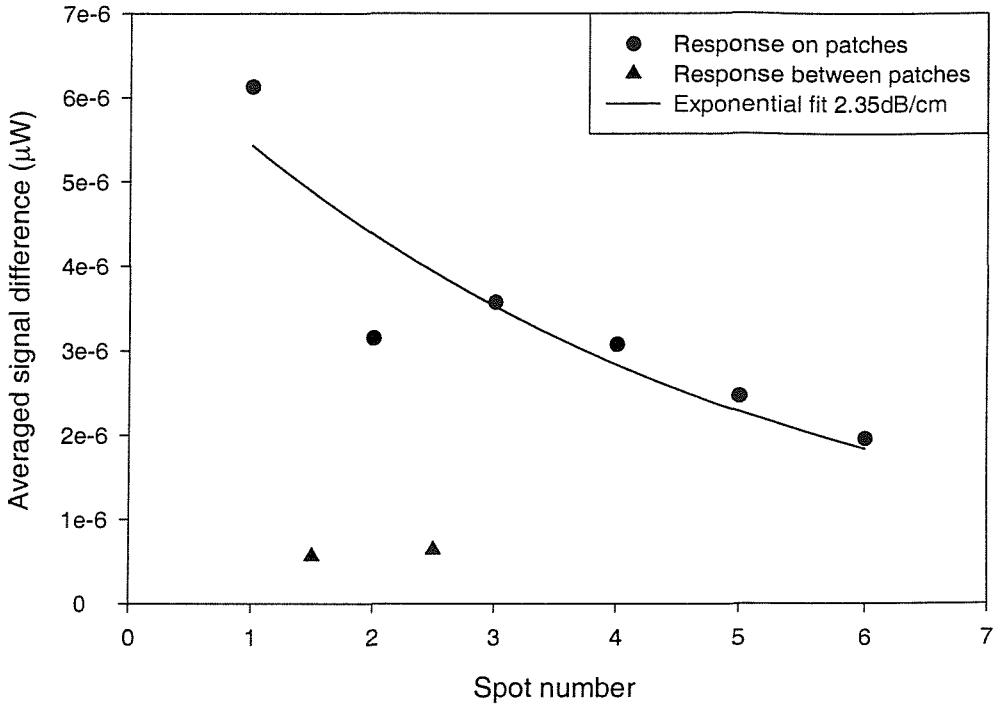

Figure 6.7: Response to Cy5.5 dye labelled antibody between patches on chip with 30nm Ta_2O_5 overlay

and normalised such that the mean signal at 0ppb pesticide is equal to 1. Logistic functions were fitted to these data as shown in figure (6.9).

The limit of detection is conventionally calculated as being the analyte concentration that gives a signal three standard deviations away from the 0 ppb point. This represents that interval that approximately 95% of the measurements will fall into when measuring blank water samples with no analyte present.

The calculated detection limits for these two chips were 0.14-0.19ppb for the chip with 20nm Ta_2O_5 and 0.33-0.61ppb for the chip with 30 nm Ta_2O_5, the two figures for each chip being due to the two measurement channels. The thicker Ta_2O_5 overlays have not improved the overall sensitivity of these devices in the way that was expected. This may largely be due to errors in sample preparation, as indicated by the large error bars on the 0.1ppb data. Another major factor is believed to be the high rate of photobleaching, which effectively caps the total amount of fluorescence

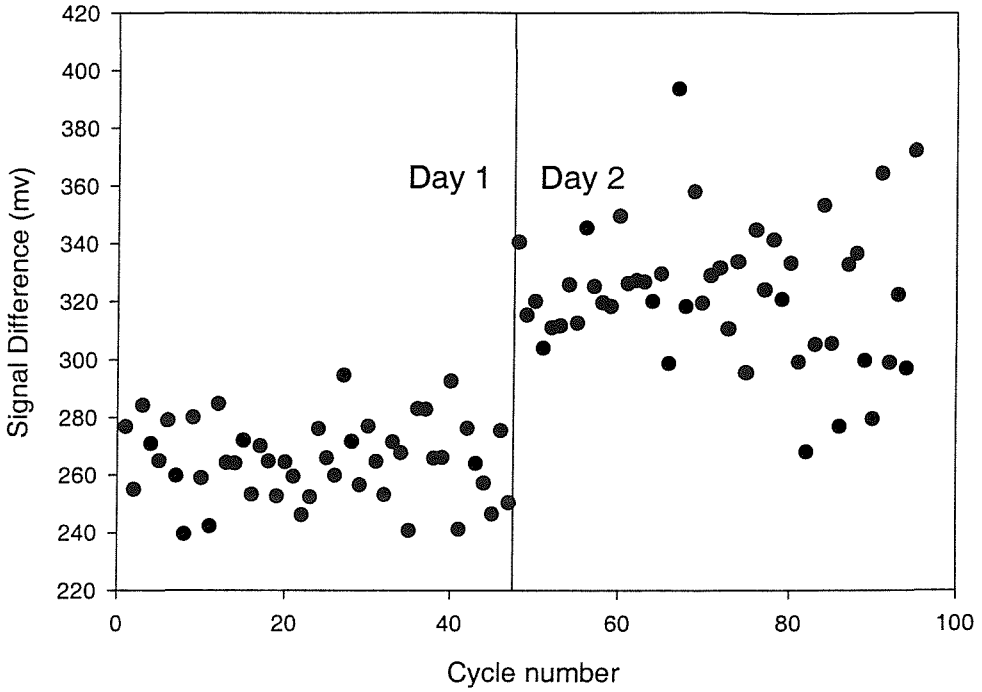

Figure 6.8: Response to many antibody samples of identical concentrations on two consecutive days

which can be emitted.

6.2.5 Conclusions from preliminary measurements

In this section the reliability of the surface chemistry on Ta_2O_5 has been proven. Chips were found to perform well after more than 150 surface regenerations. These experiments have also demonstrated immunosensing on two channels simultaneously, and that all seven sensing postions on the test devices gave measurable responses to fluorescent dyes.

However, losses in the chips are very high — 5-6dB/cm having been measured on one chip, compared with the target of less than 2.5dB/cm or 1dB from patch to patch. Large contributions to this loss come from both the silica isolation layer and the Ta_2O_5 measurement patches. For future experiments it was decided to make use of the results of the silica optimisation study, presented in chapter 5, which were

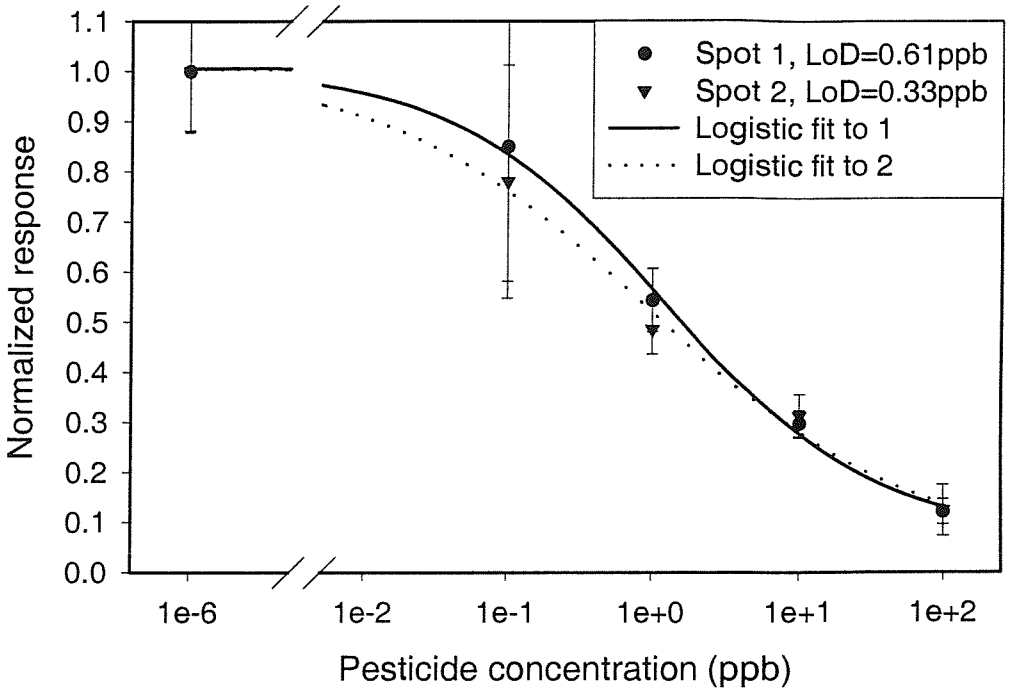

Figure 6.9: Calibration of chip with 30nm Ta_2O_5 overlay

not available at the time of these experiments. The loss due to the windows and the Ta_2O_5 films were left for further investigation. High loss is a potential stumbling point for this technology. When performing the measurements along the chip, it was noticed that the first measurement position was giving a spuriously high response. This is believed to be due to non-coupled laser light, which would mean that the efficiency of input coupling needs to be improved.

The isolation layer was also found to be porous. This has the effect for experiments with bulk dye solution that the dye passes through the isolation layer and is excited by the laser. For the antibody experiments the isolation layer was successful in keeping the labelled antibody away from the waveguide surface. For RIANA the isolation of the waveguide from the analyte is not of high importance, partly because within the project were efforts to print the surface chemistry only on the areas where it is needed using drop-on-demand technology. The more important function of the isolation layer is to prevent the black nitrile rubber o-ring, used for sealing the flow-cell to the chip, from being in direct contact with the surface of the

waveguide as this can induce high losses.

More signal was received from fluorescence on the 30nm device than the device with 20nm Ta_2O_5. This is what the model had predicted and what was seen in the previous experiments. TE excitation gave larger responses than TM as was also expected.

6.3 Four channel fluorescence sensing experiments

6.3.1 Introduction

In this second series of fluorescence sensing experiments, the measurement system was extended to measuring four channels simultaneously. The main purpose of these experiments was to demonstrate a highly sensitive integrated optical multisensor for the pesticide isoproturon. To aid in this it was decided to perform large numbers of identical test cycles so that the optimum method of data analysis could be found. In particular, it is expected that, in the presence of photobleaching, there would be an optimum time to integrate the fluorescence signal over. If the intensity of fluorescence were constant then the optimum would essentially be to integrate for as long as is practical. In the presence of strong photobleaching, long integration times introduce significant extra errors due to transient effects such as changing coupling between the laser and the waveguide or drifts in the intensity of the laser.

The extra measurement channels were also used to investigate the increase in evanescent power due to the Ta_2O_5 films and to verify the compatibility of the technologies in use with multi-sensing in RIANA. For these experiments the apparatus used was changed to a setup that bears closer resemblance to that which may be found in a RIANA instrument than that used in the earlier experiments. The changes included illumination by an electronically controlled fibre-pigtailed diode laser and using electronics designed in-house specifically for the RIANA project, rather than commercial lock-in amplifiers.

The optical enhancement caused by the high index films and the resulting change in performance of the chips with the immunochemistry were compared by measuring the fluorescence emitted from bulk dye solutions and from bound antibody. Calibration curves were then generated using standard solutions of analyte. For these

experiments the analyte was the pesticide isoproturon.

The devices for these experiments were fabricated using new parameters from the silica study in chapter 5. A secondary aim of the experiments was to evaluate the difference in performance as a result of these changes. It was hoped that the loss from the silica isolation layer would be significantly reduced, allowing more accurate measurement of the loss induced by the high index films.

6.3.2 Apparatus

The devices on the chips used for these experiments were produced following design C in figure(6.1). Once again, the ion-exchange was for 25 minutes at 400 °C through 4μm openings in an aluminium mask. Ta_2O_5 films were deposited by reactive rf sputtering from a tantalum target in a 10mTorr:1mTorr Argon:Oxygen atmosphere at 400W rf power to give films 20 nm and 30 nm thick respectively on the two samples. Silica films were deposited by rf magnetron sputtering from a silica target in a 10mTorr:1mTorr Argon:Oxygen atmosphere at 200W. This yielded films 640nm and 700nm thick using the same parameters and deposition time in each case. In the cases of both Ta_2O_5 and silica films, no substrate heating was used during deposition and patterning of the films was performed by a standard lift-off process. After the silica deposition, the samples were thoroughly cleaned in solvents and then in fuming nitric acid in order to remove all remaining photoresist. The samples were rinsed in de-ionised water, dried and then 'annealed' at 250°C for four and a half hours in an oxygen atmosphere. The silica deposition was performed without substrate heating, despite one measurement in 5.1 of a film deposited at 200°C which would indicate lower loss. There are two significant reasons for this. Firstly, the difference was smaller than the variations within the data. Secondly, when photoresist is heated to 200°C for long enough to sputter 700nm of silica, the photoresist can start to degrade, making the lift-off process more prone to failure.

A pigtailed laser diode from Point Source was used to supply radiation at 637.7nm wavelength via a polarisation maintaining fibre. Input coupling to the sensor waveguide was via butt coupling with the cleaved end of the fibre. By holding the fibre in a rotating chuck it was possible to select TE and TM polarisation by changing the orientation of the optical axis of the fibre with respect to the waveguide.

Collection of the emitted fluorescence was by four large core, high NA, polymer optical fibres. The ends of the fibres were hand polished using standard alumina lapping films, commonly used for polishing optical fibres. The collection ends of the fibres were held in a precision machined chuck, holding the fibres in a straight line with their centres 4mm apart. The four measurement channels that were used for most of the experiments corresponded to the 3rd to 6th measurement patches, counting from the optical input end. This gives alternating measurements on bare waveguides and patches overlaid with Ta_2O_5 films.

Perkin Elmer supplied four lock-in amplifier boards and interface electronics made to the in-house design. These were used in conjunction with four collection fibres and detectors to collect and measure the fluorescence from four measurement patches simultaneously. The lock-in amplifiers an interface were made into a unit with outputs to a computer and to the laser. An extra output was also added to make the modulation source for the lock-in amplifiers available to the external lock-ins that were used when measuring the waveguide outputs. The lock-in unit can use an internal modulation source or can take modulation and shutter control from digital inputs.

A Keithley DAS 1601 data acquisition board was used to record data from the lock-in amplifiers. This board was also used to provide modulation and shutter control. The board came with DriverLINX libraries which were used in Borland C++ Builder to write data acquisition and control software for windows 95/98. This software allowed the rate of recording data, the modulation frequency and the shutter to be controlled from a graphical user interface. During acquisition the data from up to 8 channels was displayed numerically and graphically. The software also has the ability to perform many runs automatically, starting and stopping the FIA at the beginning and end of runs and saving the data to separate files. While it is possible to fully control the FIA from the computer, it was decided to program the FIA using its own interface and then simply starting and stopping the program from the computer. Full FIA control may be viewed as a possible future enhancement to the software. Another program was also written to perform analysis on the sets of data files produced by the data acquisition software.

The four fluorescence detectors were calibrated against an optical power meter

by collimating the output of the diode laser and passing it through combinations of neutral density filters. The calibration lines for the four detectors are shown in figure(6.10) with the gradients shown in the key. The detectors show slight differences in response, but the calibration made use of the lock-in amplifier unit and the A/D card in the computer. Some variations in the response may be due to this.

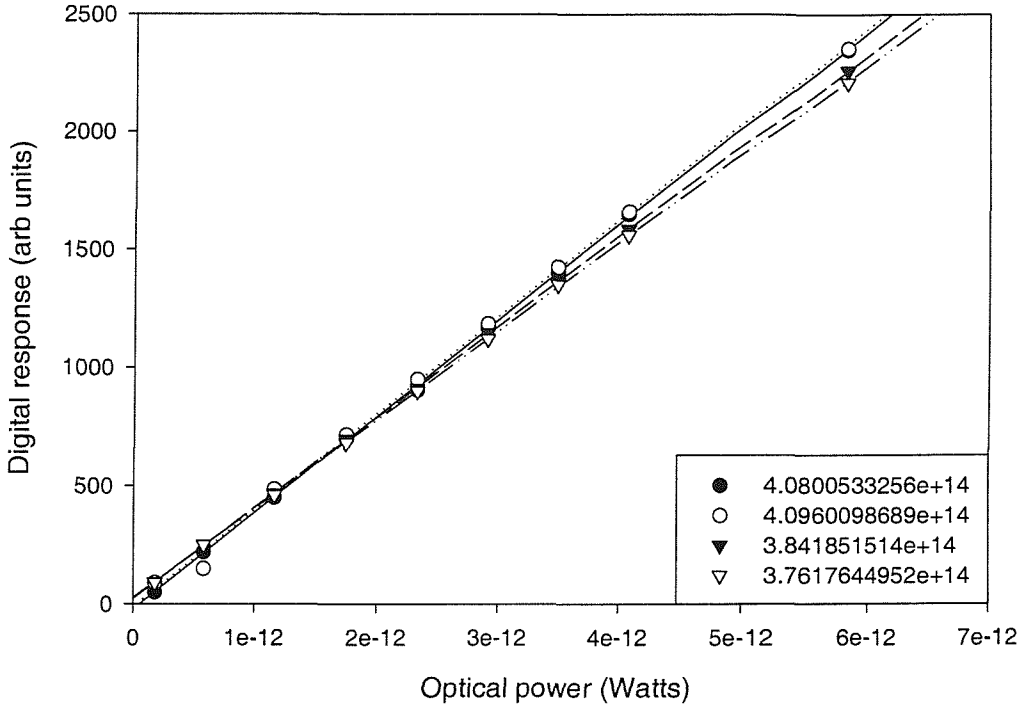

Figure 6.10: Detector calibration

Two detectors connected to commercial lock-in amplifiers were used to measure the waveguide outputs. These detectors were calibrated in a similar way to the fluorescence detectors, although the power level was several orders of magnitude higher.

6.3.3 Optical power budget

In order to know where potential weaknesses lie in the optical excitation and detection system, it is necessary to trace through the optical power reaching the different parts of the system. This is also of critical importance for selecting sensitive enough detectors to measure the collected optical power.

Refering back to figure(2.2), the light source has changed slightly for these experiments but the system still essentially consists of a laser exciting a waveguide which has fluorescent material bound to it's surface. Fluorescence travels in all directions, including right through the chip and some of the fluorescence is collected with high NA fibres at the back face of the chip. The other end of each fibre is held next to an interference filter, the other side of which is a detector for each fibre. The detectors are connected to lock-on amplifiers which are connected to a PC for data acquisition. In this section, the power arriving at the detectors is estimated such that suitable choice of detectors can be made. These calculations are also useful for highlighting the inefficiencies in the fluorescence collection system. The figures used here are mostly selected for simplicity rather than accuracy – the aim was to have an order of magnitude estimate of the power arriving at the detector. In practice, the power on the detector will vary over several orders in the course of a series of experiments.

The Point Source diode laser produces an output power of 3.05 mW. Of this power, approximately 1mW reaches the bare end of the fibre at the waveguide input. This serves as an upper estimate of how much guided power there was in the waveguide. It is of interest to know how much power is in the evanescent field of the guided mode and how much power the dye emits as fluorescence. Some effort has been made to know the responsivity of the detectors. Unfortunately the filters used are designed to operate correctly for light at normal incidence. Due to the high numerical aperture (0.47) of the fibre, angles up to 30 degrees are present. The manufacturers of the filters were unable to provide any information about the performance of the filters when used in this way. From comparison of the transmission spectrum of the optical filter with the emission spectrum of the dye, it is estimated that roughly 25% of the collected fluorescence passes through the filter.

The filter is 5mm thick and, combined with space in the detector housing, this

means the end of the fibre is a minimum of 6mm away from the detector. Again, the high numerical aperture of the fibre means that the cone of light is broad and only 11% of the collected light will reach the detector — assuming uniform proportions of the light at each angle.

A simple model of the collection of fluorescence is to assume that the dye emits isotropically. Ignoring the effects of the glass slide, 2.7% of the emission from a 2mm long 10μm wide fluorescent strip would be collected by a fibre 1mm away and perfectly centred on the patch.

Combining these figures gives an estimate that 0.07% of the emitted fluorescence is collected and reaches the detector. This figure is low, but the losses due to the presence of the filter are necessary if the fluorescence is not to be lost in collected background radiation. Despite the filtering, the signal due to background radiation is easily measurable - this is the baseline in all the calculations.

From the detector calibration and the above collection efficiency we can get from the measured signal to the power collected to the power emitted. To get from the power emitted to the evanescent power we need to know the number of dye molecules fluorescing. Knowing the dye concentrations used for bulk dye experiments, we need to calculate the volume of the evanescent field.

The refractive index of the glass is 1.51 and is increased by no more than 0.01 during ion-exchange. The effective index of the guided mode may therefore be estimated as 1.52. The refractive index of the buffer solution is estimated as 1.33 — the refractive index of water. The electric field in the superstrate is given by:

$$E(x) = E^{+}e^{-i\alpha x} + E^{-}e^{i\alpha x} \tag{6.1}$$

where

$$\alpha = \sqrt{n^2 k_0^2 - n_{eff}^2 k_0^2} \tag{6.2}$$

In the superstrate, α becomes imaginary. The amplitude of the exponentially growing term must be zero for a guided mode. The intensity of light varies as the square of the field strength. This yields the intensity profile as:

$$I(x) = I_{max} e^{-2k_0\sqrt{(n_{eff}^2 - n^2)}x} \tag{6.3}$$

The dimensions of the waveguide we estimate as 10μm wide by 2mm long. The quantum yield of the dye is quoted by the manufacturer as greater than 0.28. In

the case of the dye solutions used in the four channel experiments, the absorptance of the dye solution was measured as approxiamtely 0.03 at 638nm wavelength over a path of 5mm. The power incident is the integral of the intensity multiplied by the waveguide width over the depth of the evanescent field, given by:

$$P_{incident} = 10\mu\text{m} \times \int_0^\infty I(x)dx \tag{6.4}$$

$$\approx I_{max} \times 10\mu\text{m} \times 70nm \tag{6.5}$$

$$\approx I_{max} \times 0.7\mu\text{m}^2 \tag{6.6}$$

The power emitted is 0.28 times the power absorbed and so is given by:

$$P_{emitted} = I_{max} \times 0.7\mu\text{m}^2 \times 0.03 \times 2/5 \times 0.28 \tag{6.7}$$

$$\approx 2.4 \times 10^{-15} m^2 \times I_{max} W m^{-2} \tag{6.8}$$

Putting this together with the collection efficiency we can estimate that for 1pW collected the intensity at the surface of the waveguide would be $563000W/m^2 = 563mW/mm^2$. Compare this with the intensity of a 1mW laser focussed onto an area 10μmby 10μm, which is $10000mW/mm^2$. If the actual intensity at the surface of the waveguide were around $10000mW/mm^2$ the collected fluorescent power we would expect would be 18 pW. In this way the choice of suitable detectors was made.

6.3.4 Bulk dye experiments

Average response to samples of bulk dye

An example of the test cycles obtained with bulk solutions of Cy5.5 in PBS is shown in figure 6.11. A test cycle involves measuring the signal with a flow of phosphate buffered saline (PBS) through the flow cell. A sample of dye is then automatically drawn from a bottle and injected into the flow, giving the response. The flow cell is then rinsed by the PBS and the signal returns to the baseline level. The PBS contains 0.05% by volume of Tween 20, a surfactant, to aid in rinsing. This has been shown to reduce the amount of dye that adsorbs to surfaces in the flow system.

From test cycles such as the one in figure(6.11), the received power is integrated for 100 seconds during the dye pulse and for 100 seconds of the background, to

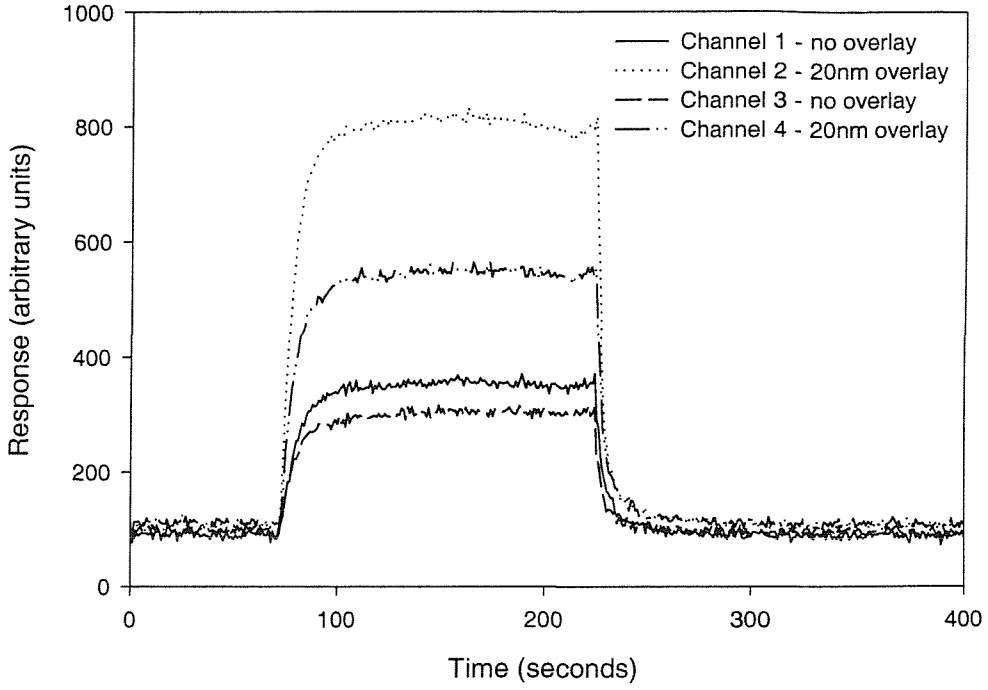

Figure 6.11: Response of four measurement channels to samples of Cy5.5 dye solution

establish a baseline. The difference of the two integrals is taken as the signal due to the fluorescence of the dye. The mean and standard error of the mean of the integrated signal difference was found for each channel on each chip. To investigate the usefulness of referencing the data with the power out of the end of the waveguide the comparison in figure(6.12) was performed. Here the standard error is divided by the mean and plotted for each channel on one chip. This is used as an analogue of a noise:signal ratio. The same is done for data that prior to averaging was divided by the recorded signal from the waveguide output. It can be seen that there is little variation in the ratio of standard error:mean from channel to channel, but that referencing with the waveguide output made a significant reduction. This is because referencing can help remove the effects of variations in input coupling from run to run. If the input coupling were completely stable, as might be found if one were to use a pigtailed chip, referencing would cease to be useful.

The mean signal difference, when simultaneously meauring the same dye solution

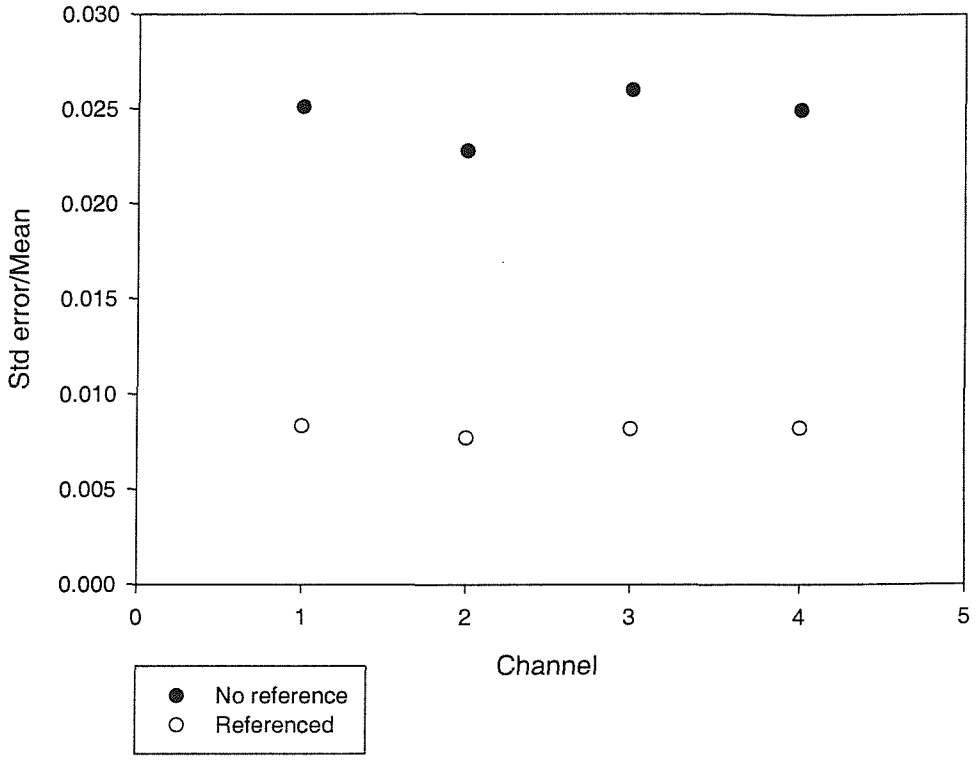

Figure 6.12: The effect of using a reference signal on the ratio of standard error to the mean response

on each of the four channels, is a quantity that can be used to directly compare the different waveguide geometries. By interpolating between the data from coated and uncoated patches estimates were formed of the magnitude of signal increases due to the Ta_2O_5 films, given as an enhancement factor. The responses at the different patches were also used to estimate the loss along the chip. In both cases two estimates are generated as a means of evaluating the error in the estimates. These are given in table(6.1).

Response to bulk dye solution at different positions along the chip

The relative performance of the different fluorescence collection and measurement channels was not well known. A simple experiment was devised to investigate this and to ensure that the differences in sensitivity were not significant to the interpre-

Thickness of overlay (nm)	Polarization	Enhancement factor		Loss (dB/cm)	
		1st Est.	2nd Est.	1st Est.	2nd Est.
20	TE	3.0	2.7	1.3	2.6
20	TM	1.8	1.7	1.5	2.0
30	TE	9.9	9.1	0.9	2.0
30	TM	2.7	2.6	0.7	1.01

Table 6.1: Enhancements and loss calculated from responses to dye solutions

tation of the results.

The four collection fibres were moved to different positions along the chip to allow comparative measurements of the different spots with the different measurement channels. The results are shown in figure 6.13. These data illustrate that the variations in fluorescent power at the different sensing positions are significantly greater than the variations due to the small differences in sensitivity of the measurement channels.

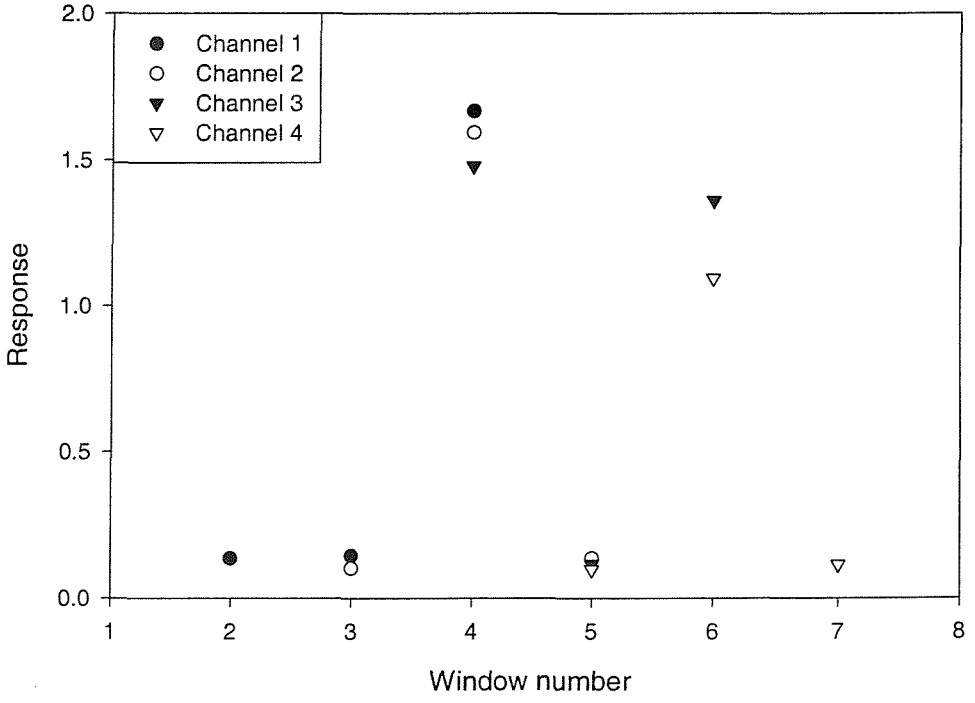

Figure 6.13: Responses at 6 patches

6.3.5 Antibody experiments

Overview

As in section 6.2, the greater interest in these experiments was in the performance of the sensors when binding antibodies labelled with fluorescent Cy 5.5 to the surface of the sensor. The major purpose of the experiments described in this section was to investigate how the integrated optical transducers perform when used in a manner as similar as possible to the RIANA system and to show that sensitive integrated optical multi-sensors can be produced with the technology presented in this thesis.

The approach taken was divided into two sets of experiments. The first experiments looked at the performance of the system by using antibody solutions of a single concentration and without any analyte molecules present. A large number of binding/regeneration test cycles were performed to allow statistical analysis. It was hoped that using the statistics gained from this it would be possible to find the optimum way to get a response figure from the collected fluorescent power despite the very rapid photobleaching. These data were also used to investigate the enhancement by the Ta_2O_5 films of the fluorescent power. Using the chips with alternating Ta_2O_5 coated and bare waveguide sensing patches a direct comparison was possible. The large number of regenerations of the sensor surface also served as another opportunity to verify that the Ta_2O_5 surface is compatible with the surface chemistry to which the antibodies bind.

System evaluation using single concentration antibody solutions

The antibody test cycle was similar to that used in section 6.2 and is shown in figure (6.4). A baseline reading is measured with PBS flowing through the flowcell. The laser is automatically switched off and the sample of analyte with antibody and ovalbumin in PBS is injected into the flowcell and allowed to bind to the surface. Rinsing with PBS then begins and the laser is switched on again. After 140 seconds regeneration of the sensor surface then begins using first pepsin and then a mixture of acetonitrile, propionic acid and water. The sensor is rinsed in PBS and then another test cycle can begin.

The antibody in the case of these experiments was 0.5 μg/ml anti-isoproturon

labelled with 1.5 dye molecules per antibody. A stock solution of antibody with ovalbumin at 100μg/ml added was prepared for each days experiments. This stock solution was automatically drawn into the sample loop and injected into the flow cell with the intention that the automation would increase the reproducibility of the experiment.

Figure (6.14) shows an example of the response to the antibody solution. This example is from the chip with the 30nm Ta_2O_5 overlay. It can be seen that initially the signal is increased for the patches with high index films in roughly the same manner as for the bulk dye solutions. The decay that follows this is at an increased rate however, as is highlighted in figure (6.15). In this graph the response curves have been normalized to a maximum value of 1 and the DC baseline component has been removed so that the rates of decay can be compared.

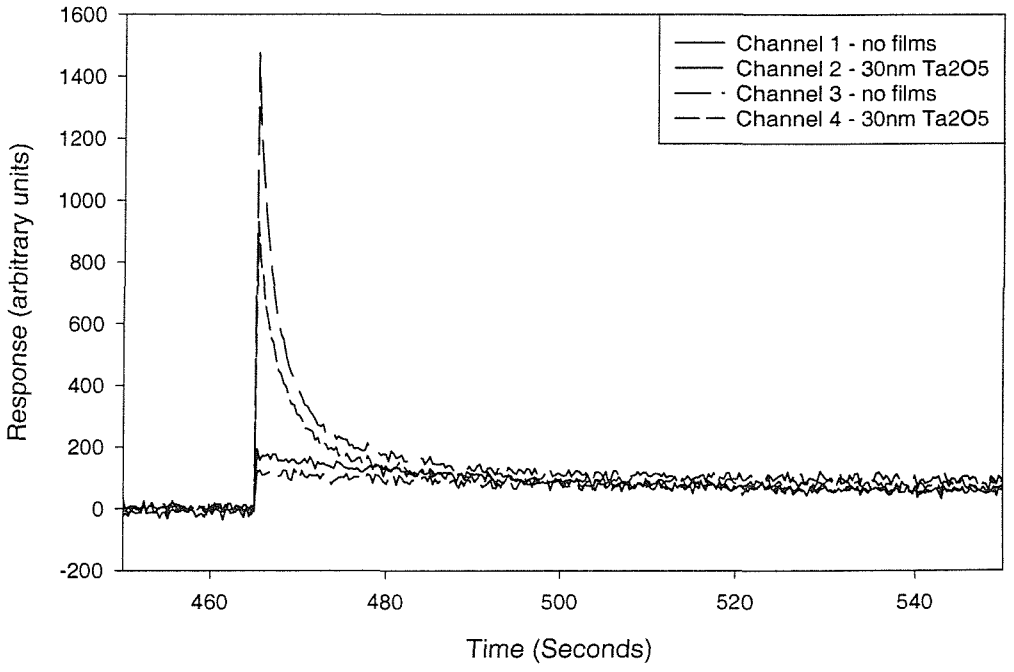

Figure 6.14: Response to antibody solution

Figure(6.16) shows the average response for channel 2 — the first Ta_2O_5 coated patch — normalized and fit with single and double exponential decay curves. This clearly shows that a double exponential gives an extremely good fit to the experi-

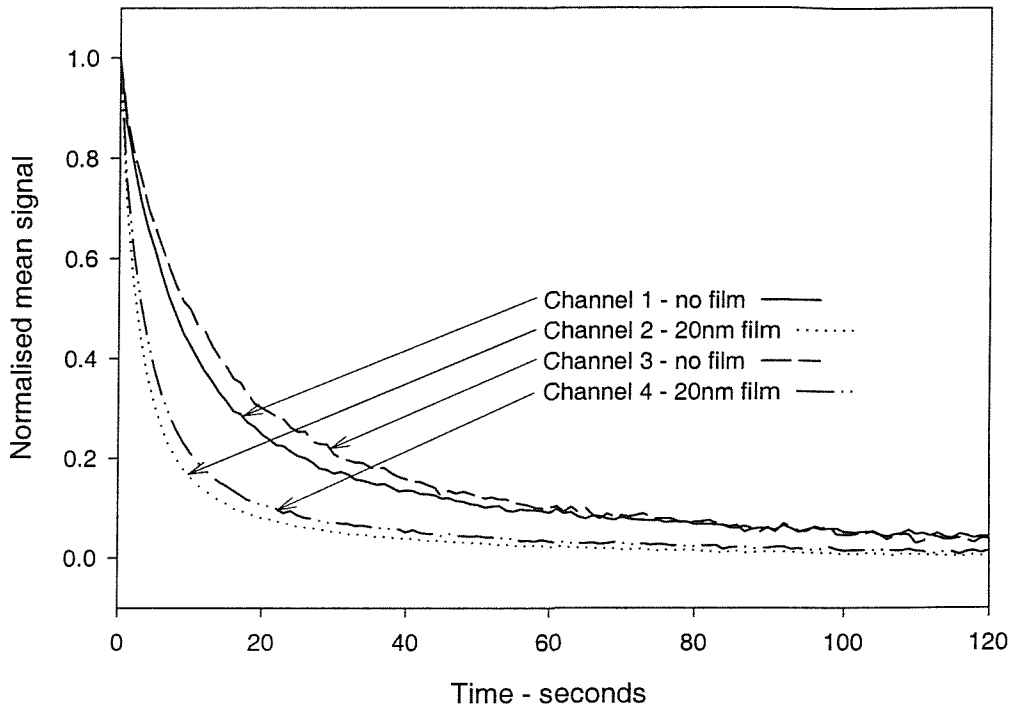

Figure 6.15: Mean response to antibody samples over 24 test cycles

mental data.

120 seconds of the signal-baseline difference was integrated for each channel and for each chip. This is enough time for the dye to bleach such that the power it emits has fallen by more than 95%. Comparing the integrals in a manner similar to that used in preparing table(6.1), table (6.2) was prepared. Here we see that the enhancement factors are far smaller in antibody experiments than in bulk dye experiments.

The reproducibility of measurements is a limiting factor for these sensors. To investigate ways of analysing the data to increase reproducibility, the data from the antibody experiments was analysed for integration times ranging between 0 and 120 seconds. This was done for each channel and for each run.

As stated at the beginning of this section, it is expected that, in the presence of photobleaching, there would be an optimum time to integrate the fluorescence signal over. If the intensity of fluorescence were constant then the optimum would

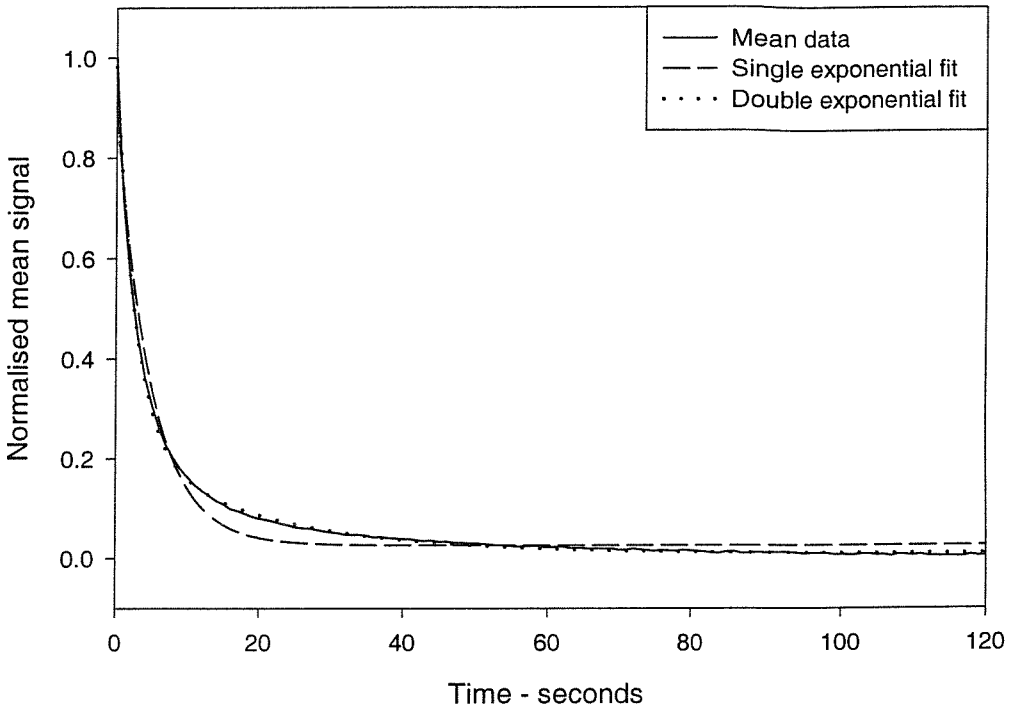

Figure 6.16: Fit to antibody response

essentially be to integrate for as long as is practical. This would allow random variations on short time-scales to effectively be averaged out. In the presence of strong photobleaching, long integration times introduce significant extra errors due to transient effects such as changing coupling between the laser and the waveguide or drifts in the intensity of the laser. There is benefit in measuring while the dye is still fluorescing, but when the fluorescence decays to a low level the difference between the signal and the baseline due to the fluorescence is lost in the random noise. Once this happens, errors are introduced due to long time-constant (compared with the measurement interval) variations, such as variations in input coupling or laser output power.

The analysis was performed as follows: from using the first data point only, up to integrating all the data up to and including 120 seconds after the shutter opened, the mean value across all the test cycles and standard error of the mean were calculated and the ratio of the standard error to the mean was calculated. The purpose of this

Thickness of overlay (nm)	Polarization	Enhancement factor	
		1st Est.	2nd Est.
20	TE	1.4	1.4
20	TM	1.3	1.3
30	TE	1.7	1.9
30	TM	1.3	1.3

Table 6.2: Enhancements calculated from responses to antibody solutions

was to give a figure for uncertainty that could be meaningfully compared across the range of data; this may be thought of as a noise to signal ratio. Clearly, the best analysis method is when the error is smallest compared to the measured value. For comparison this was done with the data referenced against the mean output power of the time the integration was performed for.

This produced a very large quantity of data, the main findings from which are presented here. Firstly, the optimum time of integration varies greatly from channel to channel and chip to chip. There does not appear to be a general rule to apply to finding this value. In some cases this value appears at a sharp minimum of a plot of standard error over mean against integration time. For others, there is an almost exponential decrease in error with time which levels off to a value of order 1%. From figure (6.17) the effect of choosing the optimum time on the data can be seen. The effect is more to level the data than to reduce scatter. Notably the integration time seems to be more important in this respect than referencing against the out-coupled power.

The reasoning for expecting an optimum integration time to exist, rather than the optimum to be integrating as long as practical, was that when the fluorescence decays to a low level, transient effects will introduce large errors. From the fact that the optimum integration times seem to vary randomly it is reasonable to surmise that these random effects are large and are not being fully compensated by the level of averaging that has been performed. The optimum integration times can therefore not, in themselves, be taken to have any great meaning. This indicates that more work may remain to be done on reducing the possible sources of large random variations in the collected fluorescence.

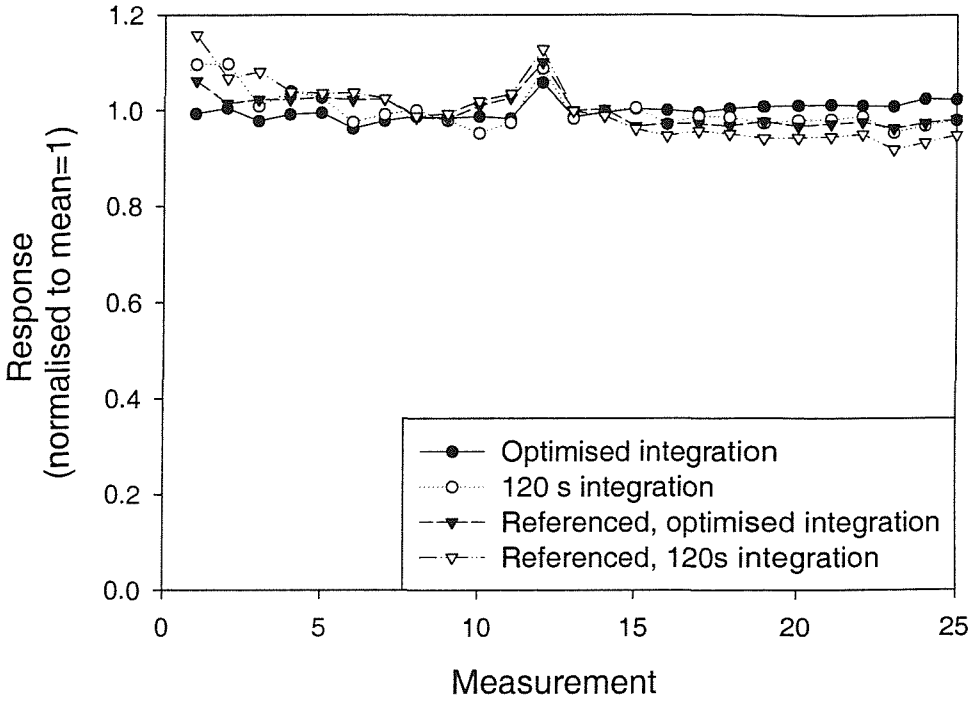

Figure 6.17: Effect of integration time and referencing on the scatter of data

The most likely sources of variation are variations in input coupling to the chip and variations in the amount of antibody bound to the surface. Variations in the input coupling can be reduced by pigtailing the chip. It was not convenient to do this for these experiments as it requires significant extra processing of the chip. This also fixes the optical axis of the fibre relative to the waveguide and means that waveguide selection cannot be changed without re-pigtailing. However, it would be useful to compare the performance of chips with the extra stability in input coupling.

Variations in the binding of antibody to the chip surface could be due to various things. If the fluidics do not reliably deliver the intended antibody concentrations to all sensing positions this would cause variations in the binding. The binding may also be effected if rinsing after regeneraton were incomplete. If the surface chemistry were somehow unreliable, or the regeneration of the surface unreliable, this would effect the amount of antibody that binds. This could be related to the fluidics or to the chemistry itself.

Experiments which discriminate between the different effects will be necessary if this is to be resolved. This means that each of these things should be investigated seperately - i.e. fibre pig-tailed chips with the same fluidics and chemistry, improved fluidics (perhaps larger volume) with the same chemistry and input coupling, etc.

However, these data reaffirm that the surface chemistry is stable (does not stop working) over a number of regenerations on the Ta_2O_5 surface. The analysis did not yield a specific integration time that produces the lowest variation of responses across the data set. The reason that the optimum integration varies so unpredictably is not at all clear. In light of these results it is therefore safest to choose an integration scheme which is applied to all the channels in a multi-channel device.

6.3.6 Calibration of sensor responses to isoproturon

Calibration of the sensors was performed using standard solutions of isoproturon for TE polarization only. Individual samples were prepared containing isoproturon concentrations from 0 to 1000 ppb. Given the previous results on the size of standard error in relation to integration time, the integration time was kept to 30s for both chips. The samples were loaded using the same automated system with the only changes being the separate individual samples and an extra step in the program to rinse the tube the samples were loaded through. The samples were loaded in random order and the results later sorted. The mean response and the standard deviation about the mean were found for each concentration where more than one sample of that concentration was injected.

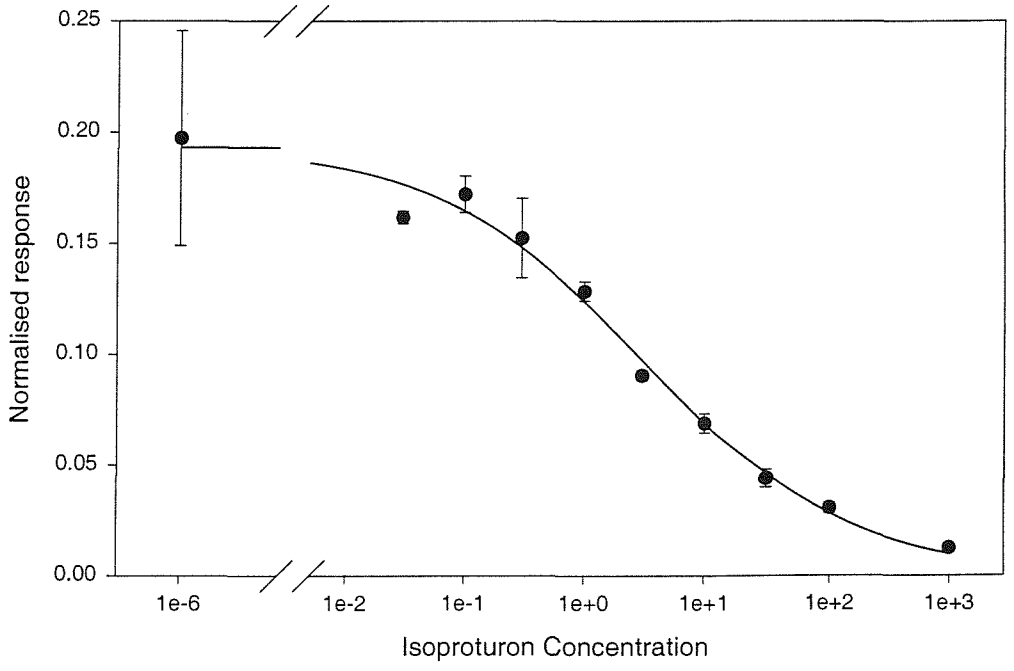

Figure 6.18: Calibration curve, chip with 20nm Ta_2O_5

An example of the results is shown in figure (6.18). From this figure a problem can be seen. The error bars correspond to the standard deviation of the data from the mean for each point. The standard deviation is unusually large for the 0ppb samples, shown as 1e-6 on the graph to allow the software to plot the logarithmic

Channel	Thickness of overlay (nm)	Detection Limit(ppb)
1	0	20
2	20	100
3	0	39
4	20	155
1	0	0.22
2	30	2.31
3	0	0.03
4	30	2.94

Table 6.3: Detection limits calculated from calibration curves

axis. This graph was chosen for the fact that this sample was the worst of the two. The detection limits, calculated as the isoproturon concentration which gives a response 3 standard deviations from the 0ppb point, are shown in table (6.3).

The results are not as would neccessarily be desired. In all cases the detection limits are higher for the channels where the high index films are present than for those without. The detection limits for the chip with the 20nm overlay are very high given that the target detection limit is 0.1ppb or lower. On the other hand, one of the bare waveguide channels on the chip with 30nm Ta_2O_5 overlay gives a calculated detection limit of 0.03ppb.

The detection limits are generally high due to large scatter of data at the 0ppb point. There are several possible reasons for this scatter. If the regeneration of the surface is not complete at the end of each test cycle then the points with less isoproturon and hence greater antibody binding will be effected most strongly. If the system does not properly rinse all the previous sample through this will also cause perturbation of the results, the lower concentration points by more again. The random order of the samples will allows both these effects to be strongly detrimental to the results.

The fact that the detection limits are lower for sensing patches further along the sensor and for patches without the high index films indicates that the intensity of light in the evanescent fields is higher than the optimum point. In this situation it is clear that the use of high index films is not appropriate, but in future work

these films could be useful where lower power light sources are to be used or where many sensors are integrated, eg. by use of concatenated y-junctions and the power is divided down.

6.3.7 Conclusions

Integrated optical multisensors have been constructed capable of sensing analytes on four channels simultaneously, to detection limits calculated to be as low as 0.03 ppb. These sensors show little variation in performance after over 100 regenerations of the sensor surface.

The addition of thin films of $Ta_2O_5$to the surface of integrated optical sensors has been shown to increase the intensity of fluorescence excited in dye molecules in the evanescent fields of guided modes. The size of the enhancements were in approximate agreement with both modelling and the previous experiments on Mach-Zehnder interferometers. Experiments with dye-labelled antibodies showed this effect, but the rate of photobleaching of the dye was increased similarly. This had the effect of causing there to be no increase in sensitivity of the sensors, a decrease was instead seen.

6.4 Summary

In these experiments the previous data on increases in evanescent power by thin high index films on the surface of waveguides has been reinforced. It has been demonstrated that the optics are suitable for multi-channel measurements at a small number of interaction zones along the length of a single waveguide and also that the materials used are compatible with the chemistry used in the RIANA application.

Due to high rates of photo-bleaching in dye molecules bound to the sensor surface, the enhancements in evanescent power have not yielded equivalent enhancements in the overall sensitivity of the devices. Whilst the high index films increases the intensity of the fluorescence by up to an order of magnitude, the detection limits of sensor patches utilising these films were in fact higher (less sensitive).

Chapter 7

Conclusions and Future Work

7.1 Conclusions

The computer modelling of [11] has been repeated, predicting that enhancements of greater than an order of magnitude in the sensitivity of evanescent wave optical sensors are possible through the use of high index overlays. The model has also been demonstrated to be capable of simulating graded index waveguide structures using the staircase approximation.

The computer model was applied to simulating various different sensing mechanisms. The enhancements in sensitivity were predicted to be similar for devices where optical properties change in the bulk superstrate or a film on the waveguide surface.

To test the theoretical predictions Mach-Zehnder interferometers were fabricated and different thickness patches of high index films were applied to the surface. By pumping sucrose solutions over the devices the sensitivity to refractive index was measured. This was performed with the excitation polarized to TE and TM separately, though it is felt that perhaps this was not done with sufficient precision.

The experiments showed not only that the enhancements predicted by modelling were attainable in practice, but that the model agreed very well with experiment on the size of enhancement as a function of film thickness for the TE polarization. It was not yet necessary to use the capability of the model to approximate diffused waveguides by the staircase approximation although this remains a useful option for the future.

The TM polarization did not yield such good results, but this may be due to a bad data set. Even though detailed analysis was not useful for these data, there was still a definite increase in the sensitivity of the devices with overlay thickness and it was definitely a much smaller increase than for the TE polarization. This is also in agreement with the computer model.

The detection limits of the devices were estimated. From this it is predicted that a sensor could be made using this process with a detection limit of 4×10^{-7}. If the design were further optimized this could be lowered further.

Fluorescence sensing experiments were performed in which it was shown that the use of high index films similarly increases the intensity of fluorescence emitted by fluorophores at the surface of the chip. Sensors were fabricated capable of measuring fluorescence at 2-4 discrete sensing positions simultaneously. These sensors were used to measure the concentrations of simazine and isoproturon in water and sensitivites as low as 0.03 ppb are reported. The highest sensitivity came from a sensing position which was not coated with the Ta_2O_5 film. The investigation of the use of high index films with fluorescence sensors has shown that the current integrated optical sensors are not limited by low intensity of illumination, but by the photodegradatation of the fluorophores in use.

7.2 Future Directions

A great emphasis in this thesis has been placed on the use of high index films on the surface of a low NA waveguide to increase the interaction of the guided mode with the superstrate medium. This technique has been shown to be highly applicable to refractometry but of reduced use in fluorescence sensing. The future will see changes in the field, such as better fluorescent dyes, which will make this technique far more useful. Other developments which one would expect to see are large arrays of sensors, in which the input power may be divided between 8, 16 or more waveguides. In this case the use of high index fields would allow low power light sources to be used without compromising sensitivity.

Another area of interest is to collect the fluorescence emitted near the waveguide surface in the waveguide and possibly to perform the filtering stage within the chip. The collection efficiency in this case is dependent on the overlap of the evanescent fields with the fluorescent medium and so the use of high index films would be a good way to incease both excitation and collection efficiency. The real benefit of this becomes clear if one recalls that, once the fluorescence is collected, it has to be separated from the excitation. By using a high index overlay, devices could be

fabricated that need an order of magnitude less excitation power and still collect an order of magnitude more fluorescence. This would close the gap between excitation and fluorescence powers by two orders of magnitude, considerably reducing the demands of filtering.

Advances in microstructuring of materials are also set to make a great impact on this field. If one were to want to perform on-chip filtering of the fluorescence then etching is still a favoured means of producing a strong grating. Of equal interest is the use of micromachining to produce flowchannels, enabling the handling of ultra-small volumes of fluids. Experiments to date have used flow-channels hundreds of times wider than the waveguides - huge advances in sensitivity and in the speed of binding are possible when the volumes are reduced. Micromachining would also be of great interest if it were combined with techniques for burying waveguides. Despite efforts to improve the quality of films used as isolation layers on the waveguide surface, these films still cause excess losses and are porous. Using techniques such as field-assisted ion-exchange it is possible to bury the waveguides below the surface of the chip, using the substrate material to isolate the waveguide. The chip could then be etched to expose the waveguide in the regions where it is to interact with a sample - indeed in the future perhaps this will be combined with the formation of micro-flowchannels such that the gaps in the isolation are the channels.

References

[1] Richard Syms and John Cozens. *Optical Guided Waves and Devices.* Mc Graw Hill, 1992.

[2] Paul V. Lambeck. Integrated opto-chemical sensors. *Sensors and Actuators B*, 8:103–116, 1992.

[3] W. Henry. Evanescent field devices: a comparison between tapered optical fibres and polished or D-fibres. *Optical and Quantum Electronics*, 26:S261–S272, 1994.

[4] A. Klotz, A. Brecht, C. Barzen, G. Gauglitz, R.D. Harris, G.R. Quigley, J.S. Wilkinson, and R.A. Abuknesha. Immunofluorescence sensor for water analysis. *Sensors and Actuators B*, 51(1-3):181–187, 1998.

[5] Ch. Stamm and W. Lukosz. Integrated optical difference interferometer as refractometer and chemical sensor. *Sensors and Actuators B*, 11:177–181, 1993.

[6] D. Freiner, R. E. Kunz, D. Citterio, U. E. Spichiger, and M. T. Gale. Integrated optical sensors based on refractometry of ion-selective membranes. *Sensors and Actuators B*, 29:277–285, 1995.

[7] R. D. Harris and J. S. Wilkinson. Waveguide surface plasmon resonance sensors. *Sensors and Actuators B*, 29(1–3):261–267, 1995.

[8] B. J. Luff, R. D. Harris, J. S. Wilkinson, R. Wilson, and D. J. Schiffrin. Integrated-optical directional coupler biosensor. *Optics Letters*, 21(8):618–620, 1996.

[9] B. J. Luff, J. S. Wilkinson, J. Piehler, U. Hollenbach, J. Ingenhoff, and N. Fabricius. Integrated optical Mach-Zehnder biosensor. *Journal of Lightwave Technology*, LT-16:583–592, 1998.

[10] G. Stewart, F. A. Muhammad, and B. Culshaw. Sensitivity improvement for evanescent-wave gas sensors. *Sensors and Actuators B*, 11:521–524, 1993.

[11] G. Stewart and B. Culshaw. Optical waveguide modelling and design for evanescent field chemical sensors. *Optical and Quantum Electronics*, 26:S249–S259, 1994.

[12] S. McCulloch, G. Stewart, R. M. Guppy, and J. O. W. Norris. Characterisation of $TiO_2 - SiO_2$ sol-gel films for optical-chemical sensor applications. *International Journal of Optoelectronics*, 9(3):235–241, 1994.

[13] F. A. Muhammad, G. Stewart, and W. Jin. Sensitivity enhancement of D-fibre methane gas sensor using high-index overlay. *IEE Proceedings-J*, 140(2):115–118, April 1993.

[14] Kiminori Itoh and Marc Madou. Optical waveguides for surface spectroscopy: $FePO_4$ thin-film/K^+-doped glass composite waveguide systems having tapered velocity couplers. *Journal of Applied Physics*, 69(11):7425–7429, June 1991.

[15] Kiminori Itoh, Xiao-Min Chen, and Masayuki Murabayashi. Ion-exchanged glass optical waveguide systems for surface spectroscopy. composite structures for realization of high sensitivity and low loss. *Chemistry Letters*, pages 1991–1994, 1993.

[16] Xiao-Min Chen, Kiminori Itoh, and Masayuki Murabayashi. Highly sensitive and low loss ion-exchanged glass optical waveguides constructed by the successive doping of K+ and Ag+ ions. *Bulletin of the Chemical Society of Japan*, 68:2823–2829, 1995.

[17] Musa Ahmad and Ramaier Narayanaswamy. Fibre optic reflectance sensor for the determination of aluminium(III) in aqeous environment. *Analytica Chimica Acta*, 291:255–260, 1994.

[18] Musa Ahmad and Ramaier Narayanaswamy. Development of an optical fibre Al(III) sensor based on immobilised chrome azurol s. *Talanta*, 42:1337–1344, 1995.

[19] A. M. Ervin, K. J. Ewing, R. A. Lamontagne, I. D. Aggarwal, and D. A. Rowley. Development of a fiber-optic sensor for trace metal detection in aqeous environments. *Applied Optics*, 32(22):4287–4289, August 1993.

[20] Zhihao Lin and Lloyd W. Burgess. Chemically facilitated donnan dialysis and its application in a fiber optic heavy metal sensor. *Analytical Chemistry*, 66(15):2544–2551, August 1994.

[21] Zhihao Lin, Karl S. Booksh, Lloyd W. Burgess, and Bruce R. Kowalski. Second-order fiber optic heavy metal sensor employing second-order tensorial calibration. *Analytical Chemistry*, 66(15):2552–2560, August 1994.

[22] Faris A. Muhammad and George Stewart. Polarised finite-difference analysis of D-fibre and application for chemical sensing. *International Journal of Optoelectronics*, 7(6):705–721, 1992.

[23] B. D. MacCraith, C. M. McDonagh, G. O'Keeffe, A. K. McEvoy, T. Butler, and F. R. Sheridan. Sol-gel coatings for optical chemical sensors and biosensors. *Sensors and Actuators B*, 29:51–57, 1995.

[24] Lin Yang, S. Scott Saavedra, and Neal R. Armstrong. Sol-gel-based, planar waveguide sensor for gaseous iodine. *Analytical Chemistry*, 68(11):1834–1841, June 1996.

[25] Christophe Piraud, Eustace K. Mwarania, J. Yao, K. O'Dwyer, D. J. Schiffrin, and James S. Wilkinson. Optoelectrochemical transduction on planar optical waveguides. *Journal of Lightwave Technology*, 10(5):693–699, May 1992.

[26] Darren R. Dunphy, Sergio B. Mendes, S. Scott Saavedra, and Neal R. Armstrong. The electroactive integrated optical waveguide: Ultrasensitive spectroelectrochemistry of submonolayer adsorbates. *Analytical Chemistry*, 69(15):3086–3094, August 1997.

[27] J. Bürck, B. Zimmerman, J. Mayer, and H. J. Ache. Integrated optical NIR-evanescent wave absorbance sensor for chemical analysis. *Fresenius Journal of Analytical Chemistry*, 354:284–290, 1996.

[28] Sergio B. Mendes and S. Scott Saavedra. On probing molecular monolayers: a spectroscopic optical waveguide approach of ultra-sensitivity. *Optics Express*, 4(11), May 1999.

[29] R. G. Heideman, R. P. H. Kooyman, and J. Greve. Performance of a highly sensitive optical waveguide Mach-Zehnder interferometer immunosensor. *Sensors and Actuators B*, 10:209–217, 1993.

[30] B. J. Luff, R. D. Harris, and J. S. Wilkinson. Directional coupler sensor using a low-index fluoropolymer isolation layer. In *Proceedings 7th European Conference on Integrated optics*, pages 169–172, Delft, The Netherlands, April 1995.

[31] E. F. Schipper, R. P. H. Kooyman, R. G. Heideman, and J. Greve. Feasibility of optical waveguide immunosensors for pesticide detection: physical aspects. *Sensors and Actuators B*, 24–25:90–93, 1995.

[32] L. M. Lechuga, A. T. M. Lenferink, R. P. H. Kooyman, and J. Greve. Feasibilty of evanescent wave interferometer immunosensors for pesticide detection: chemical aspects. *Sensors and Actuators B*, 24–25:762–765, 1995.

[33] R. Kherrat, N. Jaffrezic-Renault, P. Greco, H. Helmers, P. Benech, and R. Rimet. Integrated optical enlarged-field interferometer used as a chemical sensor. *Sensors and Actuators B*, 37:7–11, 1996.

[34] Th. Schubert, N. Haase, H. Kück, and R. Gottfried-Gottfried. Refractive-index measurements using an integrated Mach-Zehnder interferometer. *Sensors and Actuators A*, 60:108–112, 1997.

[35] Ch. Fattinger, H. Koller, D. Schlatter, and P. Wehrli. The difference interferometer: a highly sensitive optical probe for quantification of molecular surface concentration. *Biosensors and Bioelectronics*, 8:99–107, 1993.

[36] D. Schlatter, R. Barner, Ch. Fattinger, W. Huber, J. Hübscher, J. Hurst, H. Koller, C. Mangold, and F. Müller. The difference interferometer: application as a direct affinity sensor. *Biosensors and Bioelectronics*, 8:109–116, 1993.

[37] W. Lukosz. Integrated optical chemical and direct biochemical sensors. *Sensors and Actuators B*, 29:37–50, 1995.

[38] D. Clerc and W. Lukosz. Real-time analysis of avidin adsorption with an integrated-optical output gratin coupler: adsorption kinetics and optical

anisotropy of adsorbed monomolecular layers. *Biosensors and Bioelectronics*, 12(3):185–194, 1997.

[39] Rino E. Kunz. Integrated optical sensors based on hard dielectric films on replicated plastic substrates. In *Proceedings 8th European Conference on Integrated Optics*, pages 86–93, Stockholm, Sweden, April 1997. Paper EWD1.

[40] J. Dübendorfer and R. E. Kunz. Compact integrated optical immunosensor using replicated chirped grating coupler sensor chips. *Applied Optics*, 37(10):1890–1894, April 1998.

[41] M. Wiki, R. E. Kunz, G. Voirin, K. Tiefenthaler, and A. Bernard. Novel integrated optical sensor based on a grating coupler triplet. *Biosensors and Bioelectronics*, 13:1181–1185, 1998.

[42] Steven A. Soper, Linda B. McGown, and Isiah M. Warner. Molecular fluorescence, phosphorescence and chemiluminescence spectrometry. *Analytical Chemistry*, 66(12):428R–444R, June 1994.

[43] Huarui He, Hong Li, Gerhard Mohr, Barna Kovács, Tobias Werner, and Otto S. Wolfbeis. Novel type of ion-selective fluorosensor based on the inner filter effect: An optrode for potassium. *Analytical Chemistry*, 65(2):123–127, 1993.

[44] Z. M. Hale and F. P. Payne. Fluorescent sensors based on tapered single-mode fibres. *Sensors and Actuators B*, 17:233–240, 1994.

[45] D. Marcuse. Launching light into fiber cores from sources located in the cladding. *Journal of Lightwave Technology*, 6(8):1273–1279, August 1988.

[46] G. L. Duveneck, M. Pawlak, D. Neuschäfter, E. Bär, W. Budach, U. Pieles, and M. Ehrat. Novel bioaffinity sensors for trace analysis based on luminescence excitation by planar waveguides. *Sensors and Actuators B*, 38–39:88–95, 1997.

[47] Steven J. Choquette, Laurie Locascio-Brown, and Richard A. Durst. Planar waveguide immunosensor with fluorescent liposome amplification. *Analytical Chemistry*, 64(1):55–60, January 1992.

[48] Y. Zhou, J. V. Magill, R. M. De La Rue, P. J. R. Laybourn, and W. Cushley. Evanescent fluorescent immunoassays performed with a disposable ion-exchanged patterned waveguide. *Sensors and Actuators B*, 11:245–250, 1993.

[49] Jens Kremeskötter, Robert Wilson, David J. Schiffrin, B. Jonathan Luff, and James S. Wilkinson. Detection of glucose via electrochemiluminescence in a thin-layer cell with a planar optical waveguide. *Measurement Science and Technology*, 6:1325–1328, 1995.

[50] T. E. Plowman, W. M. Reichert, C. R. Peters, H. K. Wang, D. A. Christensen, and J. N. Herron. Femtomolar sensitivity using a channel-etched thin film waveguide fluoroimmunosensor. *Biosensors and Bioelectronics*, 12(1/2):149–160, 1996.

[51] L. Mosiello, L. Nencini, L. Segre, and M. Spanò. A fibre-optic immunosensor for 2,4-dichlorophenoxyacetic acid detection. *Sensors and Actuators B*, 38–39:353–359, 1997.

[52] Richard B. Thompson and Eric R. Jones. Enzyme-based fiber optic zinc biosensor. *Analytical Chemistry*, 65(6):730–734, 1993.

[53] D. J. S. Birch, A. S. Holmes, and M. Darbyshire. Intelligent sensor for metal ions based on fluorescence resonance energy transfer. *Measurement Science and Technology*, 6:243–247, 1995.

[54] Max E. Lippitsch, Sonja Draxler, and Dietmar Kieslinger. Luminescence lifetime-based sensing: new materials, new devices. *Sensors and Actuators B*, 38–39:96–102, 1997.

[55] Leah Tolosa, Henryk Malak, Govind Raob, and Joseph R. Lakowicz. Optical assay for glucose based on the luminescence decay time of the long wavelength dye cy5. *Sensors and Actuators B*, 45:93–99, 1997.

[56] Leah Tolosa, Henryk Szmacinski, Govind Rao, and Joseph R. Lakowicz. Lifetime-based sensing of glucose using energy transfer with a long lifetime donor. *Analytical Biochemistry*, 250:102–108, 1997.

[57] Hai-Jui Lin, Henryk Szmacinski, and Joseph R. Lacowicz. Lifetime-based pH sensors: Indicators for acidic environments. *Analytical Biochemistry*, 269:162–167, 1999.

[58] Olaf J. Rolinski and David J. S. Birch. A fluorescence lifetime sensor for cu(i) ions. *Measurement Science and Technology*, 10:127–136, 1999.

[59] River analyser final presentation, June 1999.

[60] Pochi Yeh. *Optical Waves in Layered Media.* John Wiley and Sons, 1988.

[61] Dietrich Marcuse. *Theory of Dielectric Optical Waveguides.* Academic Press, second edition, 1991.

[62] Amnon Yariv. *Optical Electronics in Modern Communications.* Oxford University Press, fifth edition, 1997.

[63] Ajoy K. Ghatak, K. Thyagarajan, and M. R. Shenoy. Numerical analysis of planar optical waveguides using matrix approach. *Journal of Lightwave Technology*, LT-5(5):660–667, May 1987.

[64] M. R. Ramadas, E. Garmire, A. K. Ghatak, K. Thyagarajan, and M. R. Shenoy. Analysis of absorbing and leaky planar waveguides: a novel method. *Optics Letters*, 14(7):376–378, April 1989.

[65] E. K. Sharma, M. P. Singh, and P. C. Kendall. Exact multilayer waveguide design including absorbing or metal layers. *Electronics Letters*, 27(5):408–410, February 1991.

[66] John Chilwell and Ian Hodgkinson. Thin-films field-transfer matrix theory of planar multilayer waveguides and reflection from prism-loaded waveguides. *Journal of the Optical Society of America A*, 1(7):742–753, July 1984.

[67] S. D. Conte and C. de Boor. *Elementary Numerical Analysis: an algorithmic approach.* McGraw-Hill, second edition, 1972.

[68] Pascal Mauron. Internal communications. Computer modelling performed as part of a final year undergraduate project whilst visiting the University of Southampton from the Swiss Federal Institute of Technology.

[69] Emmanuel Anemogiannis and Elias N. Glytsis. Multilayer waveguides: Efficient numerical analysis of general structures. *Journal of Lightwave Technology*, 10(10):1344–1351, October 1992.

[70] A. Gedeon. Comparison between rigorous theory and wkb-analysis of modes in graded-index waveguides. *Optics Communications*, 12(3):329–332, November 1974.

[71] G. Hass. Preparation, properties and optical applications of thin films of titanium dioxide. *Vacuum*, 11(4):330–345, October 1952.

[72] Pascal Mauron. Collection of the fluorescent light emitted by dye molecules adsorbed to the surface of a dielectric slab waveguide: A modal approach. Final practical work submitted for diploma of engineer in micro-engineering, Department of Micro-Engineering, Swiss Federal Institute of Technology and Optoelectronics Research Centre, University of Southampton, 1995.

[73] R. D. Harris. *Waveguide Surface Plasmon Resonance Biosensor*. Thesis submitted for the degree of doctor of philosophy, University of Southampton, February 1996.

Appendix A

Publications List

[1] A.Klotz, C.Barzen, A.Brecht, R.D.Harris, G.R.Quigley, J.S.Wilkinson, G.Gauglitz Sensitivity enhancement of transducers for total internal reflection fluorescence *SPIE Int Symposium on Integrated Optoelectronic Devices San Jose*, 23-29 January 1999, 3620-53

[2] G.R.Quigley, R.D.Harris, J.S.Wilkinson Sensitivity enhancement of integrated optical sensors by use of thin high-index films *Applied Optics 1999*, Vol.38(28) pp.6036-9

[3] A.Brecht, C.Barzen, A.Klotz, G.Gauglitz, R.D.Harris, G.Quigley, J.S.Wilkinson, S.Fraval, P.Sztajnbok, D.Barcelo, J.Gascon, M.Steinwand, R.Abuknesha River Analyser - multiresidue immunoanalytical monitoring tools *Biosensors for Environmental Diagnostics* 1998, Teubner, Stuttgart, Germany pp.147-160

[4] R.D.Harris, G.R.Quigley, J.S.Wilkinson, A.Klotz, C.Barzen, A.Brecht, G.Gauglitz, R.A.Abuknesha Waveguide immunofluorescence sensor for water pollution analysis *SPIE Int Symposium on Industrial & Environmental Monitors & Biosensors*, Boston, 1-6 November 1998 Vol.3539 pp.27-35

[5] A.Klotz, A.Brecht, C.Barzen, G.Gauglitz, R.D.Harris, G.R.Quigley, J.S.Wilkinson, R.A.Abuknesha Immunofluorescence sensor for water analysis *Sensors & Actuators B* 1998, Vol.51, No.1-3, pp.181-187

[6] R.D.Harris, G.R.Quigley, J.S.Wilkinson, A.Klotz, C.Barzen, A.Brecht, G.Gauglitz, R.A.Abuknesha Integrated optical immunofluorescence sensor for environmental monitoring *Biosensors '98*, Berlin, Germany, 3-5 June 1998,Proc. pp.72

[7] A.Brecht, A.Klotz, C.Barzen, G.Gauglitz, R.D.Harris, G.R.Quigley, J.S.Wilkinson, P.Sztajnbok, R.Abuknesha, J.Gascon, A.Oubinam D.Barcelo Optical immunoprobe development for multiresidue monitoring in water *Analytica Chimica Acta*, 1998, Vol.362 pp.69-79

[8] A.Klotz, A.Brecht, C.Barzen, G.Gauglitz, R.D.Harris, G.R.Quigley, J.S.Wilkinson, R.A.Abuknesha Immunofluorescence sensor for water analysis *Europt(r)ode IV* Muenster, Germany, 29 March-1 April 1998

[9] L.M.B.Hickey, G.R.Quigley, J.S.Wilkinson, E.G.Moya, F.Moya, C.Grattepain Ti-diffusion in sapphire for active and passive waveguide devices *CLEO/Europe '98* Glasgow, Scotland 13-18 Sept 1998, CThF3

[10] G.R.Quigley, R.D.Harris and J.S.Wilkinson Sensitivity enhancement of integrated optics sensors by thin high index films *European Conference on Integrated Optics '97* 2-4 Apr 1997 Proc Eth-H8, 326-9